3-2-2021

# Machining of Inconel 718 nickel-based superalloy using nano-lubricants and liquid nitrogen

Behzad Eskandari
*University of Windsor*

# MACHINING OF INCONEL 718 NICKEL-BASED SUPERALLOY USING NANO-LUBRICANTS AND LIQUID NITROGEN

By

Behzad Eskandari

A Thesis

Submitted to the Faculty of Graduate Studies

through the Department of Mechanical, Automotive and Materials Engineering

in Partial Fulfillment of the Requirements for

the Degree of Master of Applied Science

at the University of Windsor

Windsor, Ontario, Canada

2020

# MACHINING OF INCONEL 718 NICKEL-BASED SUPERALLOY USING NANO-LUBRICANTS AND LIQUID NITROGEN

By

Behzad Eskandari

APPROVED BY:

W. Abdul-Kader
Department of Mechanical, Automotive and Materials Engineering

---

Wm. Altenhof
Department of Mechanical, Automotive and Materials Engineering

---

A. T. Alpas, Advisor
Department of Mechanical, Automotive and Materials Engineering

December 21, 2020

# DECLARATION OF CO-AUTHORSHIP / PREVIOUS PUBLICATION

I. Co-Authorship

I hereby declare that this thesis incorporates material that is result of joint research, as follows:

Chapter 3 and 4 of this thesis was co-authored with Dr. Sukanta Bhowmick under the supervision of Professor Ahmet T. Alpas. In all cases, the key ideas, primary contributions, experimental designs, data analysis, interpretation, and writing were performed by the author, and the contribution of Dr. Bhowmick was primarily through discussions on tribological analyses and consultation on tribology test results. Professor Alpas provided the initial outline of the projects according to the research programs of NSERC Strategic Consortium CANRIMT feedback on refinement of the ideas and editing of the manuscripts.

I am aware of the University of Windsor Senate Policy on Authorship and I certify that I have properly acknowledged the contribution of other researchers to my thesis, and have obtained written permission from each of the co-author(s) to include the above material(s) in my thesis. I certify that, with the above qualification, this thesis, and the research to which it refers, is the product of my own work.

II. Previous Publication

This thesis includes two original papers that have been previously published/submitted for publication in peer reviewed journals, as follows:

| Thesis chapter | Publication title/full citation | Publication status |
|---|---|---|
| Chapter 3 | Eskandari, Behzad, Sukanta Bhowmick, and Ahmet T. Alpas. "Flooded drilling of Inconel 718 using graphene incorporating cutting fluid." *The International Journal of Advanced Manufacturing Technology* (2020): 1-14. https://doi.org/10.1007/s00170-020-06195-9 | Published |
| Chapter 4 | Eskandari, Behzad, Sukanta Bhowmick, and Ahmet T. Alpas. "Turning of Inconel 718 Using Liquid Nitrogen: RSM Multi-Response Optimization of Cutting Parameters. " *Journal of Manufacturing Processes* (2020) | Submitted |

I certify that I have obtained a written permission from the copyright owner(s) to include the above published material(s) in my thesis. I certify that the above material describes work completed during my registration as a graduate student at the University of Windsor.

III. General

I declare that, to the best of my knowledge, my thesis does not infringe upon anyone's copyright nor violate any proprietary rights and that any ideas, techniques, quotations, or any other material from the work of other people included in my thesis, published or otherwise, are fully acknowledged in accordance with the standard referencing practices. Furthermore, to the extent that I have included copyrighted material that surpasses the bounds of fair dealing within the meaning of the Canada Copyright Act, I certify that I have obtained a written permission from the copyright owner(s) to include such material(s) in my thesis.

I declare that this is a true copy of my thesis, including any final revisions, as approved by my thesis committee and the Graduate Studies office, and that this thesis has not been submitted for a higher degree to any other University or Institution.

# ABSTRACT

Utilization of cutting fluid incorporating graphene nanoplatelets (GNP) as well as application of liquid nitrogen ($LN_2$) to the cutting area were investigated in drilling and turning of Inconel 718 iron-nickel-based superalloy in order to improve their machinability and reduce the use of mineral-based cutting fluids. The methodology was developed to establish correlations between the tribological properties of the surfaces and the role of interfacial friction on machining properties and understanding the improvements in machining from a microstructural point of view. In addition, response surface methodology (RSM) was employed to systematically optimized the cutting parameters. The results are presented in two parts: In Chapter 3, a cutting fluid (CF) consisting of 70% water and 30% vegetable oil blended with GNPs was used in order to improve drilling performance of Inconel 718 alloy. The results showed that sliding of Inconel 718 workpiece using WC-Co drills with CF containing $54\times10^{-5}$ wt.% graphene (GCF) reduced the coefficient of friction (COF) between the tool and workpiece surfaces from 0.16 to 0.08 as a result of formation of tribolayers on the sliding surfaces. A Similar tribolayer was observed when drilling under GCF condition which resulted in lower cutting torque and temperature, leading to lower surface roughness and subsurface microstructural deformation compared to conventional flooded and dry conditions. In Chapter 4, turning experiments were conducted on the Inconel 718 using a stream of liquid nitrogen, and the effects of different cutting speed, feed rate and depth of cut values on the response factors, namely flank wear, cutting force and $R_a$ surface roughness were investigated. Cryogenic cutting reduced flank wear compared to dry cutting, to values comparable to wear during flooded cutting. The results revealed that there could be an optimum set of values in which cryogenic cutting can provide a performance equivalent to the flooded cutting. Thus, experiments were designed according to RSM under cryogenic condition. Statistical analyses showed that cutting speed was the most influential parameter on flank wear and cutting force during cryogenic turning and a cutting speed of 81 m/min, a feed rate of 0.06 mm/rev and a depth of cut of 0.63 mm constituted the optimum set of cutting parameters considered in this investigation. Higher cutting speed and feed rate values can be used during the machining process by using a GNP-blended vegetable-based oil to shorten the cutting time, and thus, reduce the usage of cutting fluid for production of each part. Moreover, it was shown that complete omission of cutting fluid during the machining process would be feasible by employing cryogenic cutting. Liquid nitrogen evaporates after contacting the tool and workpiece surfaces leaving no contamination which eliminates the cleaning, recycling, and deposal costs after the machining process.

*To my mother and father*

# ACKNOWLEDGEMENTS

I would like to express my deep and sincere gratitude to my research supervisor, Professor A.T. Alpas for giving me the opportunity to do this research and for his constant support and invaluable guidance throughout my graduate studies. It was a great privilege and honor to work and study under his guidance. Also, special thanks to Dr. S. Bhowmick for his constant encouragement, support and friendship.

I would also like to thank my committee members, Dr. W. Altenhof and Dr. W. Abdul-Kader, for their invaluable discussions, suggestions and time.

I extend my thanks to the financial support provided by Natural Sciences and Engineering Research Council of Canada (NSERC) through a Strategic Network for Research and Innovation in Machining Technology (CANRIMT) Grant NETGP 479639-15.

Also, I would like to express my appreciation to manager of the Technical Support, Mr. A. Jenner, for all his supports throughout the experimental tests. Also, I would like to thank Mr. T. Bolger and Mr. D. Tremblay from Technical Support Centre for providing assistance with the cryogenic machining experiments. Sincere thanks to Mr. R. Barakat for invaluable help with the preparation of the force measurement system.

Finally, I wish to thank my mother and father for their love and sacrifices and my sister, brother, sister in law and brother in law for their support and prayers.

# TABLE OF CONTENT

# LIST OF ABBREVIATIONS/SYMBOLS

| | |
|---|---|
| CF | Cutting fluid |
| COF | Coefficient of friction |
| f | Feed rate |
| $F_C$ | Force along the tool face |
| $F_P$ | Force in horizontal direction |
| $F_Q$ | Force in vertical direction |
| $F_S$ | Force along the shear plane |
| GCF | Graphene blended cutting fluid |
| GNP | Graphene nanoplatelet |
| i | Inclination angle of the cutting tool |
| $KV_{max}$ | Rake wear |
| $LN_2$ | Liquid nitrogen |
| $N_C$ | Force perpendicular to the tool face |
| $N_S$ | Force perpendicular to the shear plane |
| r | Tool nose radius |
| $R_a$ | Arithmetic average roughness |
| $R_t$ | Maximum peak to valley height |
| $R_z$ | Average peak to valley height |
| V | Cutting speed |
| $VB_{max}$ | Flank wear |
| $V_C$ | Chip speed |
| $V_S$ | Shearing speed |
| $t_c$ | Chip thickness |
| $\phi$ | Shear plane angle |
| $\mu$ | Coefficient of friction |
| $\beta$ | Friction angle |
| $\alpha_c$ | Chip flow angle |
| $\alpha_t$ | Normal rake angle |
| $\sigma_c$ | Compressive stress |

# LIST OF FIGURES

# LIST OF TABLES

# CHAPTER 1

# INTRODUCTION

Superalloys are used in demanding industrial applications ranging from aircraft components such as jet engine and chemical and petrochemical equipment to medical, and nuclear parts [1]. It is their special combination of mechanical properties, such as high strength at elevated temperatures, high corrosion resistance, excellent thermal fatigue properties and thermal stability [2] that have made these alloys favorable for such a wide range of modern engineering applications.

However, superalloys are considered as difficult-to-cut materials. The fact that superalloys retain their strength at elevated temperatures, which normally softens steel, results in high cutting force. Given that almost all the cutting energy converts to heat in machining as a result of friction at the tool-chip interface, high cutting temperature generates during cutting of these alloys and low thermal conductivity of superalloys entraps the generated heat in the cutting area. Consequently, high cutting force and temperature result in high adhesion and dissolution wear on the cutting tool [2, 3] and reduce the machined surface quality [4-6] in terms of

increasing surface roughness. Presence of abrasive carbides in superalloys, on the other hand, promotes abrasive wear of the cutting flank and rake faces of the cutting tools.

Generally, it has been shown that application of cutting fluid during the cutting process improves machinability of alloys by increasing tool life [7] and decreasing cutting temperature [8] and adhesion of workpiece material to the cutting tool [9]. There are various types of cutting fluids utilized in machining processes [10]:

1. Straight oils, including mineral and vegetable oils typically used for low temperature cutting processes conducted at low speeds.
2. Soluble oils, a mixture of oil and water and additives which are generally used when higher speeds are used.
3. Semisynthetic fluids, made of chemical emulsions mixed with mineral oil and diluted in water.
4. Synthetic fluids, chemicals with additives, diluted in water, and containing no oil.

Almost 80% of the cutting fluid consumption worldwide is mineral-based cutting fluid [11]. This is because of its high lubrication efficiency resulting in high quality machined part, making it favorable for the production managers and machinists. However, there are some concerns over use of mineral-based cutting fluids during the cutting process. It has been reported that 80% of all occupational infections of the operators were due to skin contact with the cutting fluids [12]. The International Agency for Research on Cancer (IARC) has reported that heterocyclic and polyaromatic rings existing in petroleum-based cutting fluids are carcinogenic [13]. For this reason, the Environmental Protection Agency (EPA) has special requirements regarding storage and disposal of mineral-based cutting fluids.

Consequently, the current trend in metal cutting process is towards using ‘green machining’ in which either the mineral-based cutting fluids are being replaced with eco-friendly cutting fluids or dry cutting approaches are implemented [14]. Vegetable-based cutting fluids are introduced as an alternative to mineral-base oils. However, the efficiency of these kinds of cutting fluids need to be improved. Addition of nanoparticles to the vegetable-based fluids are used to improve their lubrication effects so that friction in the tool-chip interface decreases. Cryogenic cutting which cools down the primary and secondary cutting areas, on the other hand, could be used as a clean cutting method in which no cutting fluid is used, while achieving the results comparable to those of conventional flooded cutting.

## 1.1. RESEARCH OUTLINE

In Chapter 2, superalloys history and metallurgical properties are presented in Section 2.1. Also, metal cutting principles, namely orthogonal and oblique cutting models, chip types and formation mechanism and cutting force and temperature as well as turning process principles are given in Section 2.2. Then, the problems in machining of superalloys are discussed and previous studies on the methods for addressing these problems, namely addition of nanoparticles in the cutting fluid as well as use of liquid nitrogen in cutting of superalloys are summarized in Section 2.3.

Chapter 3 investigates the tribological behaviour of Inconel 718 against WC-Co using different concentrations of graphene in cutting fluid. The relationships between tribological behaviour of surfaces and the drilling parameters were studied. For this purpose, drilling tests were carried out on Inconel 718 to evaluate the effect of graphene nanoplatelets (GNP)-blended cutting fluid on the machining performance of Inconel 718. The main objective of pin on disk and drilling

tests in this chapter was to examine whether the formation of tribolayers could play a role in reducing the cutting torques, tool wear and surface roughness of the drilled holes through tribological and material characterization approaches. In addition, this chapter attempts to make a connection between improvement of the machining performance of Inconel 718 by formation of tribolayer on the tool surface and the workpiece subsurface microstructural deformation during the drilling process.

Chapter 4 summarizes the results of cryogenic cutting of Inconel 718 during a turning process. This chapter is presented in two parts i.e. comparison of effect of cryogenic cutting with flooded and dry conditions, aiming to determine whether any improvements in machinability of Inconel 718 would achieve by application of liquid nitrogen ($LN_2$) to the cutting area. For this purpose, the turning tests were done at different cutting parameters (cutting speed, feed rate and depth of cut) and the resulting flank wear, cutting force and $R_a$ surface roughness were compared with the observations from flooded and dry cutting. The main objective of this part was to evaluate the effectiveness of application of $LN_2$ to the cutting area in increasing the machinability of Inconel 718 so that it will be comparable to conventional flooded cutting. In the second part, statistical analysis and multi-response optimization using desirability function of RSM were employed in order to investigate the effect of cutting parameters on the response factors, namely flank wear, cutting force, $R_a$ surface roughness and material removal rate (MRR) and determine the optimum cutting parameters in cutting under cryogenic condition. Thus, cutting speed, feed rate and depth of cut were selected as cutting parameters each in five levels.

The practical objective of this research was to evaluate and improve implementation of alternatives to mineral-based cutting fluids, namely addition of GNP to a vegetable-based

cutting fluid as well as application of $LN_2$ to the cutting area. The scientific objectives included development of a methodology whereby the relationships between the surface and subsurface properties of the materials and their machining performance could be correlated. This constitutes a relatively new approach of conducting sliding tests and using its results in determining the underlying reason of improvement of machinability of Inconel 718 using GNP-incorporated cutting fluid.

## REFERENCES

[1] M.J. Donachie, S.J. Donachie, Superalloys: a technical guide, ASM international, OH, USA, 2002.

[2] D. Zhu, X. Zhang, H. Ding, Tool wear characteristics in machining of nickel-based superalloys, International Journal of Machine Tools and Manufacture, 64 (2013) 60-77.

[3] B. Eskandari, B. Davoodi, H. Ghorbani, Multi-objective optimization of parameters in turning of N-155 iron-nickel-base superalloy using gray relational analysis, Journal of the Brazilian Society of Mechanical Sciences and Engineering, 40 (2018) 233.

[4] B. Davoodi, B. Eskandari, Evaluation of surface damage mechanisms and optimisation of cutting parameters in turning of N-155 iron-nickel-base superalloy, International Journal of Machining and Machinability of Materials, 21 (2019) 100-114.

[5] A. Thakur, S. Gangopadhyay, State-of-the-art in surface integrity in machining of nickel-based super alloys, International Journal of Machine Tools and Manufacture, 100 (2016) 25-54.

[6] S. Bhowmick, B. Eskandari, M.Z.U. Khan, A.T. Alpas, Investigation of the role of tribolayer formation in improving drilling performance of Ti-6Al-4V using minimum quantity of lubrication, Proceedings of the Institution of Mechanical Engineers, Part J: Journal of Engineering Tribology, (2020) 1-14.

[7] S.A. Lawal, I.A. Choudhury, Y. Nukman, Application of vegetable oil-based metalworking fluids in machining ferrous metals—A review, International Journal of Machine Tools and Manufacture, 52 (2012) 1-12.

[8] M.M.A. Khan, M.A.H. Mithu, N.R. Dhar, Effects of minimum quantity lubrication on turning AISI 9310 alloy steel using vegetable oil-based cutting fluid, Journal of Materials Processing Technology, 209 (2009) 5573-5583.

[9] M. Soković, K. Mijanović, Ecological aspects of the cutting fluids and its influence on quantifiable parameters of the cutting processes, Journal of Materials Processing Technology, 109 (2001) 181-189.

[10] S. Kalpakjian, S. Schmid, Manufacturing Engineering and Technology, SI Edition, Singapore: Pearson Publications, 2013.

[11] S. Debnath, M.M. Reddy, Q.S. Yi, Environmental friendly cutting fluids and cooling techniques in machining: a review, Journal of Cleaner Production, 83 (2014) 33-47.

[12] Y.M. Shashidhara, S.R. Jayaram, Vegetable oils as a potential cutting fluid—An evolution, Tribology International, 43 (2010) 1073-1081.

[13] H.S. Abdalla, W. Baines, G. McIntyre, C. Slade, Development of novel sustainable neat-oil metal working fluids for stainless steel and titanium alloy machining. Part 1. Formulation development, The International Journal of Advanced Manufacturing Technology, 34 (2007) 21-33.

[14] S. Zahoor, F. Ameen, W. Abdul-Kader, J. Stagner, Environmentally conscious machining of Inconel 718: surface roughness, tool wear, and material removal rate assessment, The International Journal of Advanced Manufacturing Technology, 106 (2020) 303-313.

# CHAPTER 2

# LITERATURE SURVEY

## 2.1. AN OVERVIEW OF SUPERALLOYS

Superalloys were developed in early 20th century in response to the need for a stronger and more corrosion resistant materials capable of withstanding creep and impact loads at the high temperatures of hot section of gas turbines [1]. Iron-nickel based superalloys were derived from stainless steels which were used extensively before introduction of superalloys. Other types of superalloys were then developed by addition of nickel and cobalt [2]. Today, superalloys are divided into main three groups: iron-nickel-, nickel-, and cobalt-based alloys. Table 1 presents typical composition of each type of superalloy. Figure 1 shows an overview of the improvement of creep service life of Ni-based superalloys in terms of the amount of temperature for 100 h creep life at 137 MPa load in the form of wrought, conventionally cast, directionally solidified and single crystal structure.

Table 1 Typical composition of iron-nicke-, nickel- and cobalt-base superalloys [1].

| Alloy | Composition, % | | | | | | | | | | |
|---|---|---|---|---|---|---|---|---|---|---|---|
| | Cr | Ni | Co | Mo | W | Nb | Ti | Al | Fe | C | Other |
| Iron-nickel-base | | | | | | | | | | | |
| Incoloy 800 | 21.0 | 32.5 | - | - | - | - | 0.38 | 0.38 | 45.7 | 0.05 | - |
| Nickel-base | | | | | | | | | | | |
| Haynes 214 | 16.0 | 76.5 | - | - | - | - | - | 4.5 | 3.0 | 0.03 | - |
| Cobalt-base | | | | | | | | | | | |
| UMCo-50 | 28.0 | - | 49.0 | - | - | - | - | - | 21.0 | 0.12 | - |

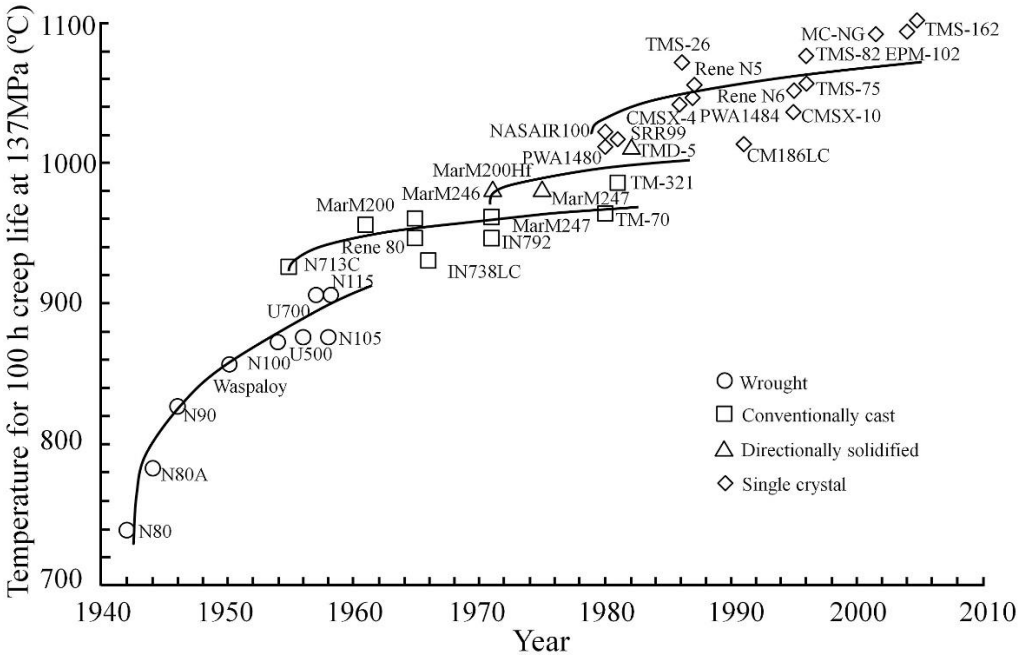

Figure 1 Historical development of high temperature superalloys [3].

### 2.1.1. Metallurgical Structure and Properties of Superalloys

Figure 2 shows an optical image of grain structure of Inconel 718 superalloy. Superalloys generally have the matrix of fcc structure which is denoted as γ which is a solid solution of Ni, Co, W and Cr, with hard precipitates of $Ni_3Al$, $Ni_3(Al, Ti)$. There are a wide variety of carbides

as the secondary phases in the matrix of superalloys, namely MC (TaC, MoC), $M_{23}C_6$, $M_6C$ as well as solid-solution hardeners and precipitate phases. These phases are responsible for strength of the superalloys by obstructing the dislocations and form a protective surface oxide film of $Cr_2O_3$ [1].

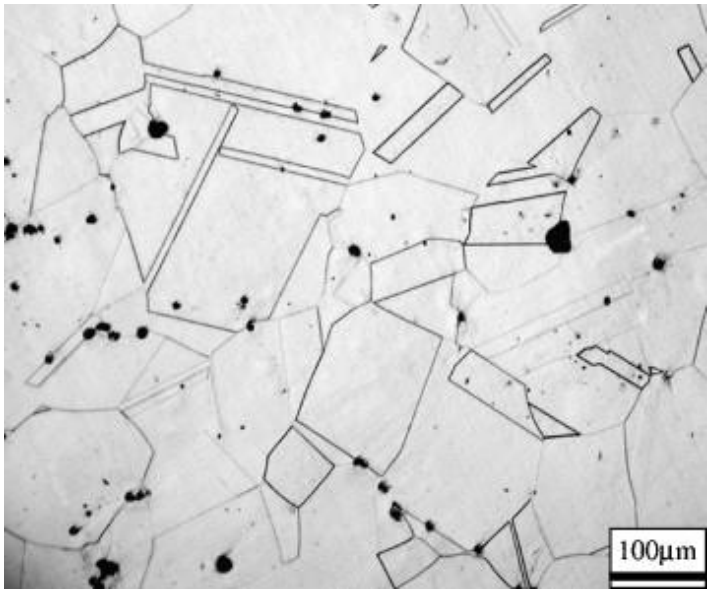


Figure 2 Optical micrograph of the annealed Inconel 718 superalloy showing grain boundaries and twinning [4].

$\gamma'$ and $\gamma''$ are the most important phases which are mostly found in nickel- and iron-nickel-based superalloys. $\gamma'$ has a fcc ordered $Ni_3$(Al, Ti) and $\gamma''$ has a bct ordered $Ni_3Nb$ atomic structures (Figure 3a). Other phases are $\eta$ which is hexagonal ordered $Ni_3Ti$ and $\delta$ orthorhombic $Ni_3Nb$ intermetallic compounds that can be found in nickel- and iron-nickel-based superalloys. In addition, other elements such as boron, zirconium and hafnium are added to these alloys which account for superalloys' mechanical and chemical properties.

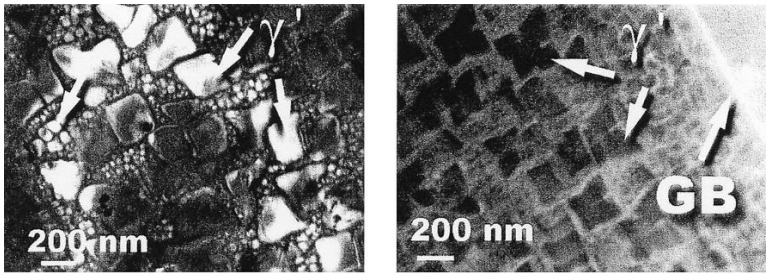


(a) (b)

Figure 3 (a, b) TEM micrographs of superalloy N18 showing the presence of four populations of γ′ precipitates [5].

### 2.1.2. Application of Superalloys

Nickel-based superalloys are mostly used in high-temperature applications such as components in aircrafts operating at 850 °C due to their high creep resistance. They are usually precision-cast to their final shape because of difficulties in machining of these alloys [6].

They also are utilized as chemical and petrochemical equipment parts such as disks, bolts, shafts, valves, cases, blades and vanes. Medical components and heat treatment equipment as well as nuclear power systems and chemical and petrochemical industries are other areas of application of these alloys [7, 8]. The high interest in use of superalloys in such critical application arises from their special combination of properties such as high strength, strong corrosion resistance, excellent thermal fatigue properties and thermal stability [9]. Figure 4 depicts an example of nickel-based superalloys used in various parts of a jet engine. Almost 50% of the weight of a jet engine is made up of Inconel 718 [10].

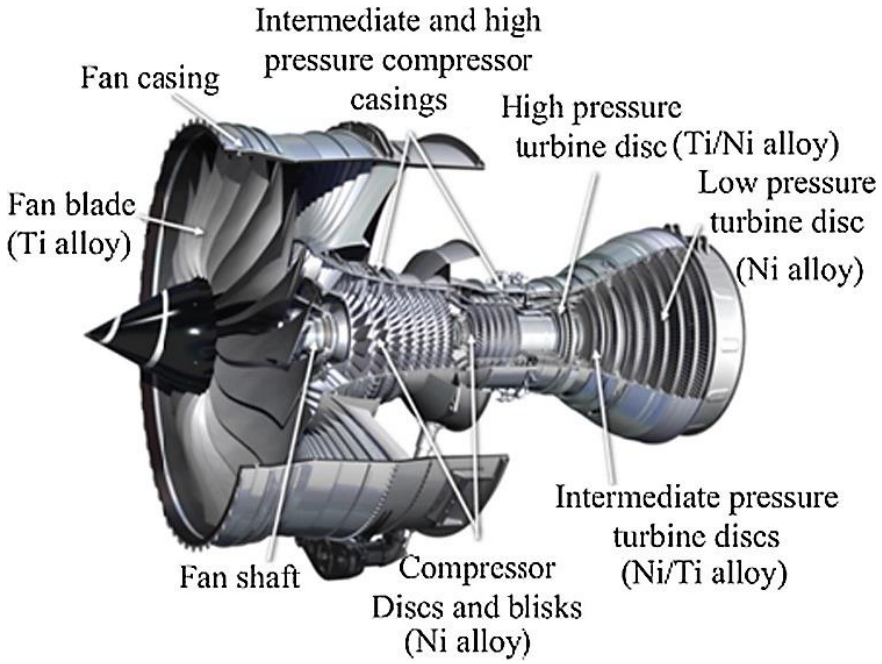


Figure 4 Rolls-Royce XWB Turbofan engine with the major components and its primary materials selection [10].

## 2.2. METAL CUTTING

In this section, the most important metal cutting principles, namely orthogonal and oblique cutting models, chip formation mechanism, cutting force model, stress distribution and cutting temperature during the metal cutting process are summarized.

### 2.2.1. Metal Cutting Principles

*Conventional machining* processes involve metal cutting principles in which mechanical force is used in order to remove *chips* from the workpiece material. They consist of various processes such as turning, milling, broaching, sawing (Figure 5).

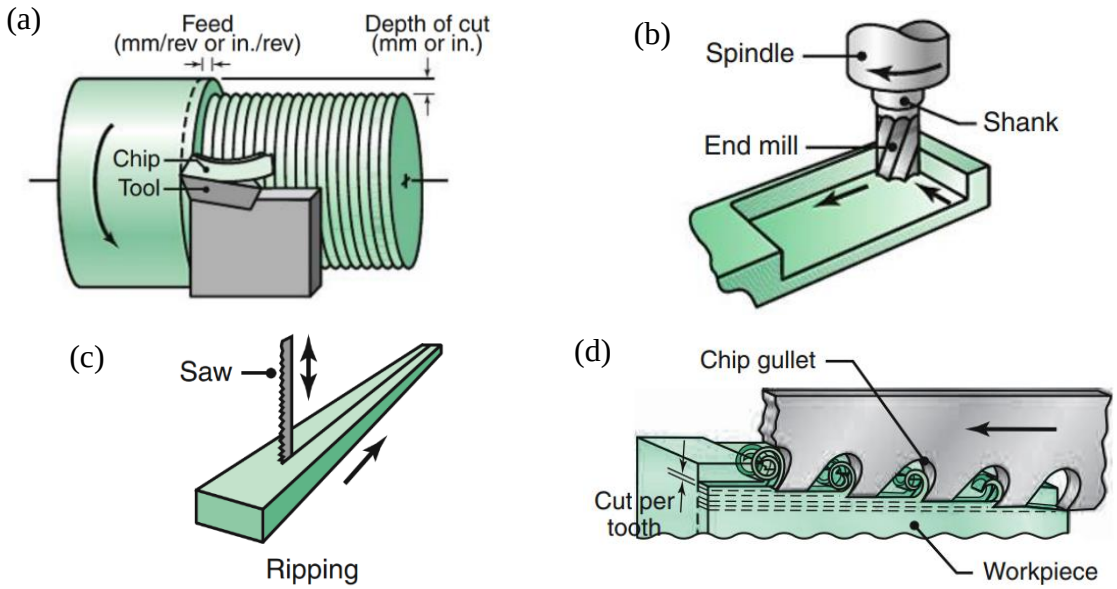


Figure 5 Schematic illustration of some machining processes: (a) turning, (b) milling, (c) sawing and (d) broaching [11].

*2.2.1.1. Orthogonal cutting model*

To simplify the complex metal cutting process, a two-dimensional model, also called *orthogonal cutting model*, was proposed by M.E. Merchant in early 1940s (Figure 6a). According to this model, a wedge-shaped cutting tool, possessing a predesigned rake (α) and clearance angles, penetrates into the workpiece material by application of cutting force, resulting in removal of *chip*, leaving a newly machined surface behind. Figure 6b shows the primary deformation zone in which the chip forms as a result of shearing action at a specific *shear plane angle* (ϕ). Also, in this figure the secondary deformation zone is illustrated in which chip slides over rake face of the tool.

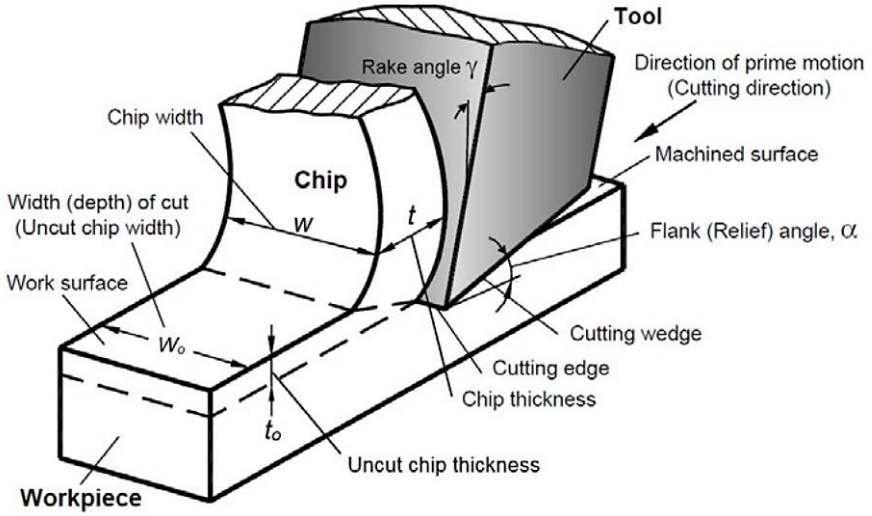


(a)

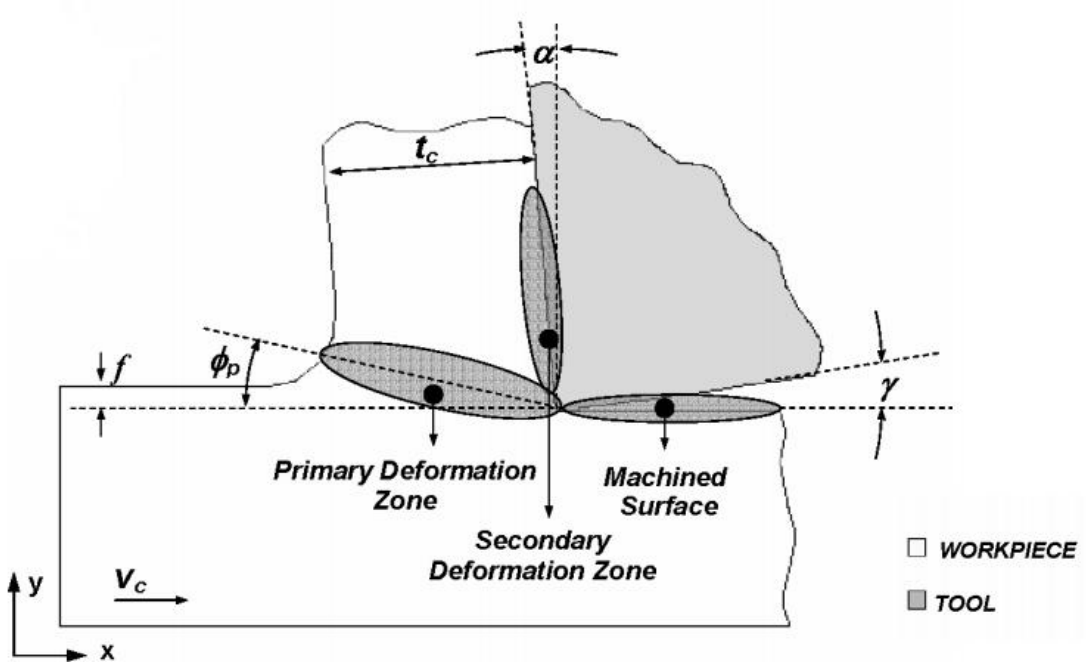


(b)

Figure 6 (a) Orthogonal cutting model with a specific shear plane proposed by M.E. Merchant [12]. (b) Deformation zones in the metal cutting process [13].

Marchant's model of chip formation mechanism is used to develop a mathematical model for predicting the shear plane angle as shown in the Figure 7a. Figure 7b shows angular

relationships between the cutting speed ($V$), shearing speed ($V_S$) and chip speed ($V_C$) in the cutting zone. According to this figure, shear strain ($\gamma$) can be calculated by:

$$\gamma = \frac{AB}{OC} = \frac{AO}{OC} + \frac{OB}{OC} \quad (1)$$

$$\gamma = \cot\phi + \tan(\phi - \alpha) \quad (2)$$

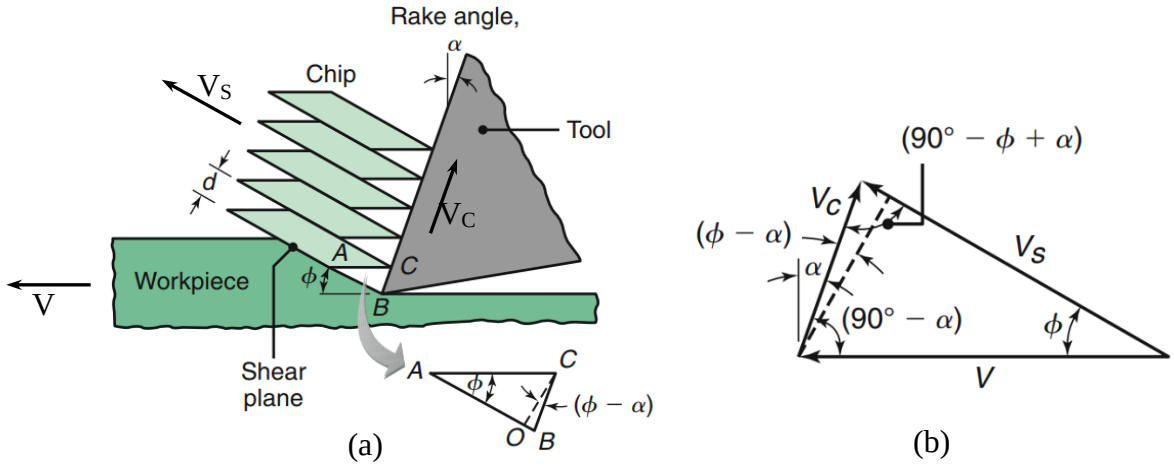


Figure 7 (a) Schematic illustration of basic mechanism of chip formation by shearing action, (b) angular relationships among the cutting speed (V), shearing speed (VS) and chip speed (VC) in the cutting zone [11].

Shear strain in machining can be as much as 5 or higher which is the highest among other manufacturing processes (Table 2). In addition, because the shearing happens in a very narrow zone in shear plane, the shear strain rate is very high. Consequently, the mechanics of metal cutting process (cutting force and power) greatly depends on the forces acting on the shear plane. As Figure 7a illustrates, chip thickness is dependent on the shear plane angle: the less the shear angle, the more the chip thickness ($t_c$). In order to find the relationship between shear angle and rake angle as well as coefficient of friction ($\mu$), it is assumed that the shear angle adjusts itself to minimize the cutting force or that the shear plane is a plane of maximum shear stress. Therefore, the following expression can be drawn:

$$\phi = 45° + \alpha - \beta \quad (3)$$

where $\beta$ is the friction angle which is related to the coefficient of friction at the tool-chip interface by the following relation:

$$\mu = tan\beta \quad (4)$$

Table 2 Typical ranges of strain in manufacturing processes [11]

| Process | True strain |
|---|---|
| Machining | 1-10 |
| Superplastic forming | 0.2-3 |
| Extrusion | 2-5 |
| Forging, rolling | 0.1-0.5 |
| Sheet metal forming | 0.1-0.5 |
| Wire and tube drawing | 0.05-0.5 |

*2.2.1.2. Oblique cutting model*

Generally, in real metal cutting processes, cutting tools have complex geometries being oblique rather than orthogonal in the cutting edge. As can be observed in Figure 8a, the inclination angle of the cutting tool, *i*, results in helical chips. In this figure, $\alpha_c$ is chip flow angle and $\alpha_t$ is normal rake angle. Assuming that $\alpha_c = i$ (this assumption has been verified experimentally), and considering that both $i$ and $\alpha_t$ can be measured directly, the effective rake angle can be calculated by:

$$\alpha_e = sin^{-1}(\sin^2 i + \cos^2 i \sin \alpha_t) \quad (5)$$

Note that, as inclination angle increases, the effective rake angle increases and the chip becomes thinner and longer, and thus, the cutting force decreases. The influence of the inclination angle on chip shape is shown in Figure 8b.

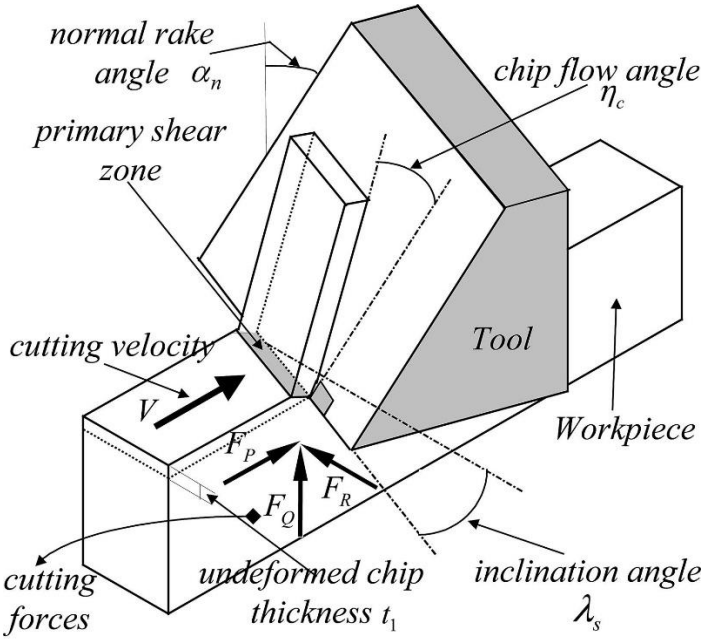


Figure 8 Geometrical view of oblique cutting [14].

*2.2.1.3. Chip types and formation mechanisms during the metal cutting process*

In actual machining process, various forms of chip are produced which can be categorized into three main groups:

- Continuous chips,
- Discontinuous chips,
- Serrated (segmented) chips.

Cutting ductile material and selecting high cutting speeds as well as high rake angles promote creation of continuous chips (Figure 9a). However, because of the high contact area between the tool rake face and the produced chip in the secondary shear zone (Figure 9b), formation of continuous chip results in high friction forces in this region. Thus, this can lead to high tool wear and poor surface finish, making continuous chips undesirable. In addition, entanglement of the chips around the toolholder, fixture and workpiece, especially in the computer-controlled machines, exacerbates the cutting condition. Discontinuous chips are small segments of

material removed during the machining of brittle materials, cutting at very low or very high cutting speeds, large depth of cuts as well as presence of inclusions and impurities in the microstructure of workpiece material (Figure 9c). Serrated chips, on the other hand, are mostly seen in materials with low thermal conductivity and strength that decreases sharply with temperature (thermal softening). They are characterized by shear localization in a small zone in which high shear strain results in fracture in the chip while shear strain is remaining low in the large zones of chip body (Figure 9d).

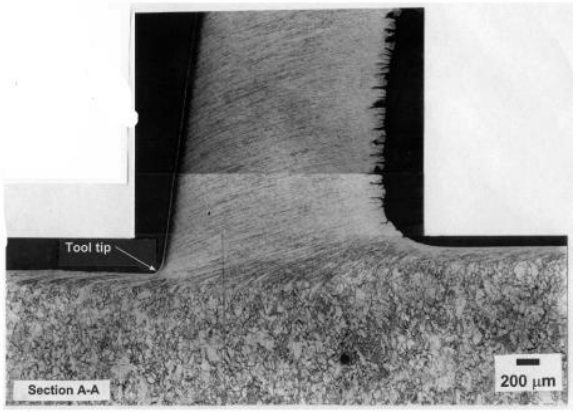


(a)

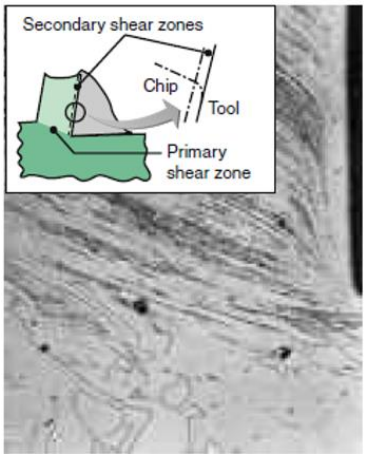


(b)

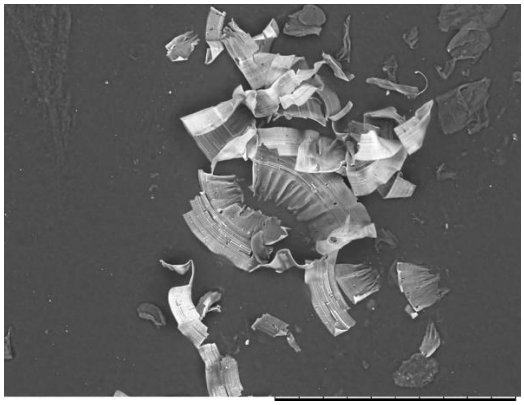

(c)

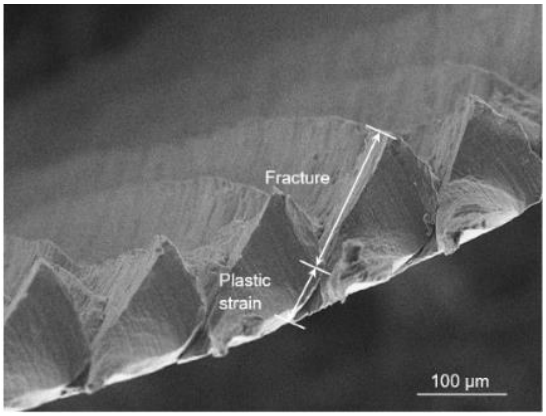


(d)

Figure 9 (a) Continuous chip with narrow, straight, and primary shear zone produced during orthogonal cutting of pure copper [15]; (b) continuous chip with secondary shear zone at the chip–tool interface [11]; (c) discontinuous chip produced during machining of Al6061 [16]; and (d) serrated (segmented) chip of Ti alloy formed under cryogenic cutting [17].

Serrated chips are produced as a result of localized plastic strain in a narrow zone which is called adiabatic shear bands (ASB) as shown in Figure 10a, b. As Figure 10 c and d show, the chip material undergoes plastic deformation up to a maximum length beyond which the material fractures as shown ($A'C'$). The chip segments remained attached to each other over a portion of length ($B'C'$) [17].

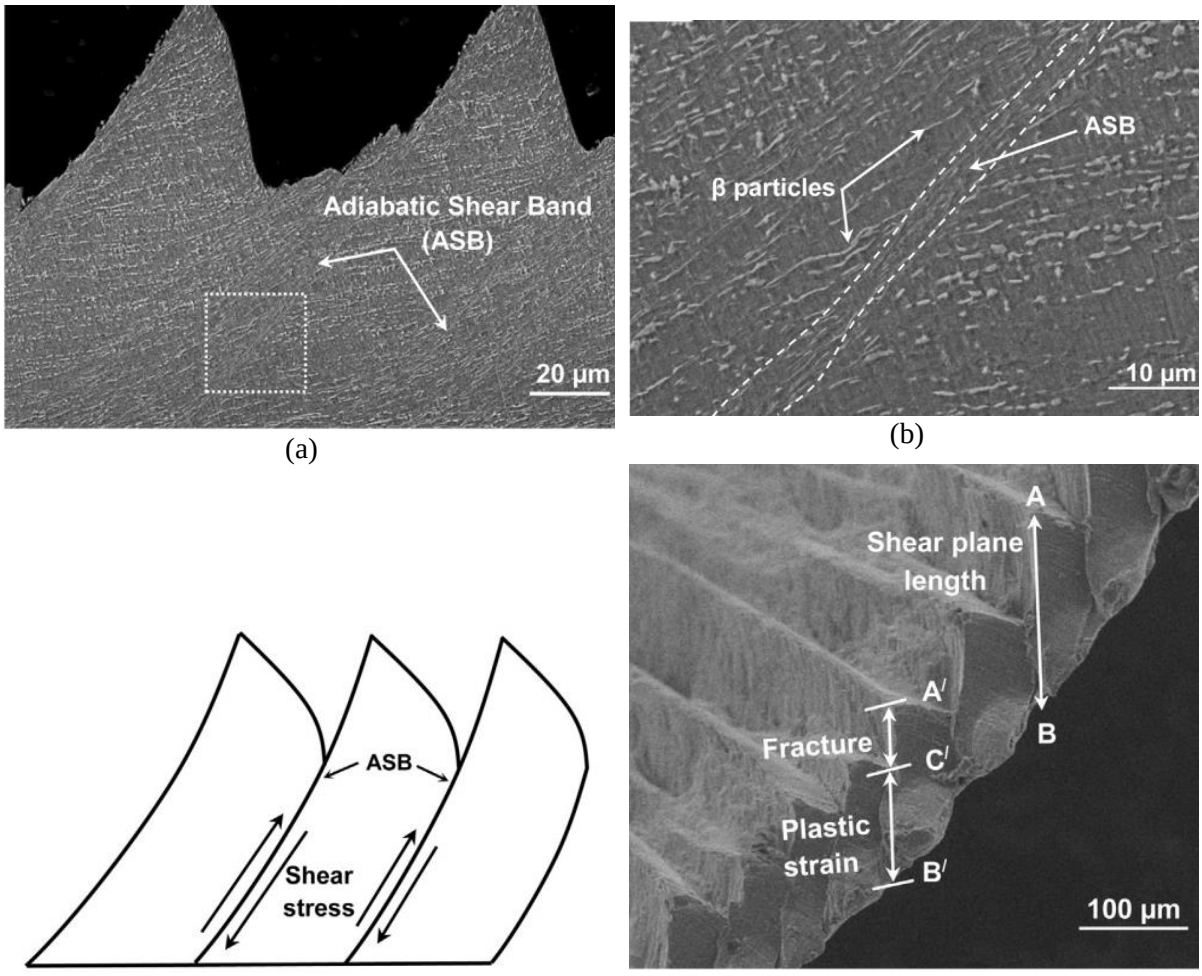


Figure 10 (a) Microstructure of the chip formed during machining of Ti alloy showing the shear localization, (c) Higher magnification of the zone marked by a white box in (b) showing the adiabatic shear band and b particles, (d) Schematic representation of a chip obtained from dry machining condition illustrating the formation of adiabatic shear bands (ASB) and intersegment shearing [17].

*2.2.1.4. Cutting forces in orthogonal cutting*

To model the cutting forces on the cutting edge during the machining process, a 2D model was developed by considering the frictional force acting on the tool-chip interface on the rake face (*R*) as well as the force between workpiece and the chip along the shear plane (R′) (Figure 11a). By resolving these forces into its components, the forces in horizontal and vertical directions, $F_P$ and $F_Q$, along and perpendicular to the shear plane, $F_S$ and $N_S$ as well as along and perpendicular to the tool face, $F_C$ and $N_C$ are obtained. The circle of forces shown in the Figure 11b is achieved by plotting these forces at the tool tip [18]. Geometrical analysis of horizontal and vertical forces results in determination of shear and frictional forces:

$$F_S = F_P \cos \emptyset - F_Q \sin \emptyset \tag{6}$$

$$N_S = F_Q \cos \emptyset + F_P \sin \emptyset = F_S \tan(\emptyset + \beta - \alpha) \tag{7}$$

Similarly, coefficient of friction ($\mu$) can be calculated:

$$\mu = \frac{F_C}{N_C} = \frac{F_P \sin \alpha + F_Q \cos \alpha}{F_P \cos \alpha - F_Q \sin \alpha} = \frac{F_Q + F_P \tan \alpha}{F_P - F_Q \tan \alpha} \tag{8}$$

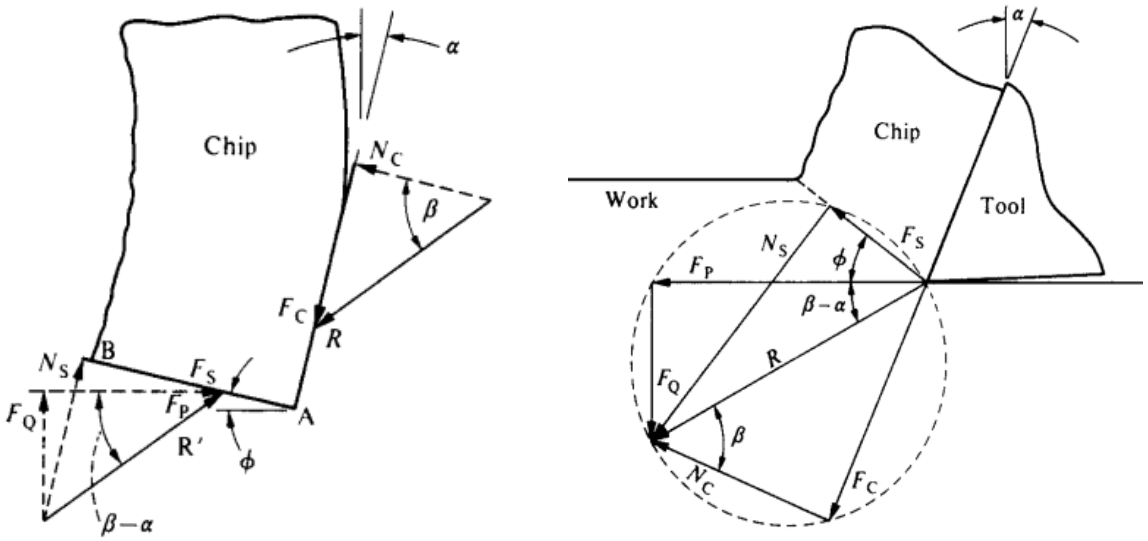


(a) (b)

Figure 11 (a) Free body diagram of chip and (b) composite cutting force circle during orthogonal cutting process [18].

*2.2.1.5. Stresses generated during metal cutting process*

Determination of stress distribution on the tool-chip interface is crucial in analyzing the cutting processes and the obtained surface quality. Although in actual machining practice, stress distribution can be very complex, some models have been proposed in order to simplify it. Zorev [19] proposed a model in which seizure action occurs at the tool-chip interface near the cutting edge while sliding happens beyond the sticking region. In this model, compressive stress ($\sigma_c$) is assumed to follow the following expression at any point:

$$\sigma_c = qx^y \tag{9}$$

where $x$ is distance from the point $B$ where the chip breaks contact with the tool, and $q$ and $y$ are both constants. As can be observed, compressive stress is maximum at the cutting edge and has the value of zero at the point where chip breaks contact with the rake face of the tool. The shear stress, on the other hand, has a more uniform distribution along seizure region on the rake

face. The maximum value of shear stress is less than that of compressive stress. Shear stress falls to zero in the sliding region of the tool-chip contact [20].

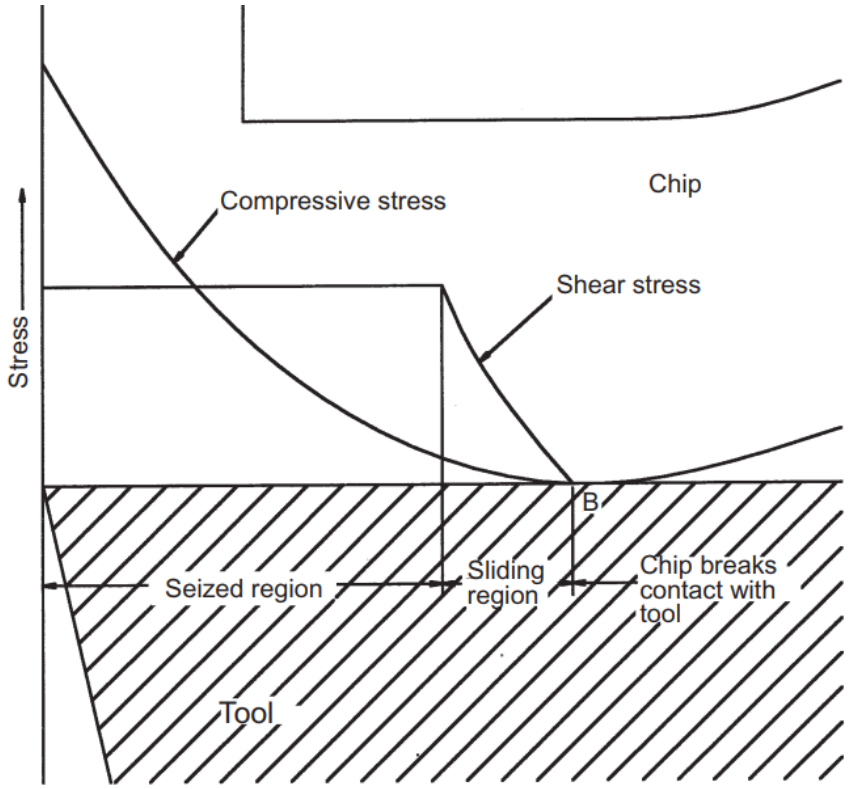


Figure 12 Model of stress distribution during cutting [20].

To measure the stress distribution on the tool surface in the real cutting conditions, several methods have been developed including carry out the cutting process using split tools, using tools of different strengths and using photoelastic polymers tools. Bagchi and Wright [21] used photoelastic sapphire tools in the cutting process in order to investigate the stress distribution during the cutting of AISI 1020 and 12L14 steels, and 360 brass workpiece materials. Figure 13 illustrates their experimental arrangements.

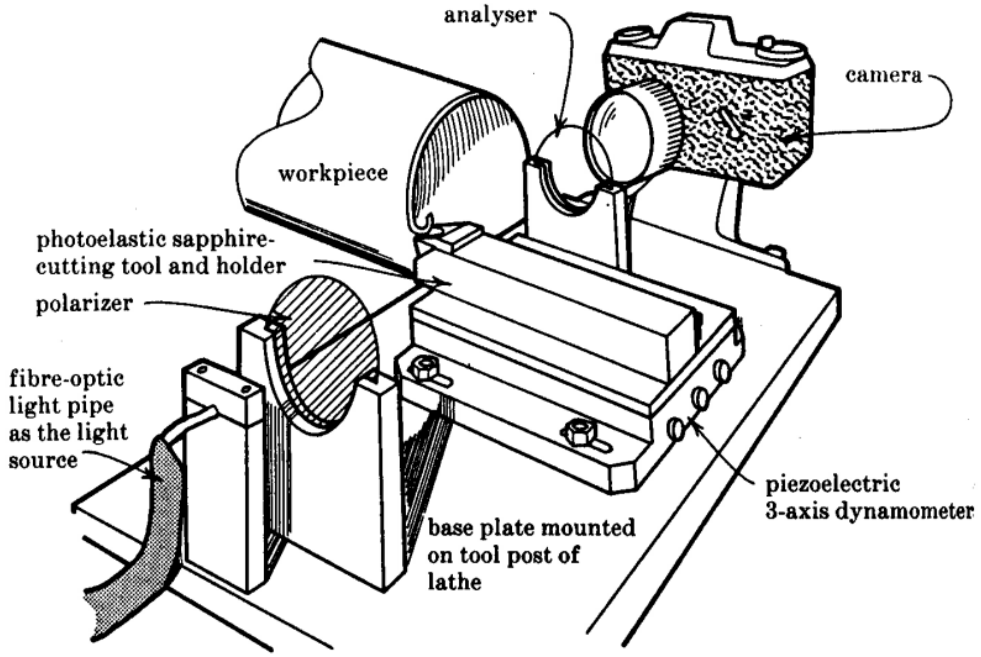


Figure 13 View of the experimental arrangement used for photoelastic stress analysis in machining [21].

Fast-frame photography allowed a series of images to be collected (Figure 15). Two sets of images are achieved in these experiments. The first set of color images provided isochromatic fringes which corresponds to positions where the difference in the principal stress values was equal to an integer value of wavelength. The second set were the black and white isoclinic fringes. These occur when either of the principal stresses were aligned with the polarizer. Bagchi and Wright [21] used the shear-difference method to calculate the normal and shear stresses from the obtained isochromatic and isoclinic fringes. Composite isochromatic and isoclinic fringes which were obtained during the machining of 12L14 steel at 75 $m.min^{-1}$ at an uncut chip thickness of 0.132 mm 0.381 mm are shown in Figure 14a, c. The corresponding calculated shear and normal stresses are shown in Figure 14b, d. These figures confirmed Zorev's stress model depicting that normal stress is maximum at the tool tip and it decreases

along the tool-chip interface. Shear stress has a lower maximum value than normal stress and falls to zero at a distance away from the tool edge.

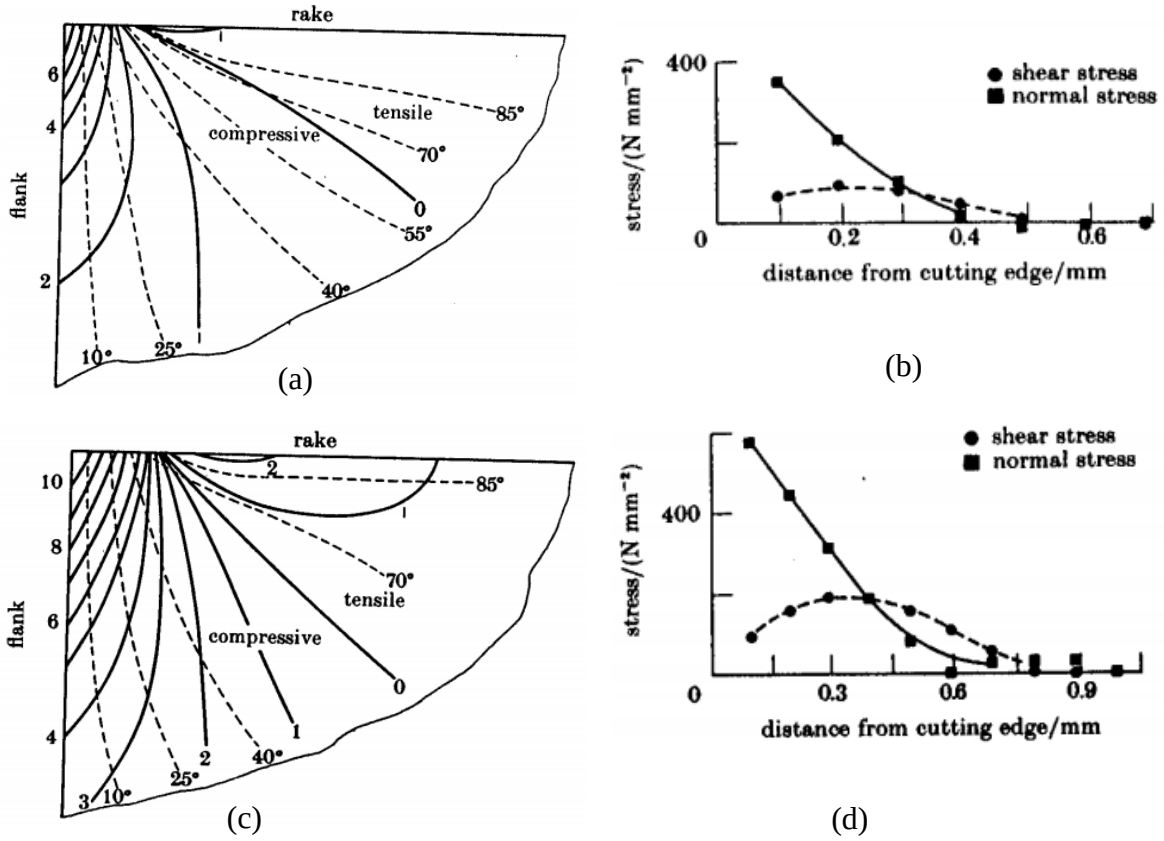


Figure 14 (a) Composite isochromatics and isoclinics obtained during the machining of 12L14 steel at 75 m min-1 at an uncut chip thickness of (a) 0.132 mm (c) 0.381 mm (Solid lines, isochromatics; dashed lines, isoclinics). Normal and shear stress distributions along the rake face surface during the machining of 12L14 steel at 75 m min-1 and an uncut chip thickness of (b) 0.132 mm, (d) 0.381 mm [22].

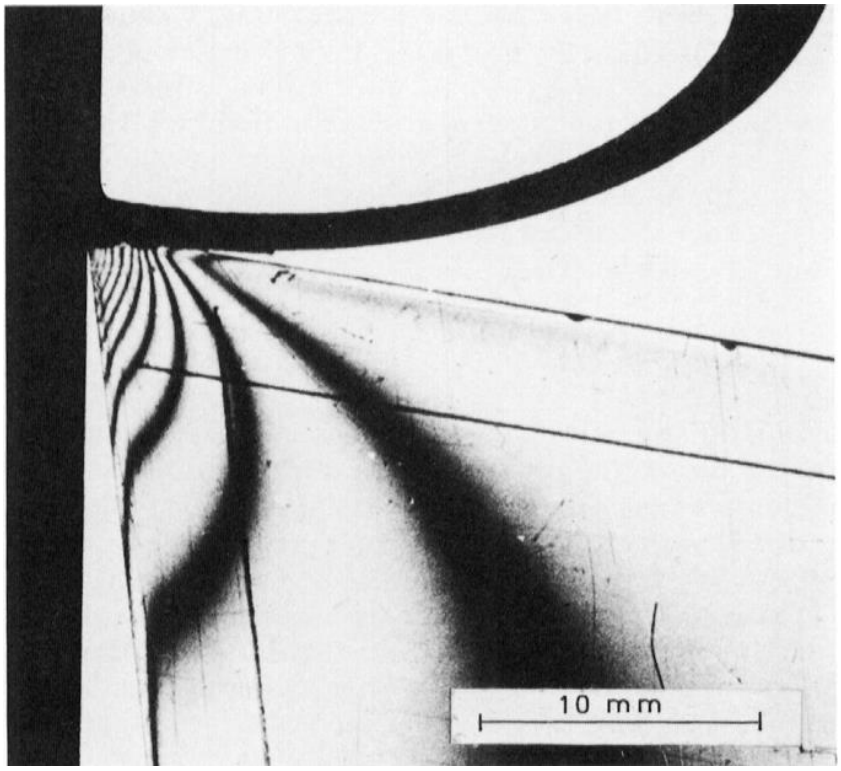


Figure 15 Stress distribution in photo-elastic model tool when cutting lead [23].

As it was shown in the Figure 14b and d, shear stress is low immediately behind the cutting edge. It increases to a maximum value and then decreases again in a distance away from cutting edge where the chip leaves the rake face of the tool. This was also shown by Doyle, et al. [24] in machining copper at 120 m/min for 50 s (Figure 16). It is observable that immediately after the tool tip, chip material flows around the cutting edge.

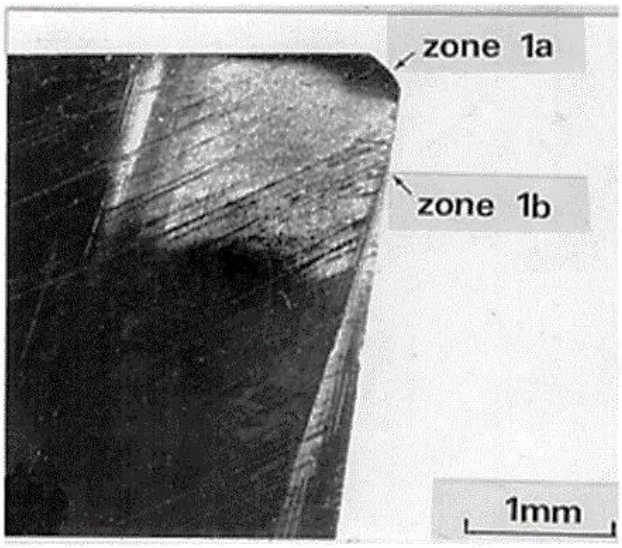


Figure 16 Rake face photographs at ×25 magnification confirming the reduced transfer and hence shear stress in zone 1a. From machining copper at 120 m/min$^{-1}$ for 50 seconds. Longer cutting times "clean-up" any organic films on rake face, creating increased amounts of the seizure type contact as time progresses [24].

Figure 17a and b shows the experimental and numerical results of strain distribution in the workpiece material during the machining process [25]. The maximum equivalent strain was at the tool tip. Secondary deformation zone showed higher amount of strain than primary zone. This also can be observed in Figure 18a, b which shows the metallography of quick-stop section through copper chip machined at a slow speed of 1.5 m/min for 300s. The regions similar to zone 1a and zone 1b, which was shown in Figure 16, can be seen in Figure 18a. Figure 18b shows the flow lines of the workpiece material around the tool tip. The length of the Zone 1a (OK) is almost 0.3 and the total length of zone 1a and zone 1b (KQ) is 3 mm. Extremely high strain of material during the turning process can be seen in (Figure 18b). Material is deformed in the primary shear zone, AB. As the cutting tool penetrates in the material, the amount of deformation increases from AD to AH to the extent that material is extremely deformed near the rake face of the tool, KLMN.

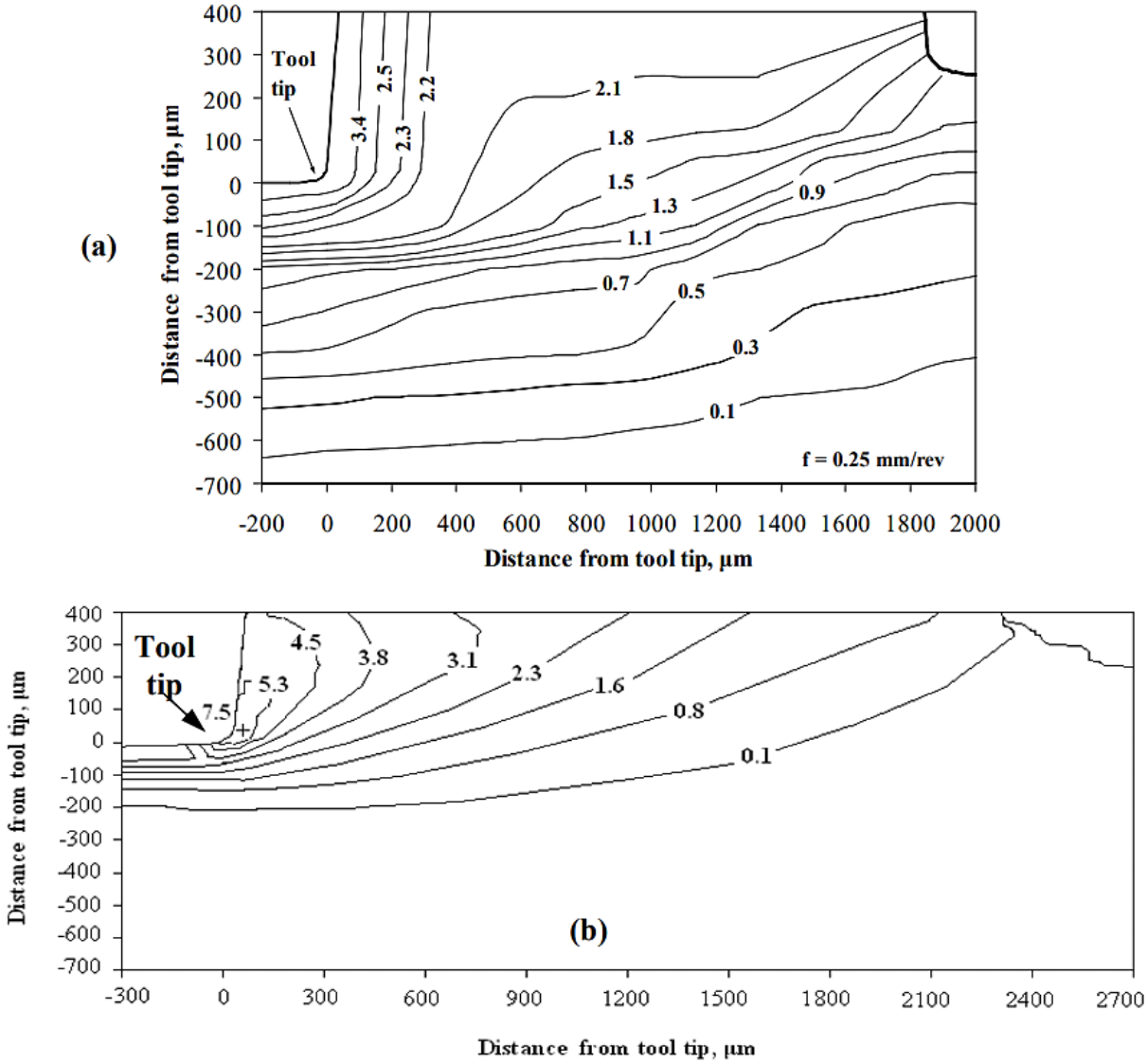


Figure 17 Strain distribution in the material during machining of Al 1100 which was determined (a) experimentally and (b) by Eulerian model [25].

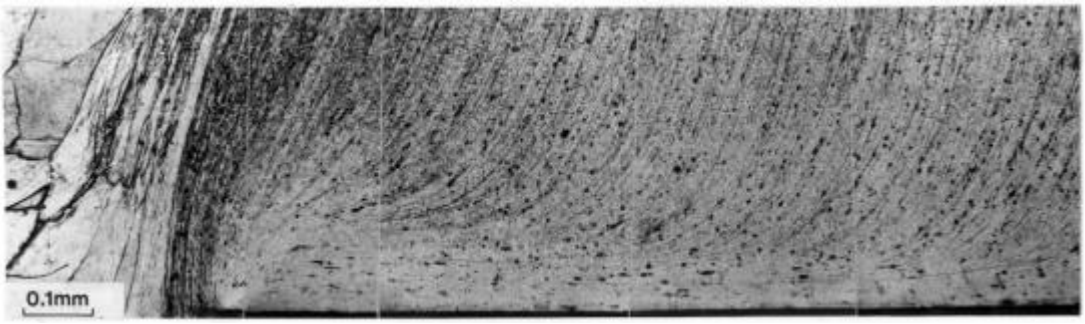


(a)

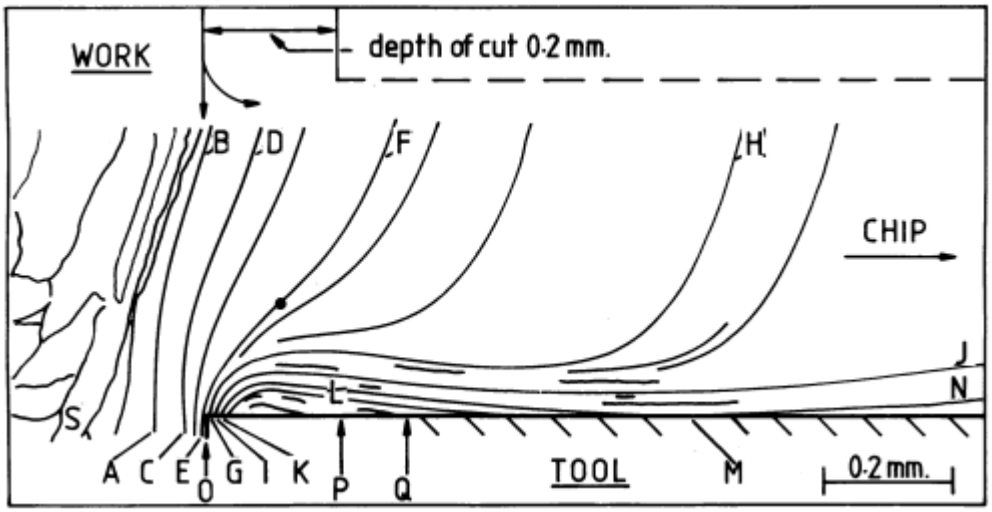


(b)

Figure 18 (a) Quick-stop section through copper chip machined at a slow speed of 1.5 m $min^{-1}$ for 300 seconds. (b) Tracing of flow lines [22].

Ni, et al. [26] showed the microstructural variation in different part of the cutting area in machining of Al 1100 alloy (Figure 19a, b). Deformation free zone (DFZ) represented the microstructure of as-received material before cutting process. In the primary deformation zone (PDZ), the high plastic deformation results in highly elongated grains (zone 2 and 3). In the secondary deformation zone (SDZ), recrystallization results in grain growth and equiaxed grains.

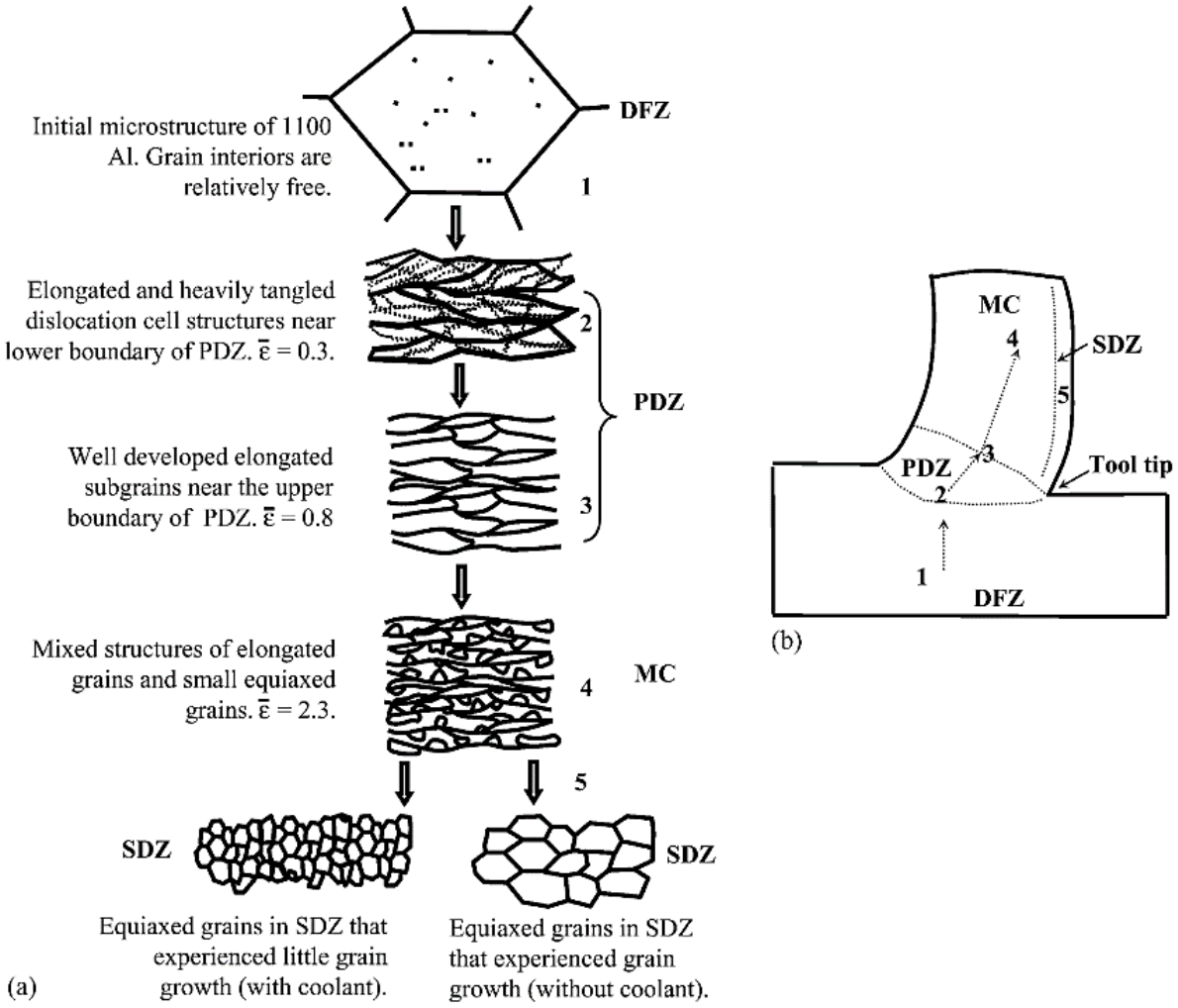


Figure 19 (a) Schematic illustration of the main steps of microstructural evolution in 1100 Al subjected to orthogonal cutting. (b) The sequence of grain refinement events shown on the cross-section of the material ahead of the tool tip [26].

*2.2.1.6. Temperature generated during the metal cutting process*

Cutting energy consumed during the machining process is expended for plastic deformation and overcoming friction in the tool/chip interface. Cutting heat is generated in the three deformation zones which was discussed in Section 2.2.1.1. Figure 20 shows three heat generation zones in machining process.

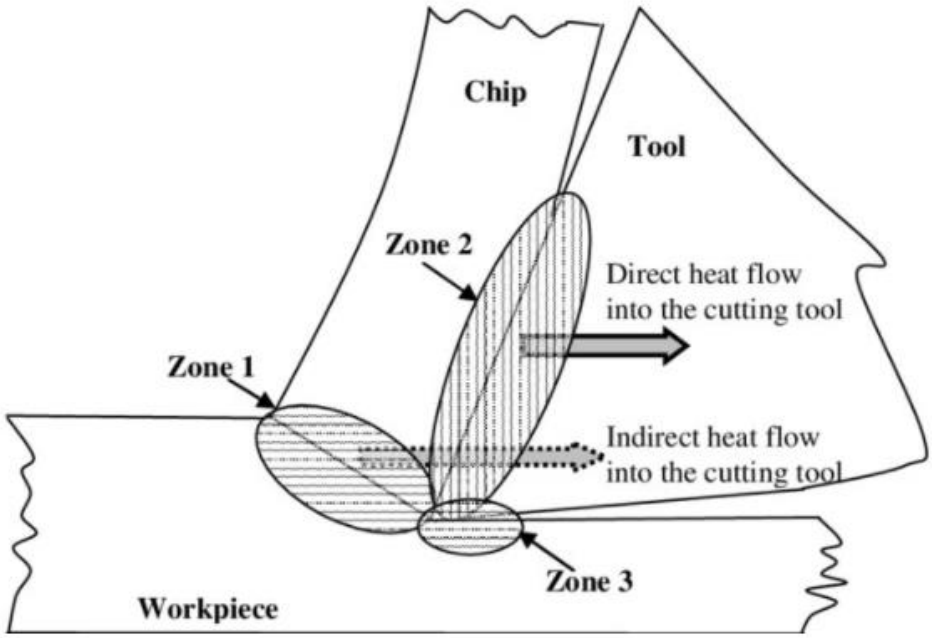


Figure 20 Heat generation zones during the machining process [27].

### 2.2.2. Turning Process

Turning process is used for manufacturing of parts that have a basically round shape (axisymmetric parts). In this process, the workpiece rotates while the cutting tool is fixed. The machine tool on which the turning process is conducted is called *turning machine* or *lathe*. Typical conventional and CNC lathe machine and their components are shown in Figure 21. Versatile processes ranging from straight and taper turning to drilling and threading can be done on lathe machines (Figure 22).

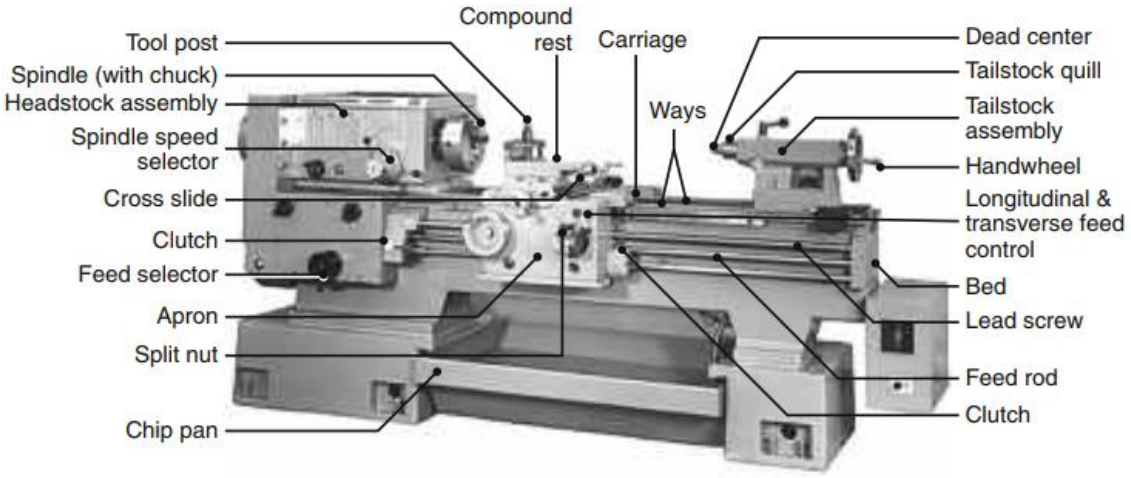


(a)

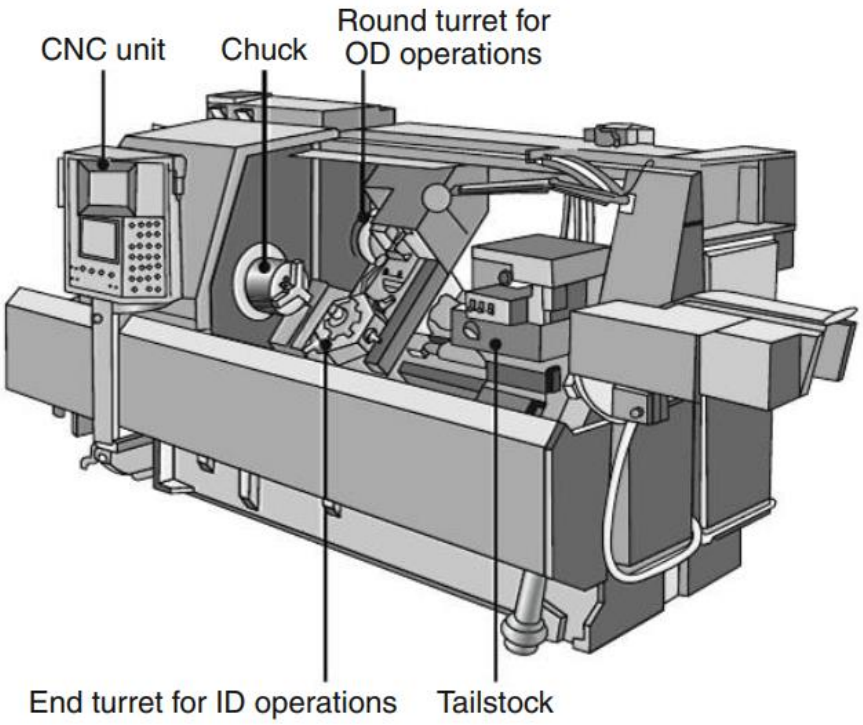


(b)

Figure 21 (a) A typical lathe, (b) a computer-controlled (CNC) lathe and their various components [11].

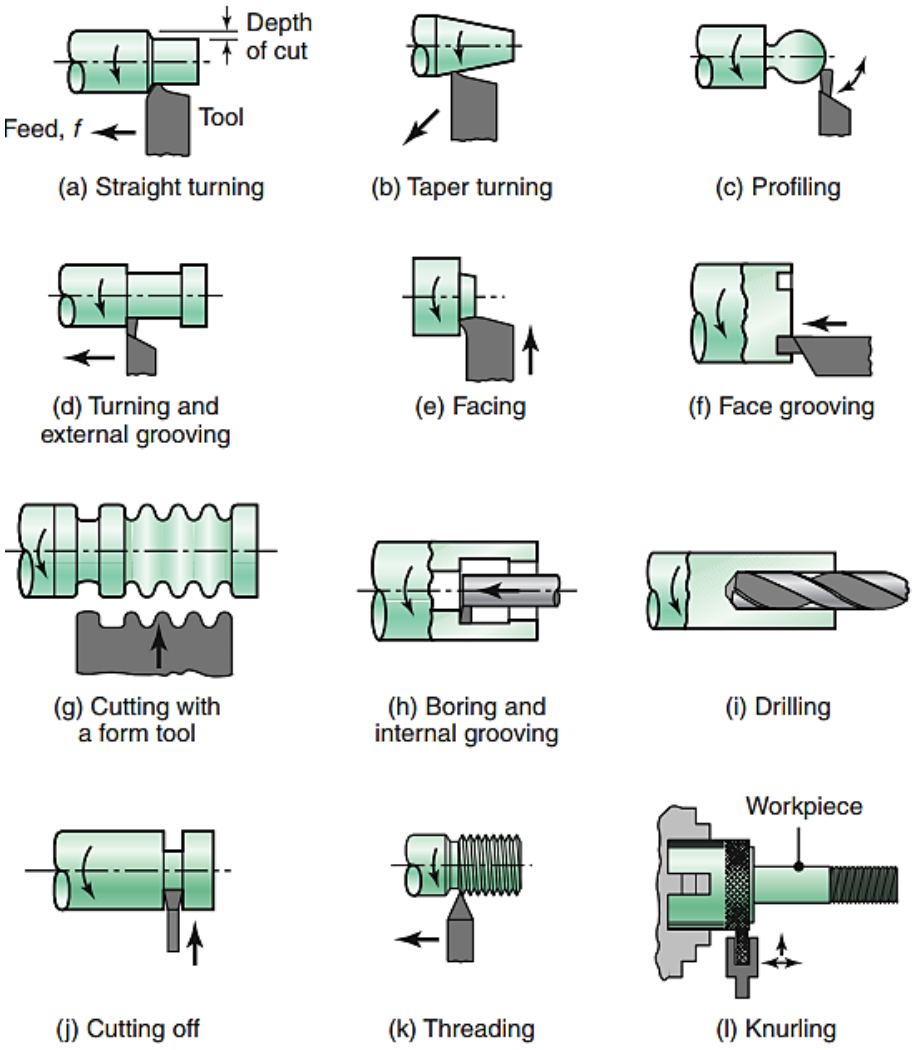


Figure 22 Various processes that can be done on a lathe machine [11].

*2.2.2.1. Turning tools geometry*

Rake and clearance angles in orthogonal and oblique cutting were discussed in the Section 2.2.1.1. However, cutting tools used in turning process have more complex geometries so that the chip can flow smoothly during the cutting process. Figure 23a-c shows a typical turning tool from different views.

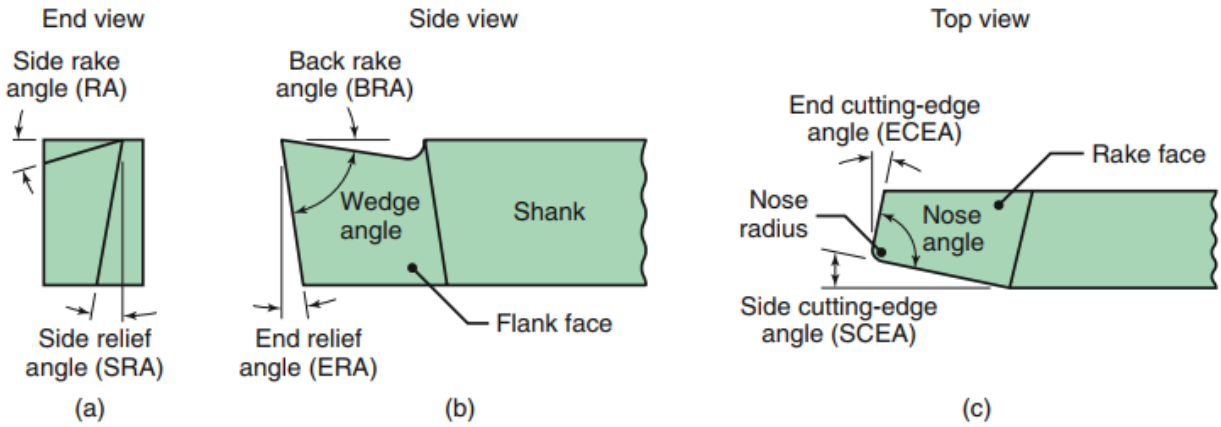


Figure 23 Designation for a typical cutting tool for turning process from (a) end view, (b) side view and (c) top view [11].

*2.2.2.2. Cutting parameters in turning process*

Cutting speed, feed rate and depth of cut are the cutting parameters in turning of which proper selection of value of these parameters has a great influence on the machining performance (Figure 24a). Cutting speed is defined as the length of tool material that pass from the tool tip. Feed rate is the length that tool travels along the workpiece per one rotation of the spindle. Depth of cut is defined as the length of the cutting tool which travels into the workpiece. It is noteworthy that feed rate and depth of cut should not be confused in the turning process and Marchant's model (Figure 6). Figure 24b shows cutting parameters in turning process as well as the Marchant's model. From this figure, it is clear that feed rate in turning is the same as the depth of cut in the orthogonal cutting model.

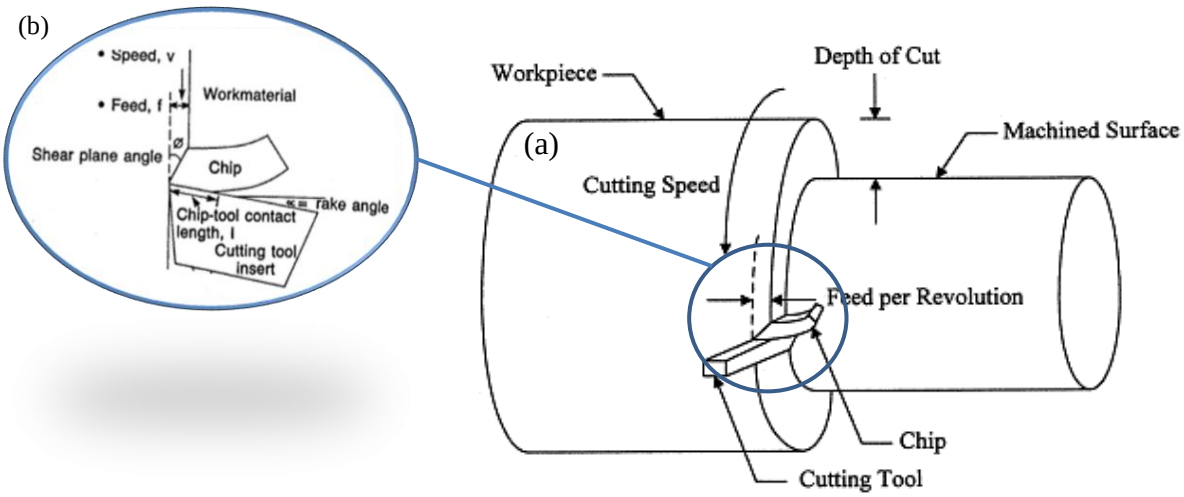


Figure 24 Cutting parameters, namely cutting speed, feed rate and depth of cut (d) in turning process [28]. (b) Transition of cutting parameters to turning process into Merchant's model [22].

*2.2.2.3. Turning tool materials*

Cutting tool are made up of materials that can withstand special environment existing in the metal cutting processes in which cutting tool encounters high stresses and temperatures in primary and tertiary cutting zones. Therefore, a cutting tool should:

- Retain its hardness at the elevated cutting temperatures,
- Have deformation resistance at high temperature of the machining process,
- Have high fracture toughness to resist edge chipping and premature failure of the cutting edge,
- Have low thermal affinity with respect to the workpiece material to resist crater wear on the rake face of the tool,
- Have high thermal conductivity to dissipate the heat generated in the cutting area.

The mostly utilized cutting tool materials in the order of development dates are carbon steel, high-speed steels (HSS), tungsten carbide-cobalt tools (WC-Co), ceramics, cubic boron nitride (CBN) and polycrystalline diamond (PCD) (Figure 25). Each group of the mentioned tool materials are divided into several sub-group categories. Generally, as the materials developed

from HSS to PCD, the toughness of the materials decreased, while their hardness (Figure 26a) and their resistance to elevated cutting temperatures (Figure 26b) increased.

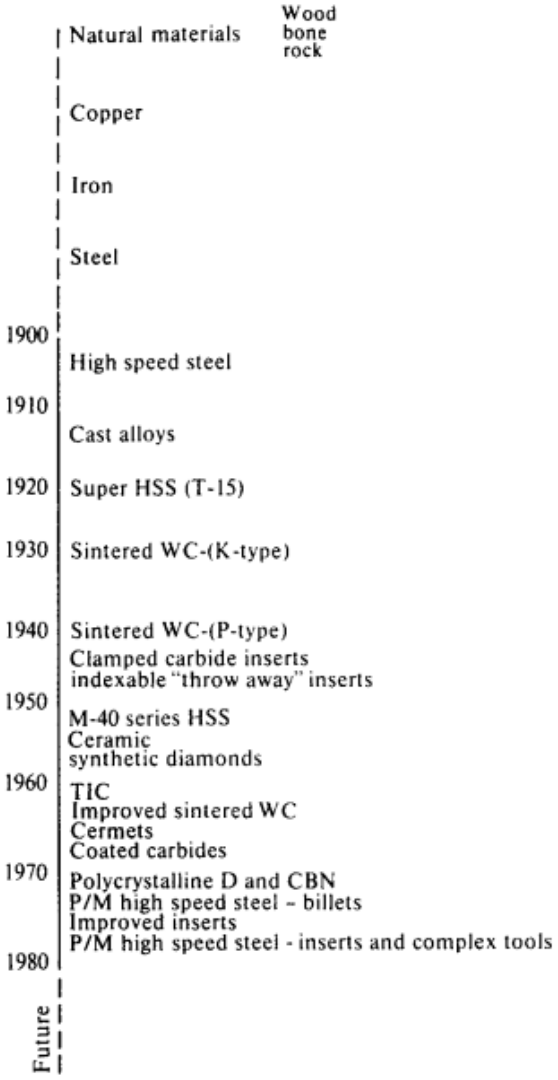


Figure 25 Various cutting tool materials in the order of their introduction dates [29].

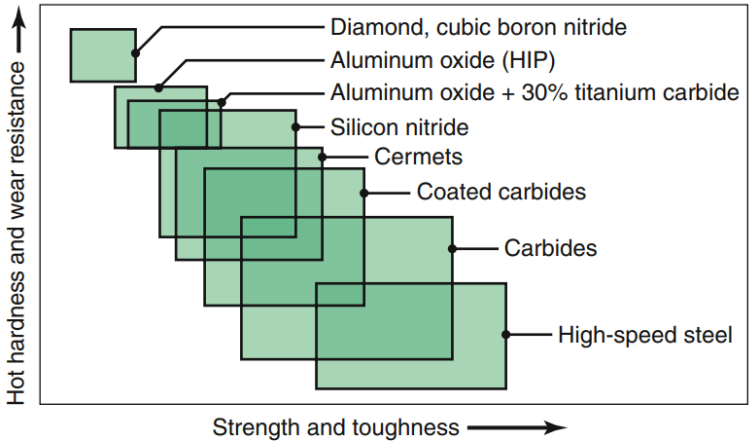


(a)

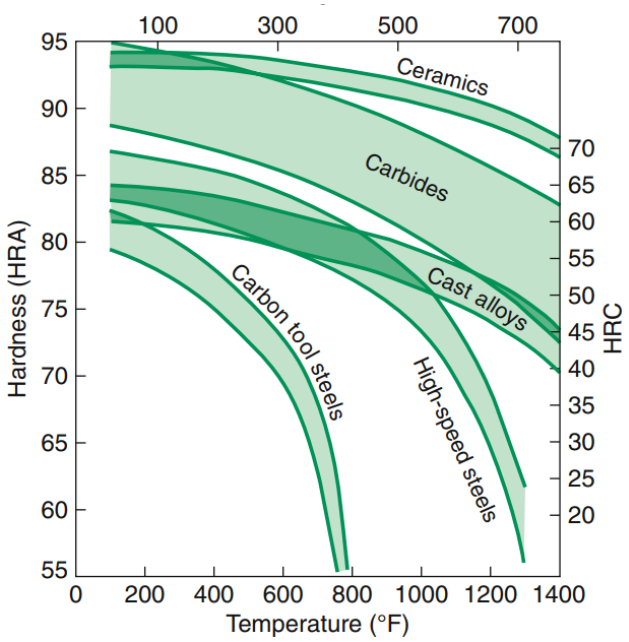


(b)

Figure 26 (a) Ranges of mechanical properties for various groups of tool materials. (b) hardness of different cutting materials as a function of temperature [11].

### *2.2.2.4. Tool Wear*

Due to the severe condition during the cutting process in which high stresses and temperatures are concentrated in a small area near the tool edge (see Section 2.2.1), the cutting tool is subject to various types of tool wear. Figure 27a-k show different tool wear types that are observed on the cutting tools after metal cutting process. One or several of these wear types can be developed

at the same time during cutting. Formation of tool wear type depends on the cutting parameters, cutting environment, tool and workpiece materials, etc. Flank (Figure 27a) and crater (Figure 27b) wear types are the mostly investigated ones and are generally used as the tool life criteria in various cutting processes. Figure 28 shows the ISO 3685 standard which is mostly used in measurement of tool wear and evaluation of effect of machining parameters (such as cutting speed, tool material and geometry, cutting fluid, etc) on the tool life.

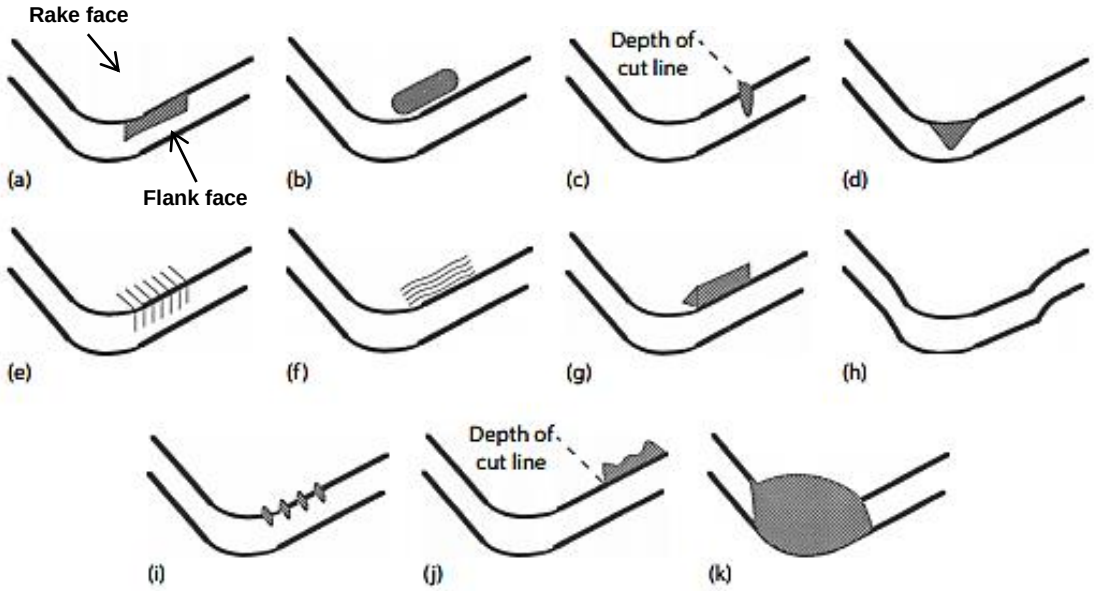


Figure 27 Types of wear on cutting tools: (a) flank wear, (b) crater wear, (c) notch wear, (d) nose radius wear, (e) thermal cracks, (f) mechanical cracks, (g) built-up edge, (h) gross plastic deformation, (i) edge chipping, (j) chip hammering, (k) gross fracture [30].

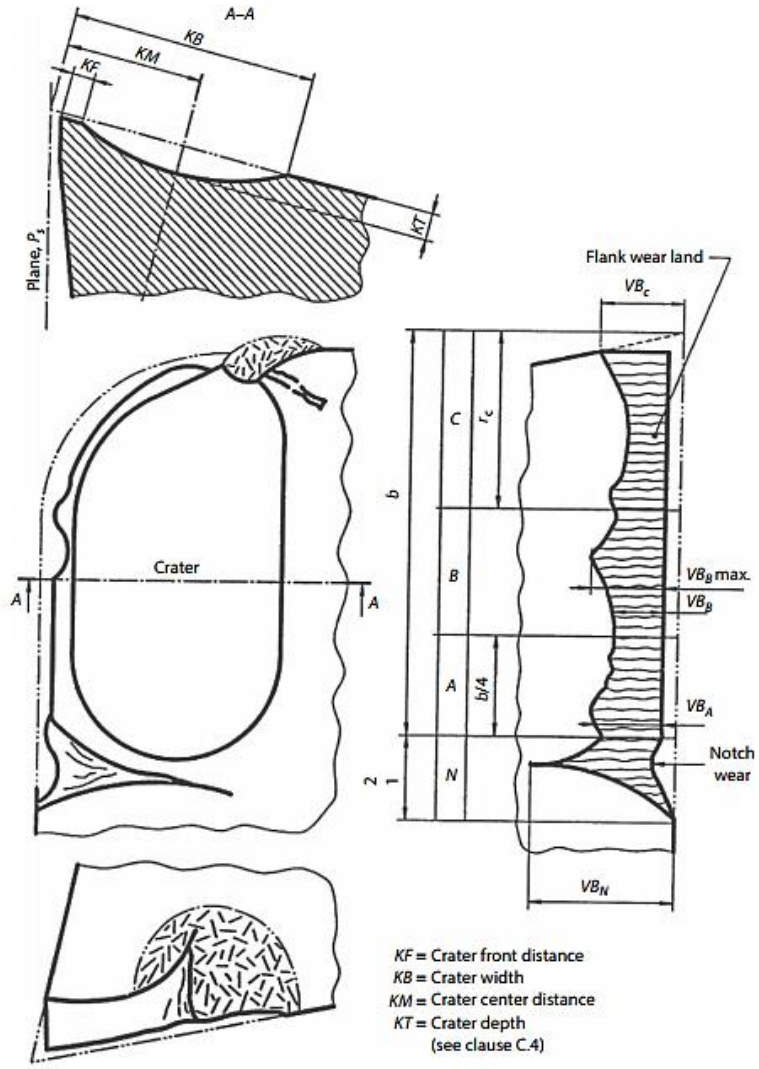


Figure 28 Characterization of flank wear land and rake face crater wear according to ISO 3685 standard [31].

### *2.2.2.5. Surface roughness*

Generally, the primary goal of cutting process is to achieve the best possible part quality. Thus, surface roughness is one the most important parameters in metal cutting processes. Several surface parameters are developed in order to characterize different aspect of the produced surface. $R_a$ and $R_z$ are the mostly used surface roughness parameters. $R_a$ is determined from deviation of peaks and valleys about the center line within the evaluation length. For this reason,

it is also called arithmetic average roughness or center line average (CLA). Considering the parameters shown in the Figure 29a, $R_a$ can be calculated by the following equation [32]:

$$R_a = \frac{1}{l_r}\int_0^{l_r}|z(x)|dx \quad (10)$$

It is the most popular parameter for a machining process and product quality control, since it is easy to measure even in the least sophisticated profilometers and gives a general description of surface amplitude. However, it is insensitive to small variations in the profile and gives no information on the in-length characteristics, also no distinction is made between peaks and valleys [33].

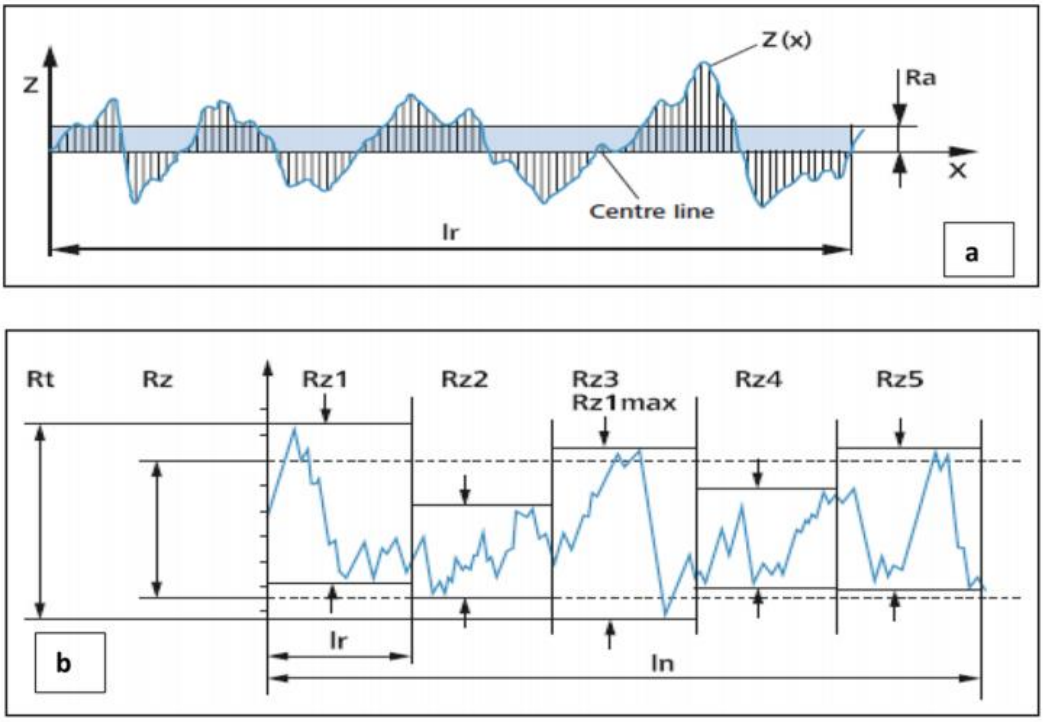


Figure 29 Criteria for defining the surface roughness: $R_a$, $R_z$ and $R_t$ according to ISO 4287 [34].

$R_t$ is defined as maximum peak to valley height over the evaluation length and very commonly used along with $R_a$, since it is very sensitive to large deviations from the mean line and scratches

[33] (Figure 29b). $R_z$ is average peak to valley height; it smoothens large deviations that are not representative of the surface finish compared to $R_t$. It is calculated by averaging the maximum peak to valley of five consecutive sampling lengths within the measuring length (Figure 29b). Feed rate and tool nose radius have the most significant influence on the $R_t$ and $R_a$ machined surface roughness parameters. Figure 30 shows schematic illustration of tool geometry on $R_t$ surface roughness in turning process.

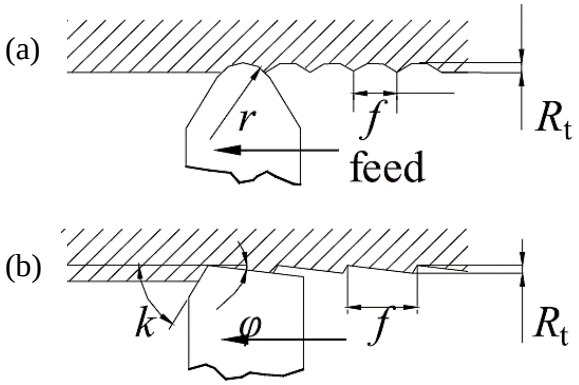


Figure 30 Schematic illustrations of tool geometry on surface roughness when turning with (a) tool with a nose radius, and (b) sharp-nosed tool [30].

Following equations have been developed to calculate the $R_t$ and $R_a$ values after turning process:

For a rounded tool nose with radius of $r$:

$$R_t = \frac{f}{\cot\kappa + \cot\varphi}\ [mm]. \tag{11}$$

For perfectly sharp tool:

$$R_t = f.\tan\varphi + \frac{r}{2}\tan^2\varphi - \sqrt{2.f.r.\tan^3\varphi}\ [mm]. \tag{12}$$

Where $r$ is tool nose radius, $f$ is feed rate, $\kappa$ and $\varphi$ are angles with regard to feed (Figure 30). Due to different cutting tool geometries involving in different machining processes, a wide

range of $R_a$ roughness values can be obtained in various machining methods. It is observable in Figure 31 that turning process produces a wide range of surface roughness values ranging from as low as 0.05 µm in finish turning to as high as 25 µm in roughing process.

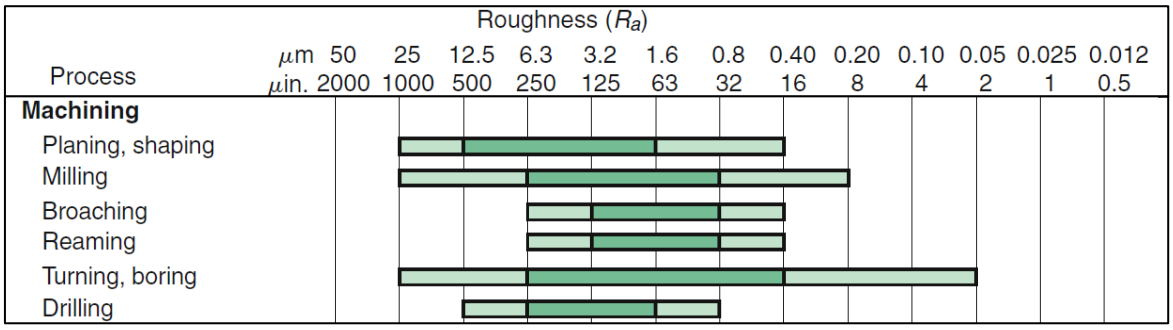

Figure 31 The range of surface roughness values obtained in various machining processes [11].

## 2.3. MACHINING OF SUPERALLOYS

Machining of components such as turning shafts and milling disks out of superalloys including Inconel 718 is partially influenced by their deformation behaviour particularly by shear localization in the adiabatic shear bands [35-38]. The poor heat dissipation during machining due to their low thermal conductivity [39-42] would lead to strain localization (hence adiabatic shear band formation) along with generation of high local temperatures at the cutting zone. One of the consequences of local temperature increase is the occurrence of high rates of dissolution wear on the rake face of the cutting tool [43] as Ni has high chemical affinity to carbides in the cutting tools [44-47]. Recently, high-pressure coolants [48, 49], cryogenic coolants [50, 51], use of tool coatings resistant to dissolution wear [52] and different cutting methods such as minimum quantity lubrication (MQL) [53] and different cutting tools [54] have been developed

to improve machinability of Ni based super alloys. Another relatively new strategy consists of modification of cutting fluids with small quantities of metallic or non-metallic nanoparticles.

Inconel 718 is a widely used nickel-based superalloy with high corrosion and creep resistance for elevated temperature applications. This provides challenges during machining due to retention of strength at elevated temperatures, high strain and strain-rate hardening, low thermal conductivity and presence of hard carbide particles in its microstructure [1]. As a result, generally tool wear [9, 41] and cutting forces are high and the machined surfaces has low quality [40, 55]. Various methods have been proposed to facilitate cutting process during machining of nickel-based superalloys including:

- High pressure cooling [48],
- Thermally enhanced machining [56],
- Laser assisted machining [57],
- Hybrid machining (application of two or more of the mentioned cutting conditions at the same time) [58],
- Use of suitable tool coatings [59].

Two other methods that have been recently employed so as to improve machinability of superalloys in particular Inconel 718 are application of cryogen ($CO_2$ or liquid nitrogen ($LN_2$)) to the cutting area [50, 60, 61], as well as use of nano-fluids in the cutting process [62].

Cryogenic cutting has been used for last 30 years in which a cryogen is used to change the mechanical properties of workpiece and tool material so as to facilitate metal cutting process. The next section will summarize the previous works that has been done in this field.

### 2.3.1. Improvement of Machining Performance of Inconel 718 Superalloy by Applying Graphene Nanoplatelet (GNP)

Different lubricants have been enhanced by adding nanoparticles at a specific ratio such as 0.15 wt.% Cu [63], 5 wt.% fullerene [64], 0.05 wt.%PbS [65], 1.0 wt. % $TiO_2$ [66], 0.1 wt.% ZnS [67], 1.0 wt.% $LaF_3$ [68], 1.0 wt.% Ni [69], 0.2 wt.% $SiO_2$ [70], 0.5 wt.% $MoS_2$ [71]. The results proved that cutting forces and the tool wear were reduced by the addition of nanoparticles to lubricant during the machining processes. Some studies attributed the observed reductions in cutting forces and tool wear to the formation of thin films or tribolayers on the contact surfaces of cutting tools [70-76]. It was also suggested that rolling of nano-particles at the interfaces between the tool and the workpiece would reduce cutting forces [77-80].

Further improvements in machining properties could be achieved using lubricants incorporating carbon based nanoparticles such as fullerene [77], and nano-diamond [75] due to their high thermal conductivity, which allows high rates of heat dissipation from the tool chip interface. Graphene emerges as a good candidate because it has excellent thermal conductivity, as high as 5000 $Wm^{-1}K^{-1}$ [81, 82] and also graphene nanoplatelets (GNPs) provide low coefficient of friction (COF) [83, 84].

Some researchers have conducted experiments on the role of graphene in machining of difficult to cut alloys. This section reviews previous works done on the effect of addition of nanoparticles in the cutting fluid during tribological and machining tests and summarizes its effect on coefficient of friction (COF), tool wear, cutting force, cutting temperature, surface quality and microhardness.

*2.3.1.1. Tribological tests*

Elomaa, et al. [78] conducted the tribological tests between a stainless steel ball and a tetrahedral amorphous carbon (ta-C) counterfaces using 1.0 wt.% graphene oxide (GO) blended water. A low COF of 0.06 was observed, which was due to the formation of a GO tribolayers on the counterfaces (Figure 32).

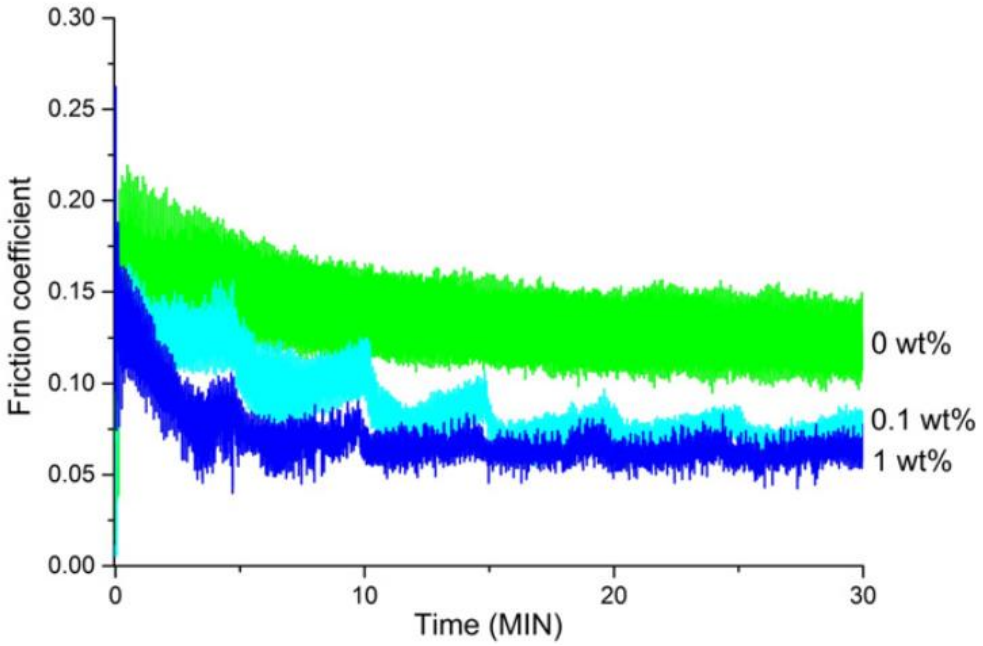


Figure 32 COF as a function of time in ta-C vs stainless steel contacts lubricated with pure water, water with 1 wt.% of GO and water with 0.1 wt.% of GO [78].

Figure 33 shows COF in a research conducted by Kinoshita, et al. [79] in which they found that GO sheets (1.0 wt.%) dispersed in water during sliding WC against stainless steel would produce a low COF of 0.05. The observed low COF was attributed to the formation of GO rich tribolayer on WC contact surface.

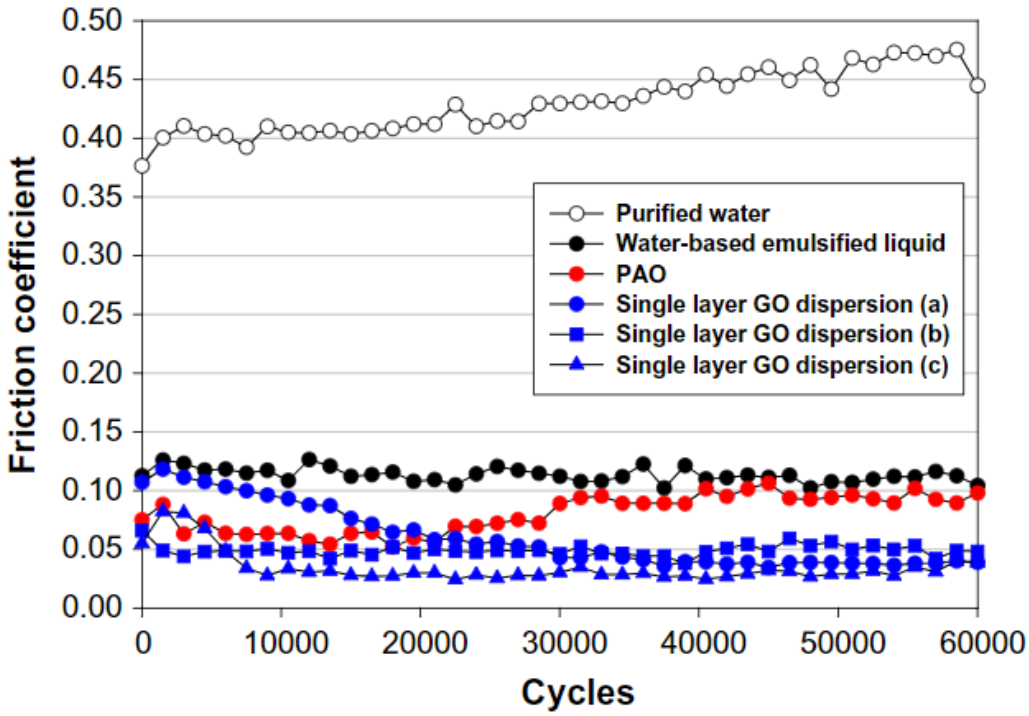


Figure 33 Variations of COF in sliding test under different lubrication conditions [79].

Bhowmick, et al. [85] studied the effect of GNPs (0.0005 wt.%) dispersed in absolute ethanol ($C_2H_5OH$) on the tribological behaviour of M2 steel sliding against itself under boundary-lubricated condition. As is shown in Figure 34, a low COF of 0.18 was observed, which was almost 50% lower than the COF of $C_2H_5OH$ without addition of GNPs. The reduction of COF was attributed to the generation of GNPs rich tribolayers on the counterface. It was found that the GNP layers were bent and fragmented during sliding.

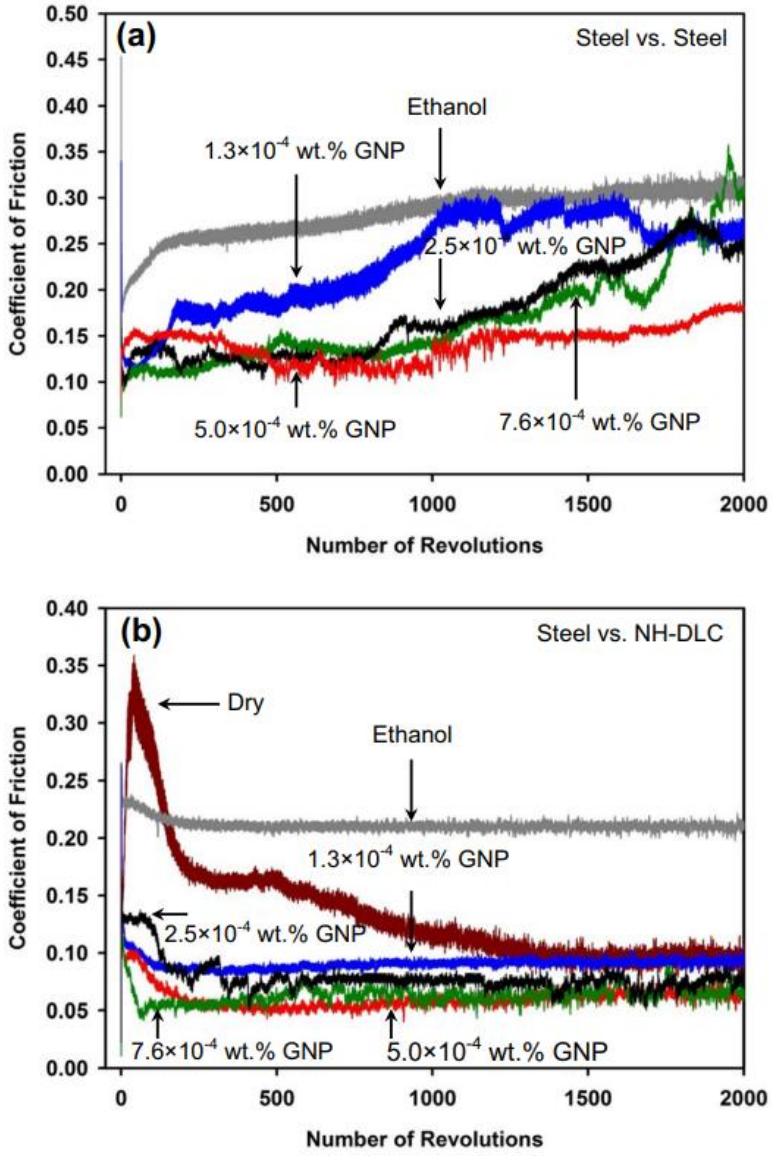


Figure 34 Variation of the COF with the number of revolutions for sliding tests conducted in different concentration of GNPs [85].

*2.3.1.2. Tool wear*

Park, et al. [73] used exfoliated graphite nanoplatelets (0.1 wt.%) dispersed in a cutting fluid during milling of AISI 1045 steel and found that GNP-dispersed vegetable oil reduced the wear and chipping at the cutting edge of the tool compared to flooded milling (Figure 35).

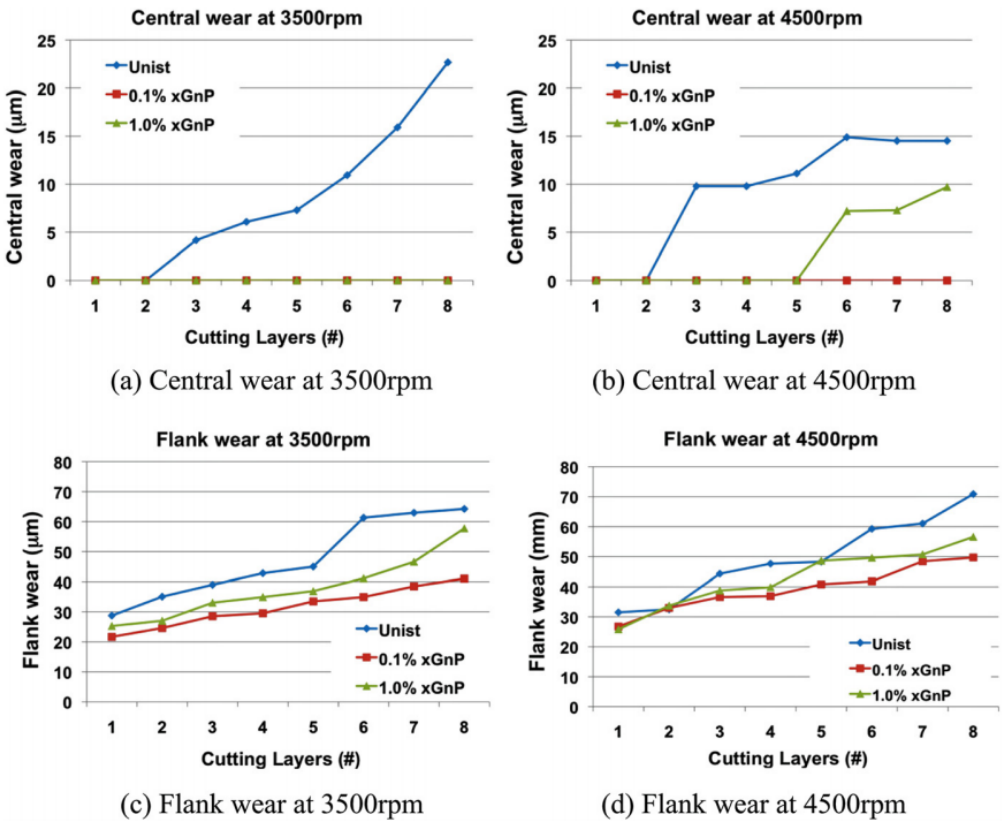


(a) Central wear at 3500rpm (b) Central wear at 4500rpm

(c) Flank wear at 3500rpm (d) Flank wear at 4500rpm

Figure 35 Central and flank wear in terms of concentration of GNP in CF [73].

Singh, et al. [74] reported that use of cutting fluid blended with 1.0 wt.% graphene during turning of AISI 4340 hardened steel resulted in the lowest tool flank wear compared with pure oil (CF) and dry cutting conditions. SEM images of flank wear under these cutting conditions at speed of 170 m/min after 6 min is illustrated in Figure 36.

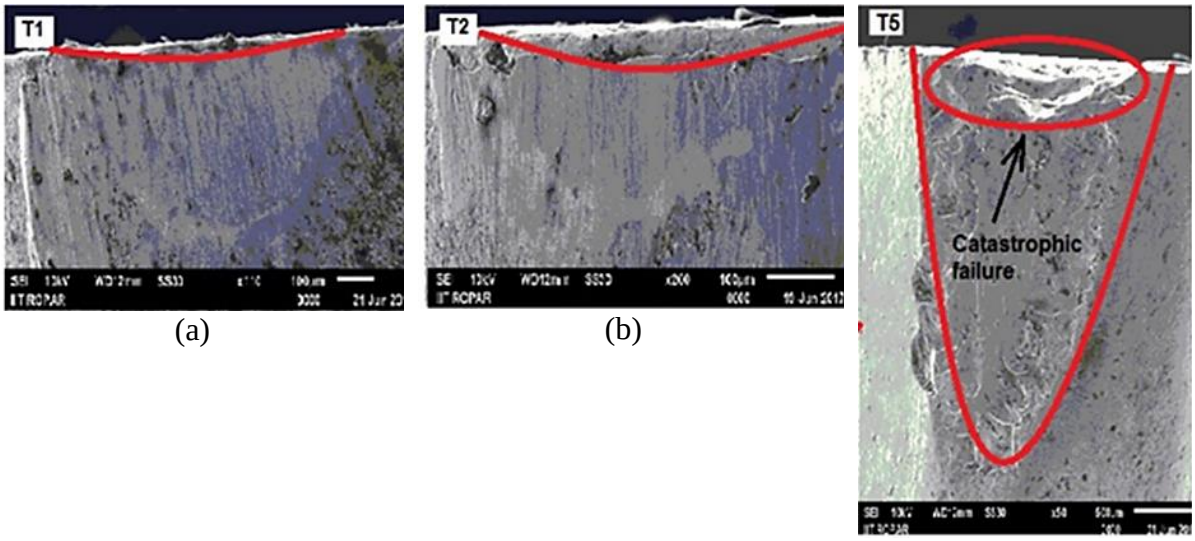


(a) (b) (c)

Figure 36 SEM images of flank wear under (a) CF blended with 1.0 wt.% graphene, (b) CF, (c) dry cutting conditions at speed of 170 m/min after 6 min [74].

Li, et al. [72] reported that after milling of TC4 titanium alloy, the tool encountered less flank wear when graphene was blended with MQL method in comparison to pure MQL (without using graphene) and when gas was used as the coolant (Figure 37). SEM images of tool flank wear under these cutting conditions is shown in Figure 38. It was observed that cutting titanium alloy using graphene in the MQL method resulted in the lowest tool edge defects compared to other cutting conditions.

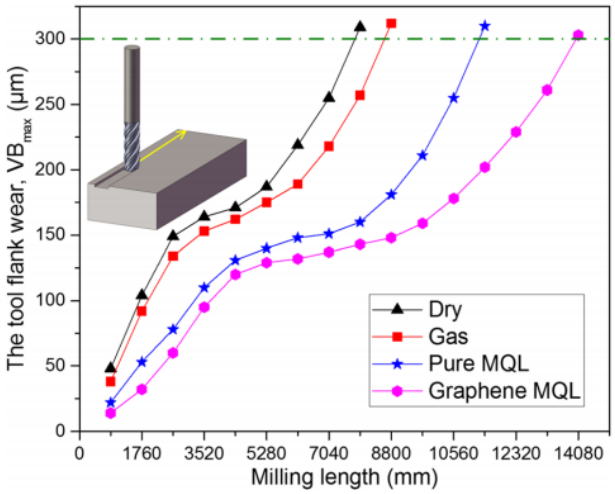


Figure 37 The tool life curves under different lubrication conditions [72].

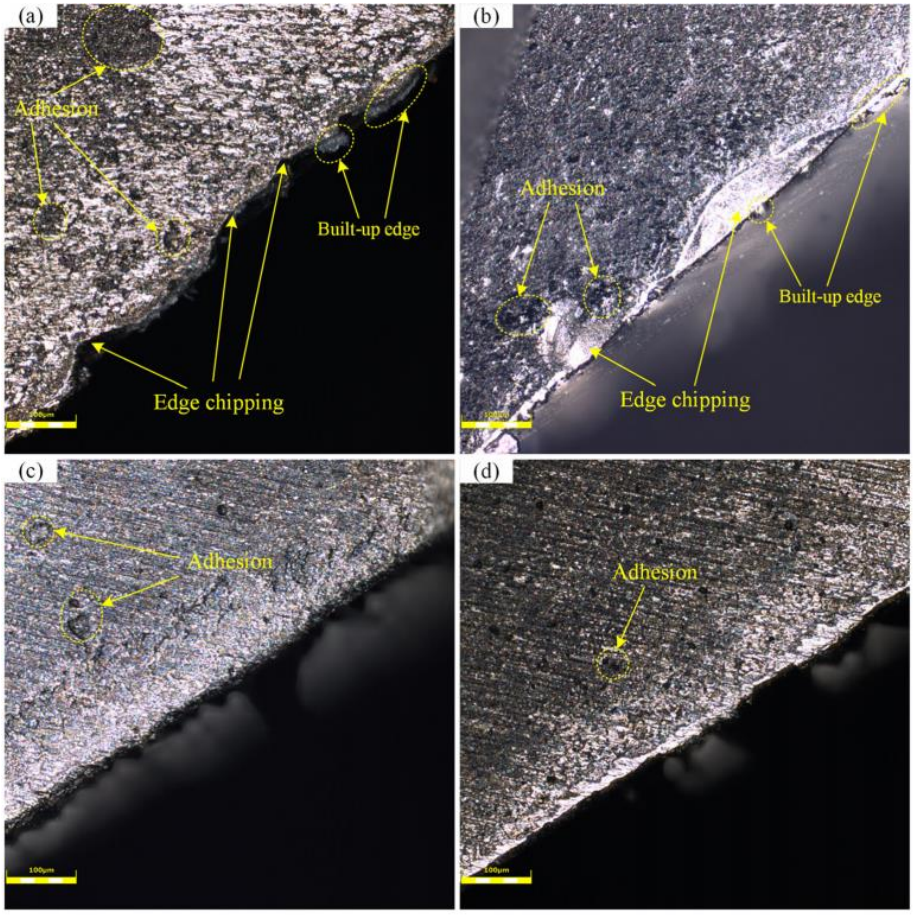


Figure 38 SEM images of tool flank wear under (a) dry, (b) gas, (c) pure MQL, and (d) graphene MQL, cutting conditions [72].

*2.3.1.3. Cutting force*

Singh, et al. [74] observed that the application of GNP (0.5-1.5 wt.%) mixed with vegetable oil during turning of AISI 4340 hardened steel using minimum quantity lubrication (MQL) reduced cutting forces and temperatures nearly 40% and 60% compared to the dry turning (Figure 39).

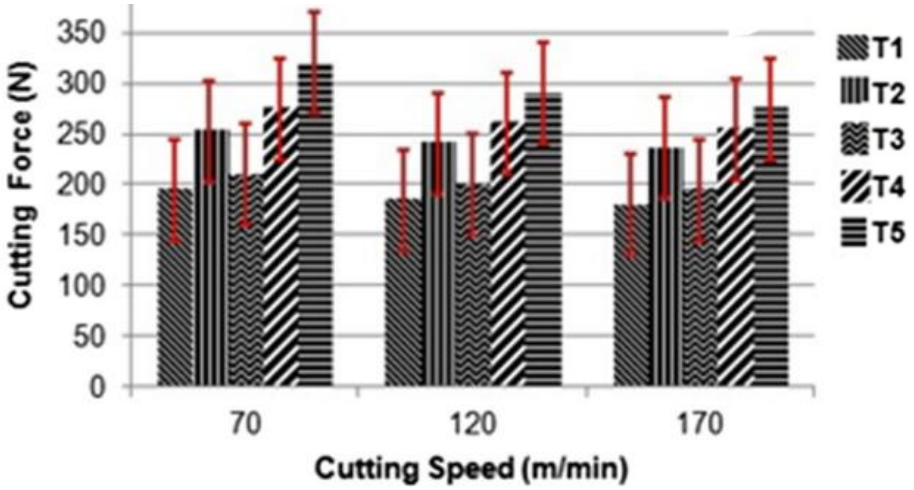


Figure 39 Average value of cutting forces under different environments [74].

Pavan, et al. [86] showed that addition of 0.3 wt.% of graphene to the cutting fluid when using MQL method (MQL CF8 in Figure 40) resulted in the lowest normal and tangential forces in grinding of Inconel 718. Dry grinding and pure cutting fluid without GNP produced the highest forces.

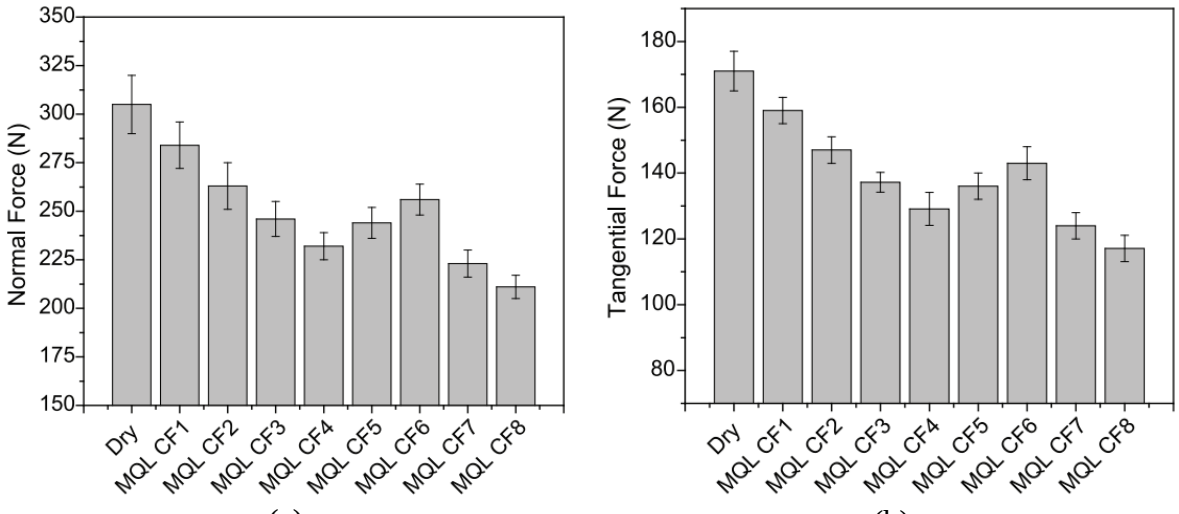


Figure 40 Effect of GNP-based nanofluid on (a) normal, (b) tangential grinding force [86] (CF1= 0 wt.%, CF2= 0.1 wt.%, CF3= 0.2 wt.%, CF4= 0.3 wt.%, CF5= 0.4 wt.%, CF6= 0.5 wt.%, CF7= 0.3 wt.% (grade II), CF8= 0.3 wt.% (grade III) [86].

*2.3.1.4. Cutting temperature*

Li, et al. [72] examined the roles of GNPs (0.1 wt.%) added to the cutting fluids during milling of titanium alloys and reported that the cutting temperature during milling was reduced by 30% compared to dry milling and 35% reduction in tool wear was observed (Figure 41).

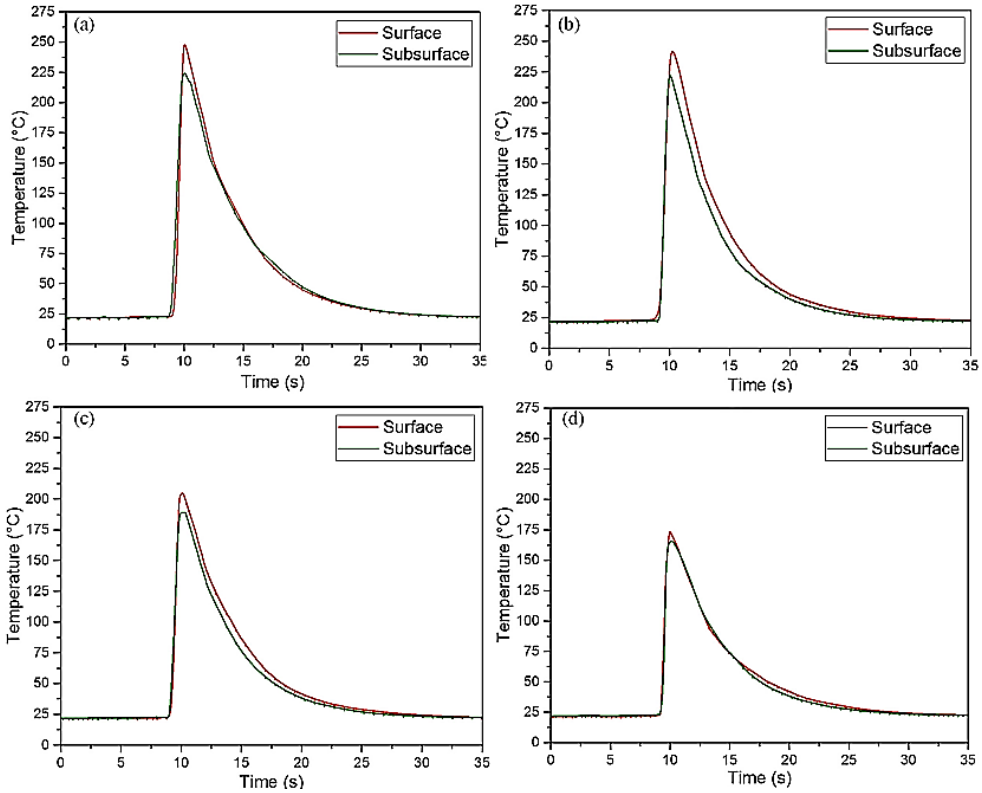


Figure 41 The measured typical signal profiles of surface temperature and the subsurface temperature under (a) dry, (b) gas, (c) pure, and (d) graphene MQL [72].

According to the study conducted by Pavan, et al. [86], grinding Inconel 718 using 0.3 wt.% graphene in the cutting fluid accounted for the lowest cutting temperature of 200 °C, while when the process was carried out using cutting fluid without GNP resulted in temperature of 230 °C (Figure 42).

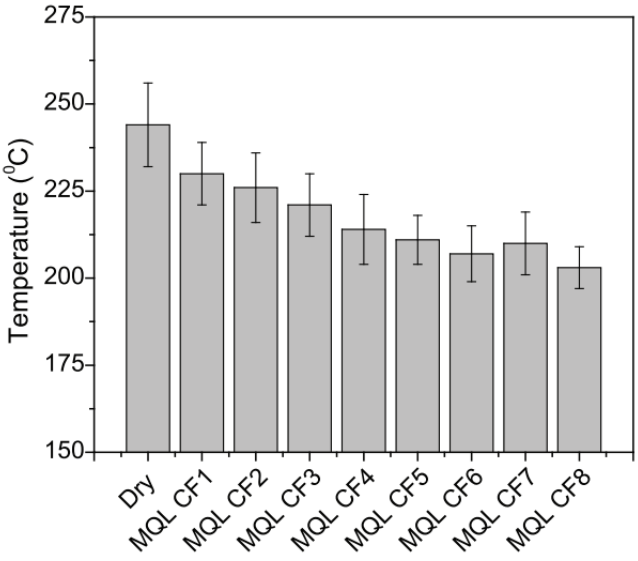


Figure 42 Effect of GNP-based nanofluid on grinding temperature [86] (CF1= 0 wt.%, CF2= 0.1 wt.%, CF3= 0.2 wt.%, CF4= 0.3 wt.%, CF5= 0.4 wt.%, CF6= 0.5 wt.%, CF7= 0.3 wt.% (grade II), CF8= 0.3 wt.% (grade III) [86].

*2.3.1.5. Surface quality*

Pavan, et al. [86] investigated the role of GNPs (0-0.5 wt.%) during grinding of Inconel 718 in MQL condition. The GNPs reduced the surface roughness of the Inconel 718 than the dry and MQL grinding conditions (Figure 43).

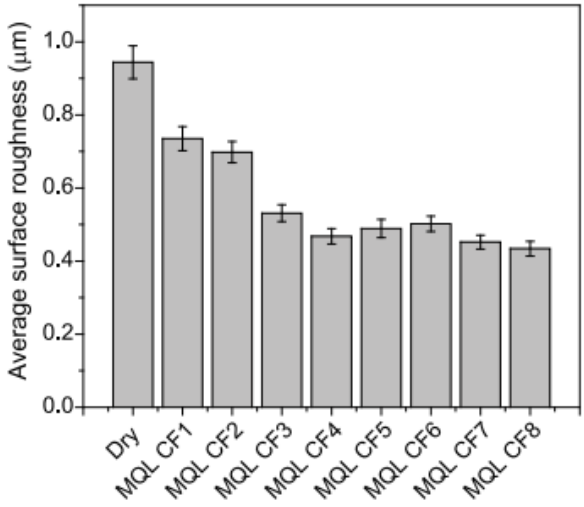


Figure 43 Effect of GNP-based nano-fluid on normal grinding force [86], (CF1= 0 wt.%, CF2= 0.1 wt.%, CF3= 0.2 wt.%, CF4= 0.3 wt.%, CF5= 0.4 wt.%, CF6= 0.5 wt.%, CF7= 0.3 wt.% (grade II), CF8= 0.3 wt.% (grade III) [86].

Figure 44 shows surface quality after milling of TC4 titanium conducted by Li, et al. [72] under dry condition as well as using gas, cutting fluid without GNP and MQL containing GNP. As it is evident in this figure, the machined surface using the latter one, i.e. using MQL blended with GNP was smoother compared to other methods. They also examined the effect of addition of GNP to the cutting fluid on surface and subsurface hardened depth (Figure 45a, b) and compared them with other cutting conditions. The results revealed that addition of GNP in MQL reduced the obtained surface microhardness to (350 HV) and hardened layer depth under the surface after machining to (5 µm) compared to MQL without GNP (375 HV and 10 µm).

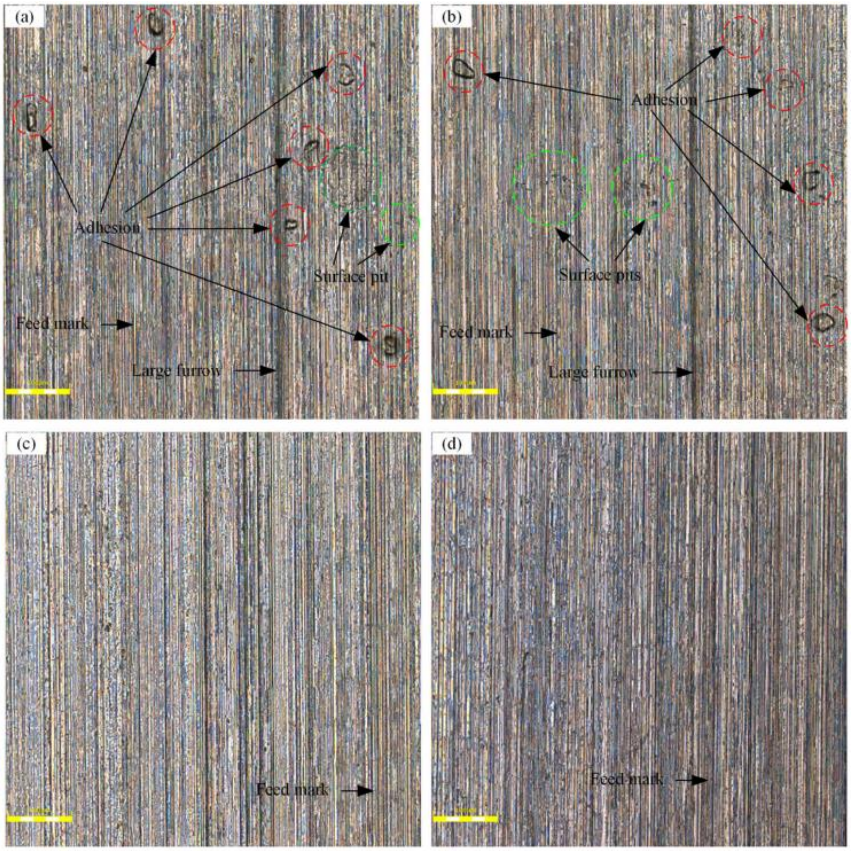


Figure 44 Machined surface quality obtained during the machining under (a) dry, (b) gas, (c) pure, and (d) graphene MQL [72].

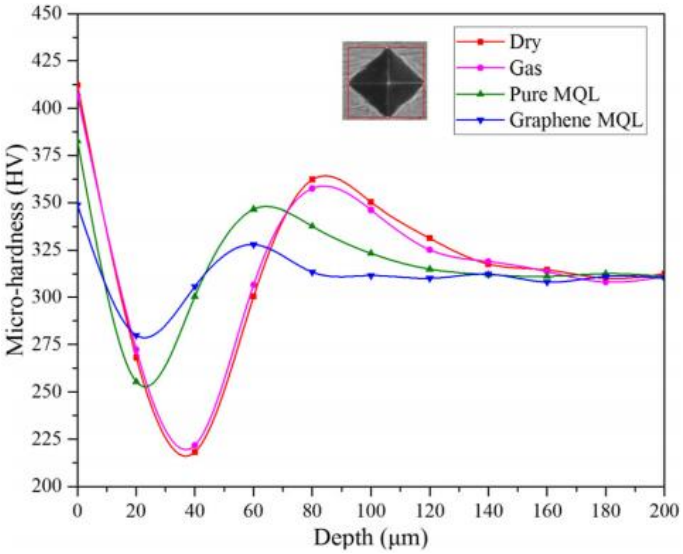


(a)

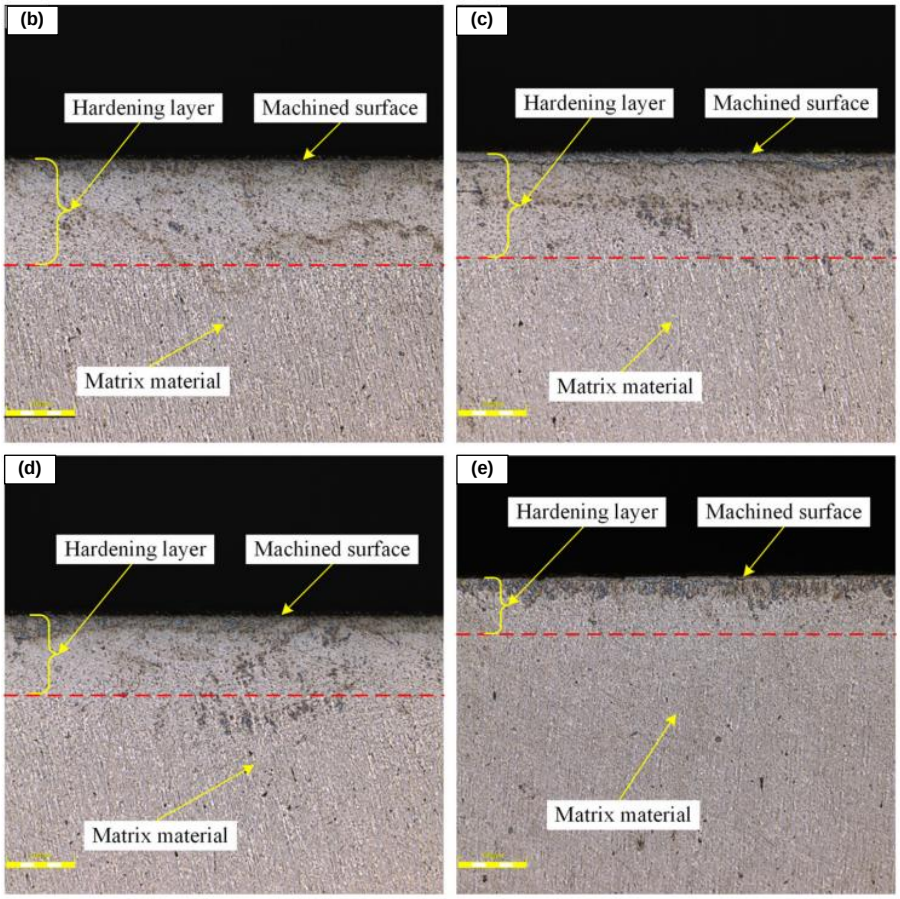


Figure 45 (a) The surface and subsurface microhardness values [72]. Depth of subsurface hardened layer under (b) dry, (c) gas, (d) pure, and (e) graphene MQL [72].

Similar results were reported by Pavan, et al. [86] in grinding of Inconel 718 using different concentration of GNPs in the cutting fluids. As Figure 46 shows, 0.3 wt.% in MQL resulted in a defect free surface while on the surfaces produced by other methods there large ridges.

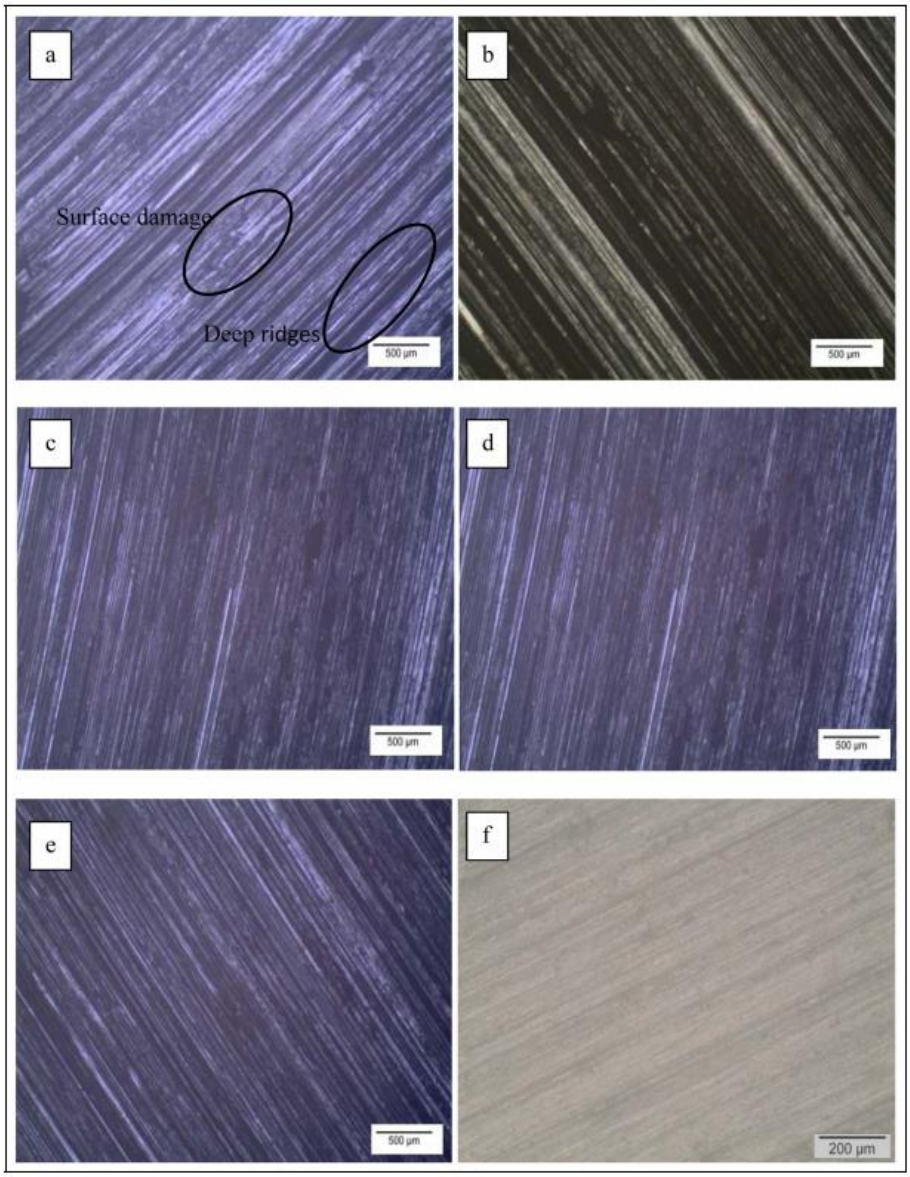


Figure 46 Workpiece surface quality after (a) dry grinding, MQL grinding with (b) 0, (c) 0.2, (d) 0.3 (grade I), (e) 0.4, and (f) 0.3 wt.% (grade III) [86].

### 2.3.2. Improvement of Machining Performance of Inconel 718 Superalloy by Applying $LN_2$

Cryogenic cutting is considered as a clean production method since liquid nitrogen ($LN_2$) evaporates instantly, leaving the machined workpiece dry and free of metal cutting fluid films and contaminants. Although the cost of $LN_2$ could be higher than flooded cutting, it has the advantage of eliminating post-cutting cleaning and recycling process. Operating the machining process using cryogens would increase the rate of heat dissipation and alleviate some of the issues related to high temperature generation the tool-workpiece interface. Mechanical properties of the workpiece material especially for steel and other the body centered cubic (bcc) and some hexagonal close packed, hcp, like titanium alloys are sensitive to low temperatures and may lead to improved machinability. Machining practices in which cryogens were applied to the cutting area dates back to 1919 [87]. Some researchers have applied the cryogen on the workpiece material by immersing the material into the cryogen [17] while other researchers have sprayed it onto the cutting area [88, 89] or the combination of these techniques [50]. Cryogenic cooling during the machining process has several effects on machining performance including (1) changing the mechanical properties of the workpiece and tool materials (increase in hardness, modulus of elasticity and strength of materials). (2) removing the heat generated during the machining process and (3) change in frictional characteristics of the tool-chip and tool-workpiece interfaces [90, 91].

The literature survey presented in the following parts of this section therefore summarizes the previous experimental works on cryogenic machining of nickel-based superalloys. Cryogenic cooling method during the turning of Inconel 718 has been compared with flooded and other cooling/lubrication methods. The following sections will review the previous works according

to the response parameters, i.e. tool wear, cutting force, surface roughness, subsurface deformation and chip morphology.

*2.3.2.1. Tool wear*

Kaynak [60] investigated the tool wear during the turning process of Inconel 718 under cryogenic, minimum quantity lubrication (MQL) and dry cutting conditions at different speeds (30, 60, 90 and 120 m/min). It was reported that the cutting tool contact length between chip and tool rake face in cryogenic cooling conditions was approximately 24% larger (1.69 mm) than that in MQL conditions (1.36 mm) at the speed of 60 m/min (Figure 47a). At higher cutting speed (120 m/min), contact length was smaller than those measured in dry and almost same with MQL conditions (Figure 47b). Evaluation of flank wear showed that cryogenic cooling resulted in lower flank wear (218 μm) compared with MQL (340 μm) and dry conditions (939 μm) (Figure 47c). Wear mechanism analyses showed that the abrasive wear mechanism was predominant during the cryogenic cutting process (Figure 48).

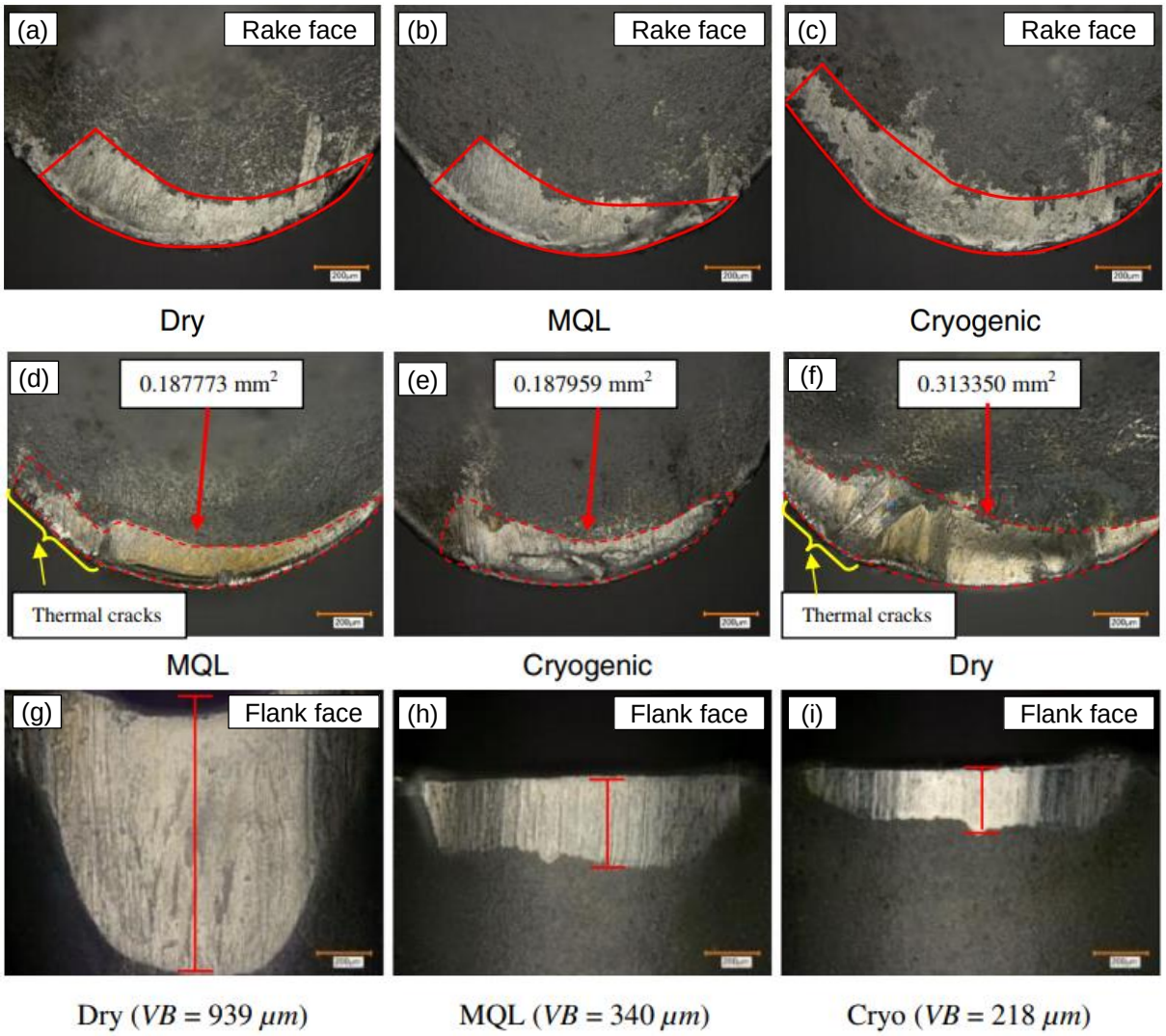


Figure 47 Crater wear as a function of different cooling/lubricating at the cutting speed of (a-c) 60 m/min, (d-f) 120 m/min. (g-i) Flank wear under different cutting conditions at 120 m/min [60].

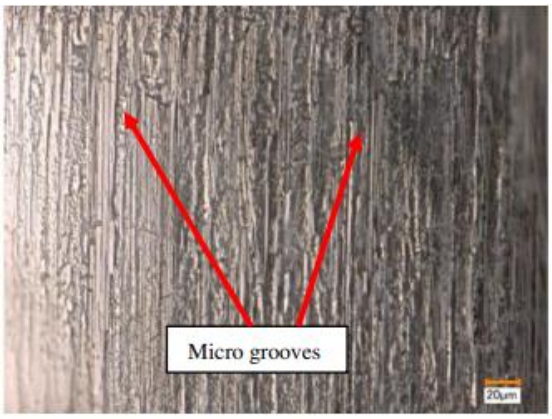


Figure 48 Wear mechanism under cryogenic cutting condition [60].

Iturbe, et al. [92] compared flank wear variation in cryogenic turning of Inconel 718 with conventional flooded cooling which was conducted in a previous work by Kaynak [60]. They reported that flooded cooling outperforms the cryogenic machining in terms of tool life. As is shown in Figure 49, cutting time was 20 min in flooded cutting while it was almost 7 min during the cryogenic cutting.

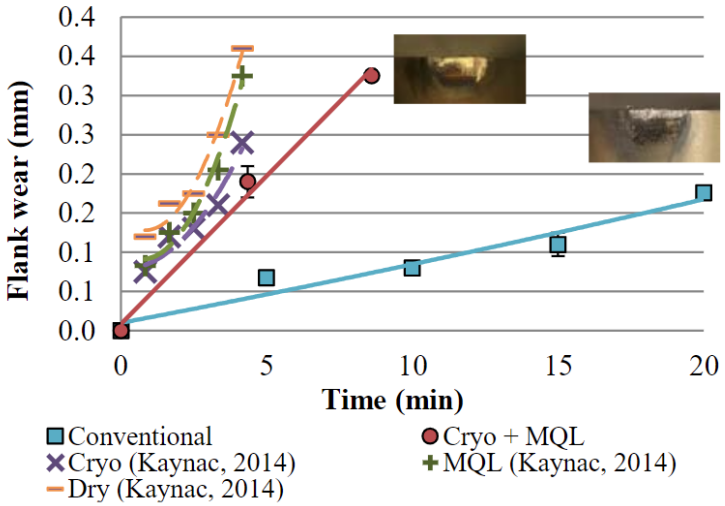


Figure 49 Evolution of flank wear in turning of Inconel 718 under cryogenic, MQL which were done by Kaynak [60] in comparison to flooded and dry conditions [92].

Pusavec, et al. [93] conducted the turning process on Inconel 718 under different cutting conditions namely dry, MQL, cryogenic and combination of cryogenic and MQL (cryoMQL). Figure 50a, b summarizes the results of the tool wear analyses, showing variation of flank wear ($VB_{max}$) and rake wear ($KV_{max}$) with cutting parameters. Dry cutting, generally, resulted in more flank wear compared to cryogenic and MQL methods. CryoMQL method showed the lowest flank and rake wear at different cutting conditions.

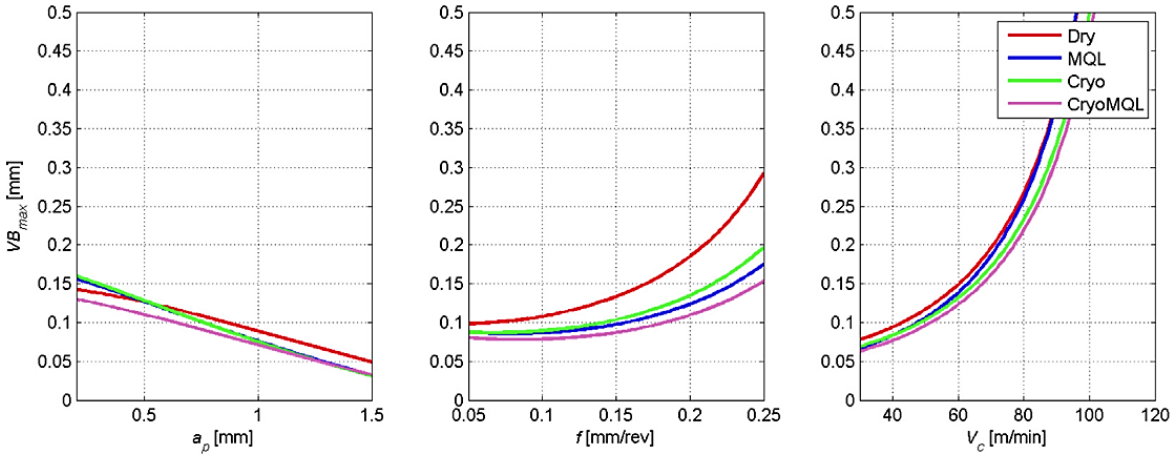


(a)

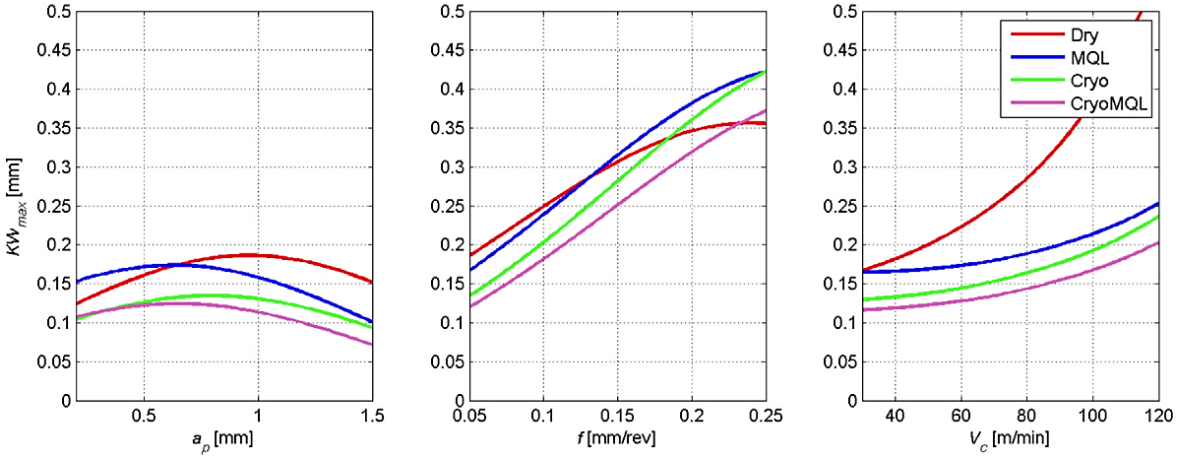


(b)

Figure 50 The influence of the cutting parameters on the cutting tool (a) flank wear and (b) rake wear under different cooling/lubrication conditions [93]. $a_p$=depth of cut, $f$= feed rate, $V_c$= cutting speed.

*2.3.2.2. Cutting force*

Kaynak [60] reported that cryogenic cutting of Inconel 718 resulted in higher radial, feed and radial cutting forces in comparison with MQL machining at low cutting speed of 60 m/min. However, at the higher cutting speed of 120 m/min, all the cutting force components were lower than the one under dry and MQL conditions (Figure 51).

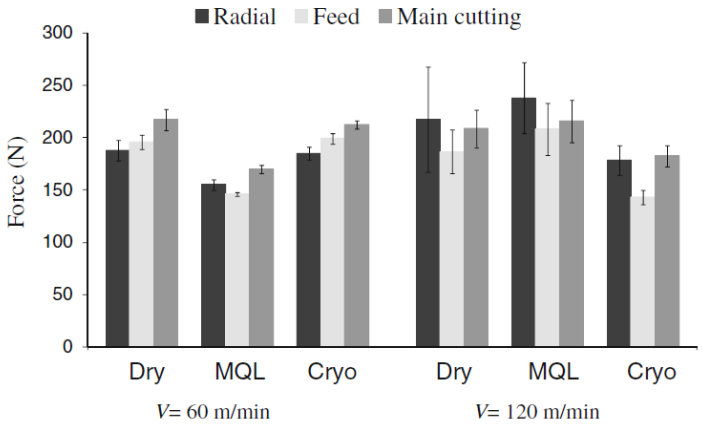


Figure 51 Comparison of cutting force components under dry, MQL and Cryogenic conditions [60].

Tebaldo, et al. [94] studied effect of Minimum Quantity Cooling (MQC) in cutting of Inconel 718. In MQC emulsions (made of soluble oil in water), water, or air (cold or liquid air) are utilized and compared the results from those of cut under dry, MQL and conventional wet machining. As is shown in Figure 52, cutting force under dry resulted in the lowest values, followed by MQL and MQC. Wet cutting led to high values of cutting forces compared to other conditions.

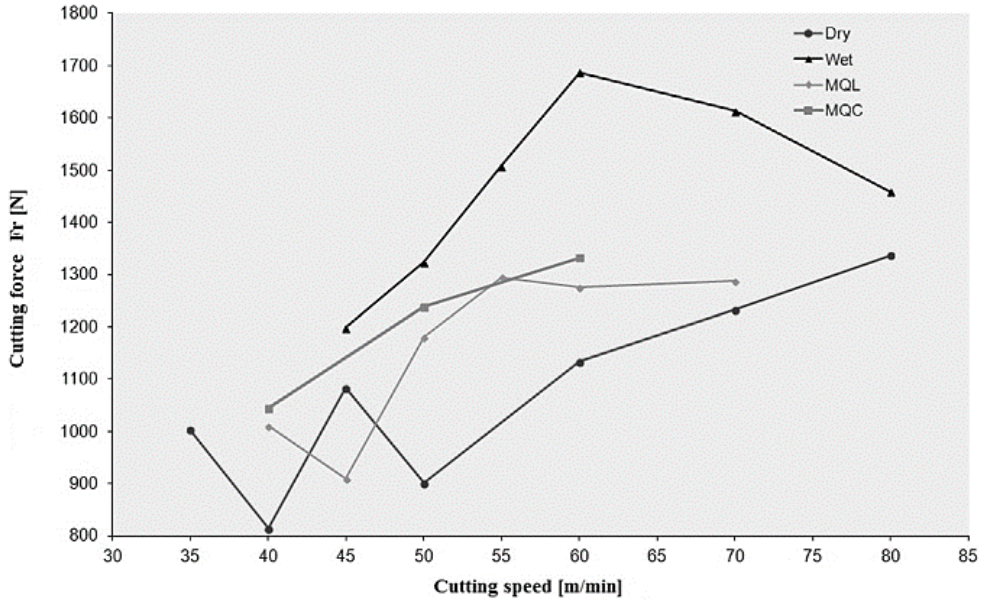


Figure 52 Cutting force values as a function of cutting speed under different cutting conditions [94].

Pusavec, et al. [93] compared the effect of application of cryoMQL (MQL+cryogenic) method with MQL and cryogenic conditions in machining of Inconel 718 which is shown in Figure 53. Cryogenic resulted in higher cutting forces at high feed rates while cryoMQL showed the lowest one at all the feed rates. At different cutting speeds and depth of cuts, cutting force did not show high difference between different cutting conditions.

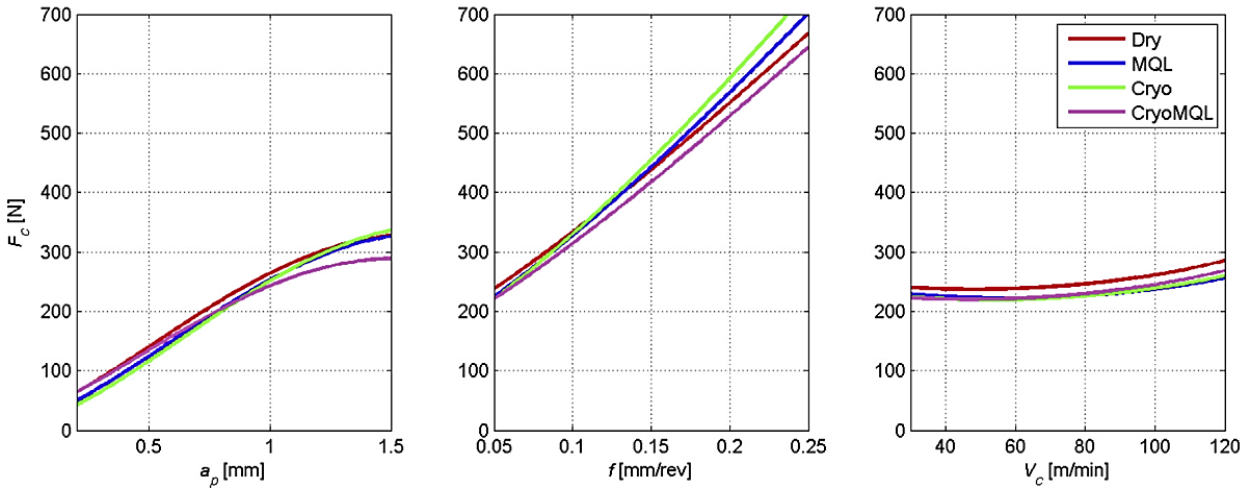


Figure 53 The influence of the cutting process parameters on the cutting force ($F_c$) under different cutting conditions [93].

*2.3.2.3. Surface roughness*

Pusavec, et al. [93] reported that with increasing the cutting parameters under all the cutting conditions, the surface roughness increased, especially with increasing the feed rate. In all plotted cases, cryo-lubrication provides lower $R_a$ roughness values than the other conditions. However, at higher feeds, the cryo-lubrication condition not only did not help at all, but it made it even worse (Figure 54).

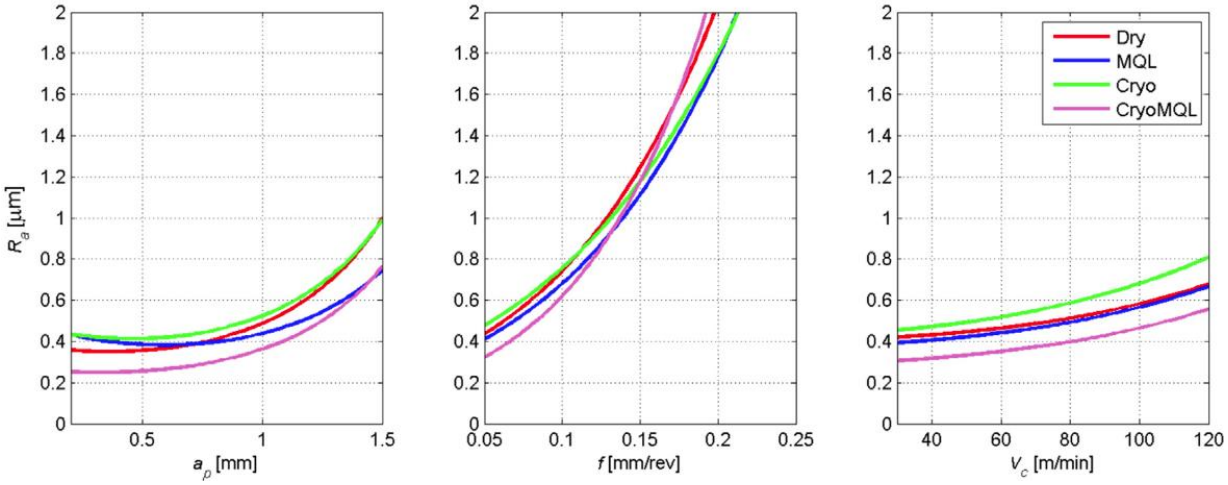


Figure 54 The influence of the cutting parameters on the machined surface roughness ($R_a$) under different cutting conditions [93].

*2.3.2.4. Subsurface microstructure*

Iturbe, et al. [92] showed that conventional flooding method performed better than cryogenic+MQL method in terms of subsurface microstructural damage. Figure 55 shows the surface damage induced with the cryogenic + MQL technique is four times bigger than that the one obtained by the conventional flooding one.

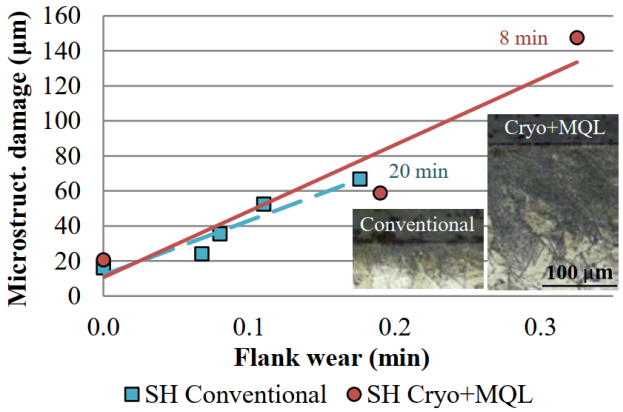


Figure 55 Microstructural damage vs. tool flank wear when turning Inconel 718 with cryogenic+ MQL and conventional cooling/lubricating approaches [92].

*2.3.2.5. Chip morphology*

Kaynak [60] investigated turning of Inconel 718 under cryogenic, MQL and dry conditions. The results showed that in all three conditions, segmented chips were generated. The pitch generated under cryogenic cooling was approximately three times larger and the valley was smaller than the one in dry and MQL conditions (Figure 56). They also reported that chip thickness increased 30% compared to MQL conditions in cryogenic cooling, while dry cutting generated the smallest chip thickness.

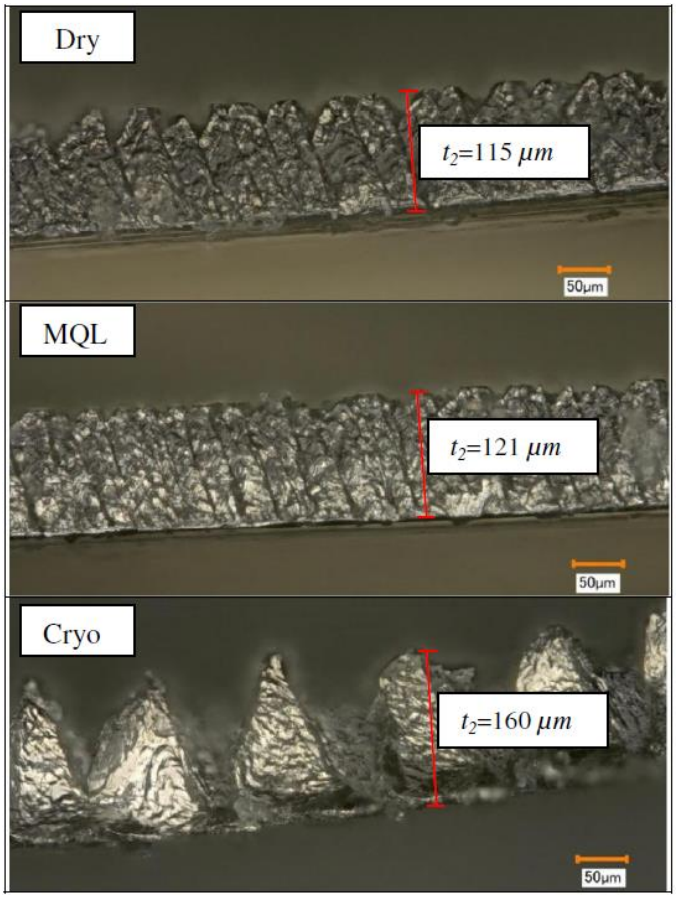


Figure 56 Chip morphology as a function of cutting condition in machining of Inconel 718 [60].

### 2.3.3. Summary of literature survey and research gaps

The literature survey revealed that the use of GNP-incorporated vegetable-based cutting fluid and a stream of liquid nitrogen during the cutting of Inconel 718 superalloy are effective approaches towards replacing mineral-based oils with eco-friendly alternatives (such as vegetable-based cutting fluids) while maintaining machinability of Inconel 718 superalloy.

However, tribological behaviour of Inconel 718 against WC-Co was not thoroughly investigated in machining of this alloy. Therefore, the underlying mechanism of improvement of machining performance when GNP-blended cutting fluid was used in cutting of Inconel 718

has not been thoroughly determined. Chapter 3 of this study addresses this gap by conducting sliding tests between Inconel 718 and WC-Co counterfaces as well as drilling experiments on Inconel 718 using WC-Co cutting tools in order to establish a relationship between the reduction of coefficient of friction by formation of tribolayers in sliding tests and the decrease in cutting torque and temperature during the cutting process. In addition, the effect of using GNP-blended cutting fluid on the subsurface microstructural deformation is studied in this section.

It was evident from the previous works that cryogenic machining did not always facilitate the cutting process of Inconel 718. There were many occasions that conventional flooded cutting outperformed cryogenic cutting method. For this reason, this method has not been implemented in machining industries as a viable practice. The question that which set of parameters should be used during the cryogenic machining to obtain an overall favorable performance which is comparable or even better the conventional flooded cutting is yet to be answered. Chapter 4 of this thesis implements response surface methodology (RSM) in order to determine the optimum parameters in which cryogenic cutting performs as effective as conventional flooded cutting while maintaining the clean production approach in turning of Inconel 718 alloy.

## REFERENCES

[1] M.J. Donachie, S.J. Donachie, Superalloys: a technical guide, ASM international, OH, USA, 2002.

[2] H. Long, S. Mao, Y. Liu, Z. Zhang, X. Han, Microstructural and compositional design of Ni-based single crystalline superalloys — A review, Journal of Alloys and Compounds, 743 (2018) 203-220.

[3] R.C. Reed, The superalloys: fundamentals and applications, Cambridge university press, United Kingdom 2008.

[4] Y. Wang, W.Z. Shao, L. Zhen, L. Yang, X.M. Zhang, Flow behavior and microstructures of superalloy 718 during high temperature deformation, Materials Science and Engineering: A, 497 (2008) 479-486.

[5] E. Cadel, D. Lemarchand, S. Chambreland, D. Blavette, Atom probe tomography investigation of the microstructure of superalloys N18, Acta Materialia, 50 (2002) 957-966.

[6] D.R. Jones, M.F. Ashby, Engineering materials 2: an introduction to microstructures and processing, Butterworth-Heinemann, USA, 2012.

[7] M.J. Donachie, Titanium: a technical guide, ASM international, USA, 2000.

[8] B. Davoodi, B. Eskandari, Investigation of wear mechanisms and tool life in turning of N-155 iron-nickel-base superalloy using response surface methodology, Modares Mechanical Engineering, 14 (2015) 51-58.

[9] D. Zhu, X. Zhang, H. Ding, Tool wear characteristics in machining of nickel-based superalloys, International Journal of Machine Tools and Manufacture, 64 (2013) 60-77.

[10] R. M'Saoubi, D. Axinte, S.L. Soo, C. Nobel, H. Attia, G. Kappmeyer, S. Engin, W.-M. Sim, High performance cutting of advanced aerospace alloys and composite materials, CIRP Annals, 64 (2015) 557-580.

[11] S. Kalpakjian, S. Schmid, Manufacturing Engineering and Technology, SI Edition, Singapore: Pearson Publications, 2013.

[12] Basic Definitions and Cutting Tool Geometry, Single Point Cutting Tools, in: V.P. Astakhov (Ed.) Geometry of Single-point Turning Tools and Drills: Fundamentals and Practical Applications, Springer London, London, 2010, pp. 55-126.

[13] A. Raczy, W. Altenhof, A. Alpas, An Eulerian finite element model of the metal cutting process, Proceedings of the 8th International LS-DYNA Users Conference, Dearborn, MI, USA, 2004, pp. 11-26.

[14] A. Moufki, A. Devillez, D. Dudzinski, A. Molinari, Thermomechanical modelling of oblique cutting and experimental validation, International Journal of Machine Tools and Manufacture, 44 (2004) 971-989.

[15] A. Raczy, M. Elmadagli, W. Altenhof, A. Alpas, An Eulerian finite-element model for determination of deformation state of a copper subjected to orthogonal cutting, Metallurgical and materials transactions a, 35 (2004) 2393-2400.

[16] L. Li, N. Yu, C. Chan, W. Lee, Al6061 surface roughness and optical reflectance when machined by single point diamond turning at a low feed rate, Plos one, 13 (2018) e0195083.

[17] G. Krishnamurthy, S. Bhowmick, W. Altenhof, A.T. Alpas, Increasing efficiency of Ti-alloy machining by cryogenic cooling and using ethanol in MRF, CIRP Journal of Manufacturing Science and Technology, 18 (2017) 159-172.

[18] M.C. Shaw, J. Cookson, Metal cutting principles, Oxford university press New York, 2005.

[19] N. Zorev, International research in production engineering, American Society of Mechanical Engineers, Pittsburgh, PA, (1963) 42.

[20] N. Zorev, Inter-relationship between shear processes occurring along tool face and shear plane in metal cutting, International research in production engineering, 49 (1963) 143-152.

[21] A. Bagchi, P. Wright, Stress analysis in machining with the use of sapphire tools, Proceedings of the Royal Society of London. A. Mathematical and Physical Sciences, 409 (1987) 99-113.

[22] E.M. Trent, P.K. Wright, Metal cutting, Butterworth-Heinemann, USA, 2000.

[23] E. Amini, Photoelastic analysis of stresses and forces in steady cutting, Journal of Strain Analysis, 3 (1968) 206-213.

[24] E. Doyle, J. Horne, D. Tabor, Frictional interactions between chip and rake face in continuous chip formation, Proceedings of the Royal Society of London. A. Mathematical and Physical Sciences, 366 (1979) 173-183.

[25] S. Akarca, W. Altenhof, A. Alpas, A Smoothed-Particle Hydrodynamics (SPH) Model for Machining of 1100 Aluminum, 10th Internatio nal LS-DYNA Conference, Detroit, 2008, pp. 12-11.

[26] H. Ni, M. Elmadagli, A.T. Alpas, Mechanical properties and microstructures of 1100 aluminum subjected to dry machining, Materials Science and Engineering: A, 385 (2004) 267-278.

[27] M. Fahad, A heat partition investigation of multilayer coated carbide tools for high speed machining through experimental studies and finite element modelling, The University of Manchester (United Kingdom), 2012.

[28] W.H. Yang, Y.S. Tarng, Design optimization of cutting parameters for turning operations based on the Taguchi method, Journal of Materials Processing Technology, 84 (1998) 122-129.

[29] M.C. Shaw, Self friability of falling objects, Bulletin of JSME, 23 (1980) 324-328.

[30] D.A. Stephenson, J.S. Agapiou, Metal cutting theory and practice, CRC press, USA, 2016.

[31] International Standard ISO 3685, Tool-life testing with single-point turning tools, 1993-11-15.

[32] D. Whitehouse, 2 - Identification and separation of surface features, in: D. Whitehouse (Ed.) Surfaces and Their Measurement, Kogan Page Science, Oxford, 2002, pp. 16-47.

[33] J.P. Davim, Surface integrity in machining, Springer, London 2010.

[34] M. Hamed, Y. Zedan, A.M. Samuel, H.W. Doty, F.H. Samuel, Milling parameters of Al-Cu and Al-Si cast alloys, The International Journal of Advanced Manufacturing Technology, 104 (2019) 3731-3743.

[35] R. Komanduri, T.A. Schroeder, On shear instability in machining a nickel-iron base superalloy, Journal of Engineering for Industry, 108 (1986) 93-100.

[36] A.R.C. Sharman, A. Amarasinghe, K. Ridgway, Tool life and surface integrity aspects when drilling and hole making in Inconel 718, Journal of Materials Processing Technology, 200 (2008) 424-432.

[37] J. Ning, V. Nguyen, Y. Huang, K.T. Hartwig, S.Y. Liang, Inverse determination of Johnson–Cook model constants of ultra-fine-grained titanium based on chip formation model and iterative gradient search, The International Journal of Advanced Manufacturing Technology, 99 (2018) 1131-1140.

[38] A. Gok, C. Gologlu, H.I. Demirci, Cutting parameter and tool path style effects on cutting force and tool deflection in machining of convex and concave inclined surfaces, The International Journal of Advanced Manufacturing Technology, 69 (2013) 1063-1078.

[39] I.A. Choudhury, M.A. El-Baradie, Machinability of nickel-base super alloys: a general review, Journal of Materials Processing Technology, 77 (1998) 278-284.

[40] B. Davoodi, B. Eskandari, Evaluation of surface damage mechanisms and optimisation of cutting parameters in turning of N-155 iron-nickel-base superalloy, International Journal of Machining and Machinability of Materials, 21 (2019) 100-114.

[41] B. Eskandari, B. Davoodi, H. Ghorbani, Multi-objective optimization of parameters in turning of N-155 iron-nickel-base superalloy using gray relational analysis, Journal of the Brazilian Society of Mechanical Sciences and Engineering, 40 (2018) 233.

[42] A. Gök, K. Gök, M.B. Bilgin, M.A. Alkan, Effects of cutting parameters and tool-path strategies on tool acceleration in ball-end milling, Materials and Technology, 51 (2017) 957-965.

[43] E.O. Ezugwu, Z.M. Wang, A.R. Machado, Wear of coated carbide tools when machining nickel (Inconel 718) and titanium base (Ti-6Al-4V) alloys, Tribology Transactions, 43 (2000) 263-268.

[44] Y.S. Liao, R.H. Shiue, Carbide tool wear mechanism in turning of Inconel 718 superalloy, Wear, 193 (1996) 16-24.

[45] B. Davoodi, B. Eskandari, Tool wear mechanisms and multi-response optimization of tool life and volume of material removed in turning of N-155 iron–nickel-base superalloy using RSM, Measurement, 68 (2015) 286-294.

[46] B. Davoodi, B. Eskandari, Surface roughness optimization i n machining of N-155 iron-nickel-base superalloy using the taguch i method, Aerospace Mechanics Journal, 11 (2015) 43-53.

[47] J. Ning, V. Nguyen, S.Y. Liang, Analytical modeling of machining forces of ultra-fine-grained titanium, The International Journal of Advanced Manufacturing Technology, 101 (2019) 627-636.

[48] E.O. Ezugwu, J. Bonney, Effect of high-pressure coolant supply when machining nickel-base, Inconel 718, alloy with coated carbide tools, Journal of Materials Processing Technology, 153-154 (2004) 1045-1050.

[49] Z. Fang, T. Obikawa, Turning of Inconel 718 using inserts with cooling channels under high pressure jet coolant assistance, Journal of Materials Processing Technology, 247 (2017) 19-28.

[50] F. Pusavec, H. Hamdi, J. Kopac, I.S. Jawahir, Surface integrity in cryogenic machining of nickel based alloy—Inconel 718, Journal of Materials Processing Technology, 211 (2011) 773-783.

[51] N. Khanna, C. Agrawal, M.K. Gupta, Q. Song, Tool wear and hole quality evaluation in cryogenic Drilling of Inconel 718 superalloy, Tribology International, 143 (2020) 106084.

[52] A. Devillez, F. Schneider, S. Dominiak, D. Dudzinski, D. Larrouquere, Cutting forces and wear in dry machining of Inconel 718 with coated carbide tools, Wear, 262 (2007) 931-942.

[53] K. Khanafer, A. Eltaggaz, I. Deiab, H. Agarwal, A. Abdul-latif, Toward sustainable micro-drilling of Inconel 718 superalloy using MQL-Nanofluid, The International Journal of Advanced Manufacturing Technology, 107 (2020) 3459-3469.

[54] K. Pang, D. Wang, Study on the performances of the drilling process of nickel-based superalloy Inconel 718 with differently micro-textured drilling tools, International Journal of Mechanical Sciences, 180 (2020) 105658.

[55] A. Thakur, S. Gangopadhyay, State-of-the-art in surface integrity in machining of nickel-based super alloys, International Journal of Machine Tools and Manufacture, 100 (2016) 25-54.

[56] G. Venkatesh, D. Chakradhar, Influence of thermally assisted machining parameters on the machinability of Inconel 718 superalloy, Silicon, 9 (2017) 867-877.

[57] S. Azhdari Tadavani, R. Shoja Razavi, R. Vafaei, Pulsed laser-assisted machining of Inconel 718 superalloy, Optics & Laser Technology, 87 (2017) 72-78.

[58] W. Bai, A. Bisht, A. Roy, S. Suwas, R. Sun, V.V. Silberschmidt, Improvements of machinability of aerospace-grade Inconel alloys with ultrasonically assisted hybrid machining, The International Journal of Advanced Manufacturing Technology, 101 (2019) 1143-1156.

[59] A. Bhatt, H. Attia, R. Vargas, V. Thomson, Wear mechanisms of WC coated and uncoated tools in finish turning of Inconel 718, Tribology International, 43 (2010) 1113-1121.

[60] Y. Kaynak, Evaluation of machining performance in cryogenic machining of Inconel 718 and comparison with dry and MQL machining, The International Journal of Advanced Manufacturing Technology, 72 (2014) 919-933.

[61] N.H.A. Halim, C.H.C. Haron, J.A. Ghani, M.F. Azhar, Tool wear and chip morphology in high-speed milling of hardened Inconel 718 under dry and cryogenic CO2 conditions, Wear, 426-427 (2019) 1683-1690.

[62] H. Hegab, U. Umer, M. Soliman, H.A. Kishawy, Effects of nano-cutting fluids on tool performance and chip morphology during machining Inconel 718, The International Journal of Advanced Manufacturing Technology, 96 (2018) 3449-3458.

[63] J. Zhou, J. Yang, Z. Zhang, W. Liu, Q. Xue, Study on the structure and tribological properties of surface-modified Cu nanoparticles, Materials Research Bulletin, 34 (1999) 1361-1367.

[64] L. Rapoport, Y. Feldman, M. Homyonfer, H. Cohen, J. Sloan, J.L. Hutchison, R. Tenne, Inorganic fullerene-like material as additives to lubricants: structure–function relationship, Wear, 225-229 (1999) 975-982.

[65] S. Chen, W. Liu, L. Yu, Preparation of DDP-coated PbS nanoparticles and investigation of the antiwear ability of the prepared nanoparticles as additive in liquid paraffin, Wear, 218 (1998) 153-158.

[66] Q. Xue, W. Liu, Z. Zhang, Friction and wear properties of a surface-modified TiO2 nanoparticle as an additive in liquid paraffin, Wear, 213 (1997) 29-32.

[67] W. Liu, S. Chen, An investigation of the tribological behaviour of surface-modified ZnS nanoparticles in liquid paraffin, Wear, 238 (2000) 120-124.

[68] J. Zhou, Z. Wu, Z. Zhang, W. Liu, H. Dang, Study on an antiwear and extreme pressure additive of surface coated LaF3 nanoparticles in liquid paraffin, Wear, 249 (2001) 333-337.

[69] S. Qiu , Z. Zhou, J. Dong , G. Chen, Preparation of Ni nanoparticles and evaluation of their tribological performance as potential additives in oils, Journal of Tribology, 123 (1999) 441-443.

[70] A.A.D. Sarhan, M. Sayuti, M. Hamdi, Reduction of power and lubricant oil consumption in milling process using a new SiO2 nanolubrication system, The International Journal of Advanced Manufacturing Technology, 63 (2012) 505-512.

[71] B. Rahmati, A.A.D. Sarhan, M. Sayuti, Morphology of surface generated by end milling AL6061-T6 using molybdenum disulfide (MoS2) nanolubrication in end milling machining, Journal of Cleaner Production, 66 (2014) 685-691.

[72] M. Li, T. Yu, R. Zhang, L. Yang, H. Li, W. Wang, MQL milling of TC4 alloy by dispersing graphene into vegetable oil-based cutting fluid, The International Journal of Advanced Manufacturing Technology, 99 (2018) 1735-1753.

[73] K.-H. Park, B. Ewald, P.Y. Kwon, Effect of Nano-Enhanced Lubricant in Minimum Quantity Lubrication Balling Milling, Journal of Tribology, 133 (2011) 031803.

[74] R. Singh, J.S. Dureja, M. Dogra, Performance evaluation of textured carbide tools under environment-friendly minimum quantity lubrication turning strategies, Journal of the Brazilian Society of Mechanical Sciences and Engineering, 41 (2019) 87.

[75] T. Lv, S. Huang, E. Liu, Y. Ma, X. Xu, Tribological and machining characteristics of an electrostatic minimum quantity lubrication (EMQL) technology using graphene nano-lubricants as cutting fluids, Journal of Manufacturing Processes, 34 (2018) 225-237.

[76] S. Bhowmick, B. Eskandari, G. Krishnamurthy, A.T. Alpas, Effect of WS2 particles in cutting fluid on tribological behaviour of Ti–6Al–4V and on its machining performance, Tribology - Materials, Surfaces & Interfaces, (2020) 1-14.

[77] X. Tao, Z. Jiazheng, X. Kang, The ball-bearing effect of diamond nanoparticles as an oil additive, Journal of Physics D: Applied Physics, 29 (1996) 2932-2937.

[78] O. Elomaa, V.K. Singh, A. Iyer, T.J. Hakala, J. Koskinen, Graphene oxide in water lubrication on diamond-like carbon vs. stainless steel high-load contacts, Diamond and Related Materials, 52 (2015) 43-48.

[79] H. Kinoshita, Y. Nishina, A.A. Alias, M. Fujii, Tribological properties of monolayer graphene oxide sheets as water-based lubricant additives, Carbon, 66 (2014) 720-723.

[80] A. Gök, H.I. Demirci, K. Gök, Determination of experimental, analytical, and numerical values of tool deflection at ball end milling of inclined surfaces, Proceedings of the Institution of Mechanical Engineers, Part E: Journal of Process Mechanical Engineering, 230 (2014) 111-119.

[81] S. Ghosh, I. Calizo, D. Teweldebrhan, E.P. Pokatilov, D.L. Nika, A.A. Balandin, W. Bao, F. Miao, C.N. Lau, Extremely high thermal conductivity of graphene: Prospects for thermal management applications in nanoelectronic circuits, Applied Physics Letters, 92 (2008) 151911.

[82] A.A. Balandin, S. Ghosh, W. Bao, I. Calizo, D. Teweldebrhan, F. Miao, C.N. Lau, Superior Thermal Conductivity of Single-Layer Graphene, Nano Letters, 8 (2008) 902-907.

[83] D. Berman, A. Erdemir, A.V. Sumant, Graphene: a new emerging lubricant, Materials Today, 17 (2014) 31-42.

[84] S. Bhowmick, A. Banerji, A.T. Alpas, Role of humidity in reducing sliding friction of multilayered graphene, Carbon, 87 (2015) 374-384.

[85] S. Bhowmick, Z. Yang, A. Banerji, A.T. Alpas, Effect of graphene nanoplates dispersed in ethanol on frictional behaviour of tool steel running against uncoated and DLC-coated tool steel, Tribology Letters, 67 (2019) 32.

[86] R.B. Pavan, A. Venu Gopal, M. Amrita, B.K. Goriparthi, Experimental investigation of graphene nanoplatelets–based minimum quantity lubrication in grinding Inconel 718, Proceedings of the Institution of Mechanical Engineers, Part B: Journal of Engineering Manufacture, 233 (2017) 400-410.

[87] M. Shaw, P. Smith, Methods of applying cutting fluids, American Society of Tool and Manufacturing Engineers (ASTME), (1956).

[88] Y. Yildiz, M. Nalbant, A review of cryogenic cooling in machining processes, International Journal of Machine Tools and Manufacture, 48 (2008) 947-964.

[89] S.H. Musavi, B. Davoodi, B. Eskandari, Pre-cooling Intensity Effects on Cooling Efficiency in Cryogenic Turning, Arabian Journal for Science and Engineering, 44 (2019) 10389-10396.

[90] S.Y. Hong, Z. Zhao, Thermal aspects, material considerations and cooling strategies in cryogenic machining, Clean Products and Processes, 1 (1999) 107-116.

[91] S.Y. Hong, Y. Ding, J. Jeong, Experimental evaluation of friction coefficient and liquid nitrogen lubrication effect in cryogenic machining, Machining Science and Technology, 6 (2002) 235-250.

[92] A. Iturbe, E. Hormaetxe, A. Garay, P.J. Arrazola, Surface integrity analysis when machining Inconel 718 with conventional and cryogenic cooling, Procedia CIRP, 45 (2016) 67-70.

[93] F. Pusavec, A. Deshpande, S. Yang, R. M'Saoubi, J. Kopac, O.W. Dillon, I.S. Jawahir, Sustainable machining of high temperature Nickel alloy – Inconel 718: part 1 – predictive performance models, Journal of Cleaner Production, 81 (2014) 255-269.

[94] V. Tebaldo, G.G. di Confiengo, M.G. Faga, Sustainability in machining: “Eco-friendly” turning of Inconel 718. Surface characterisation and economic analysis, Journal of Cleaner Production, 140 (2017) 1567-1577.

# CHAPTER 3

# FLOODED DRILLING OF INCONEL 718 USING GRAPHENE INCORPORATING CUTTING FLUID

## 3.1. INTRODUCTION

In this chapter, the idea of using graphene mixed with cutting fluids in machining of Inconel 718 is investigated, as they could provide low COF and high rates of heat transfer. The objectives of this chapter is two folds, (i) investigation of tribological behaviour of Inconel 718 against WC-Co using different concentrations of graphene in cutting fluid and characterization of the contact surfaces for the formation of tribolayers responsible for low COF and (ii) conducting drilling tests on Inconel 718 (using the results of the sliding contact tests that determined the concentration of graphene which provided the lowest COF) and to examine whether the formation of tribolayers would play a role in reducing cutting torques, tool wear and surface roughness of the drilled holes. The results showed that in order to rationalize the underlying mechanisms accountable for the reduction in cutting torques and tool wear observed in drilling of Inconel 718 using graphene in the cutting fluid, a tribological approach was useful.

## 3.2. EXPERIMENTAL

### 3.2.1. Workpiece and Tool Materials

The workpiece samples were hot rolled slab made of Inconel 718 alloy received in the dimension of 30×15×2.54 $cm^3$. The composition (wt.%) of the Inconel 718 was as follows: Ni 53.84%, Fe 18.02%, Cr 17.98%, Ca <10 PPM, Nb+Ta 5.39%, Nb 5.38%, Mo 2.92%, Ti 0.96%, Al 0.47%, Co 0.35%, Mn 0.09%, Si 0.08%, Cu 0.05%, C 0.02%, P 0.01%, B 0.004%, S 0.0003%, Ta <0.01, Mg <0.01. The surfaces of samples were prepared using SiC grinding papers with 600, 800 and 1200 grits and then polished to 3 µm and finally to 1 µm. The samples were etched in a solution of 95% HCl and 5% $H_2O_2$ for 35-40 seconds. The Inconel 718 samples exhibited the typical bimodal grain structure containing small (19 ± 3 µm) and large grains (60 ± 10 µm) with hardness values of 290 HV and 243 HV. Figure 57 shows the optical microstructure of the as-received Inconel 718 after etching.

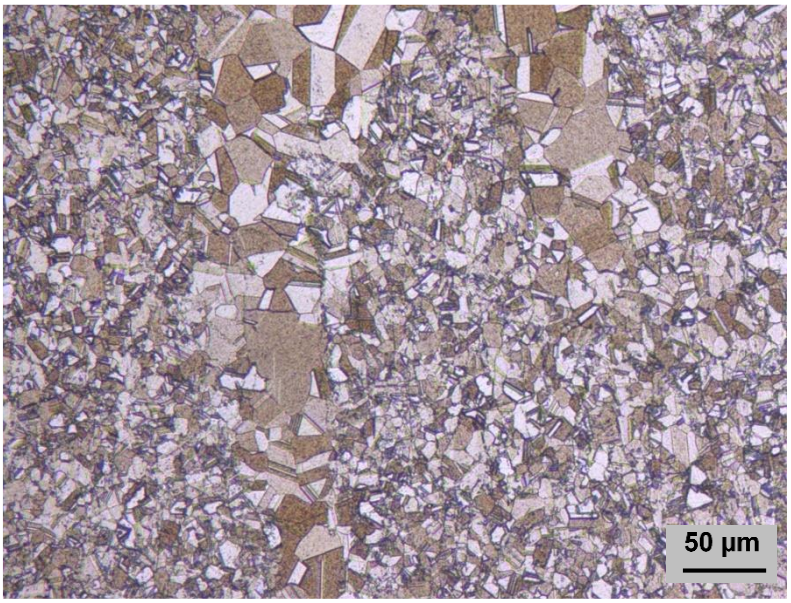


Figure 57 Optical microstructure of as received Inconel 718.

### 3.2.2. Tribological Tests

A pin-on-disk type tribometer was used for measuring the COF between WC-Co and Inconel 718. Inconel 718 pins with a radius of 4 mm and disks of WC-Co with a radius of 25 mm were used. The tests were done for 1000 revolutions at a speed of $5\times10^{-2}$ m/s. The normal load used in the tests was 5.0 N. The measured COF values were plotted against the number of revolutions. The COF curves exhibited two stages: (i) running-in stage where the COF ($\mu_r$), had the highest value during initial sliding period, and (ii) steady-state stage COF ($\mu_{ss}$), which was calculated from the arithmetic mean of the COF signals in the stage following the initial running in. Three tests were conducted under each condition (GCF, CF, dry) explained in the next paragraph and the average $\mu_r$ and $\mu_{ss}$ values were calculated. The details of calculation of $\mu_r$ and $\mu_{ss}$ values can be found in [1, 2].

Sliding tests were conducted under different tests conditions consisting of i) unlubricated sliding; ii) lubricated sliding using cutting fluid without graphene (CF), and iii) lubricated sliding using cutting fluid with graphene (GCF) in size of graphene particles is $7\pm2$ micron as determined by SEM. The cutting fluid consisted of 70% water and 30% vegetable oil with P additives. The optimum concentration of graphene to be added to the cutting fluid was determined by performing sliding tests with different wt.% of graphene. The graphene percentage that resulted in the lowest COF was considered as the optimum concentration, which was used during the machining process. The lubrication regime was determined from the ratio ($\lambda$) of minimum film thickness ($h_{min}$) to the root mean square (r.m.s) roughness of the contacting surfaces [3]. The parameters used for lubrication regime calculation are shown in Table 3.

E*, composite elastic modulus (in GPa) and the minimum lubrication thickness $h_{min}$ was calculated using following equations:

$$\frac{1}{E^*} = \frac{1-\vartheta_{Inconel718}^2}{E_{Inconel718}} + \frac{1-\vartheta_{WC-Co}^2}{E_{WC-Co}} \quad (13)$$

$$h_{min} = 1.79R^{0.47}\alpha^{0.49}\eta_0^{0.68}V^{0.68}E^{*-0.12}p^{-0.07} \quad (14)$$

$\eta_0$ = viscosity constant of lubricants,
$\alpha$ = lubricant pressure viscosity coefficient,
r* = r.m.s. surface roughness of the contacting surfaces.
$E_{Inconel718}$ = 200 GPa,
$E_{WC-Co}$ = 600 GPa,
Poisson's ratio of Inconel 718 ($\vartheta_{Inconel\,718}$) = 0.29
Poisson's ratio of WC-Co ($\vartheta_{WC-Co}$) = 0.21.

As $\lambda$=0.01 for tests done in CF, a boundary lubrication condition prevailed [3]. The boundary lubrication condition was chosen for maximizing the deformation of the graphene particles during the sliding and drilling experiments. The graphene nanoparticles were added to the cutting fluids and were then mechanically stirred for 45 minutes. To prevent agglomeration of the graphene nanoparticles, the cutting fluids were freshly blended with nanoparticles just before conducting the sliding friction and orthogonal cutting experiments.

Table 3 Parameters used to calculate the lubrication condition, $\lambda=h_{min}/r^*$, for Inconel 718 in sliding contact with WC-Co in CF.

| $R$ (m) | $V$ (m/s) | $P$ (N) | $E^*$ (GPa) | $r^*$ (µm) | $\eta_0$ (Pa.s) | $\alpha$ ($10^{-8}$) | $h_{min}$ (µm) | $\lambda$ |
|---|---|---|---|---|---|---|---|---|
| 0.002 | 0.12 | 5 | 200 | 0.49 | 0.075 | 2.41 | 0.003 | 0.01 |

R = radius of the pin and counterface, m,
V = sliding velocity, m/s,
P = normal load, N.

### 3.2.3. Drilling Tests: Torque and Temperature Measurements

A CNC machine was used to conduct the drilling tests on Inconel 718 workpieces at a rotational speed of 2500 rpm and a feed rate of 0.05 mm/rev. The tool material (twist drill) was uncoated WC-Co with a diameter of 4.05±0.01 mm. The hardness and elastic modulus of WC-Co were 1397 HV (13.7 GPa) and 414.1 GPa. Tests were done using cutting fluid (CF) and GCF ($54\times10^{-5}$ wt.% graphene) supplied at the pressure of 60 psi. The tests consisted of drilling of 50 holes consecutively. Each hole was drilled to a constant depth of 12 mm. The cutting torque was measured using a magnetostatic sensor mounted on rotating shaft of the drilling machine [4-8]. The criterion for determining the tool life was determination of the number of the hole for which a 4.00-mm dowel would no longer be inserted. The temperature increase in the workpiece during the machining process was measured by inserting a K-type chromel-alumel thermocouple at the end of the last drilled hole [9]. The thermocouple was connected to the IOTeck DAQ with data resolution of 16 bit.

### 3.2.4. Characterization of Tribolayers Formed During Sliding and Drilling Tests

A Scanning electron microscope (SEM) was used to examine the tool wear after the drilling experiments by using a high voltage of 20 kV. A distance of 10 mm was set between the sample and the electron detector. Surface morphologies of the drilled holes were observed with an optical surface profilometer by which the average surface roughness (arithmetical mean height, Sa) values were obtained. The compositions of tribolayer formed on the top of the drill's cutting edge were studied using a Raman spectrometer with solid-state laser (50 mW Nd-YAG, 532.0 nm excitation line).

## 3.3. RESULTS

### 3.3.1. Lubricated Sliding Friction Of WC-Co Vs. Inconel 718 Using CF and GCF

Variations of COF with sliding cycles for WC-Co sliding against Inconel 718 under the boundary lubricated sliding condition using CF with different graphene percentages are shown in Figure 58(a, b). During unlubricated sliding, a high COF of 0.60 was generated. The COF curves were marked by large fluctuations and neither a distinguishable running in nor a steady state friction regime was recorded. As shown in Figure 58(a), using CF without graphene, the COF was reduced to $\mu_s$ = 0.15, a steady state friction regime with smaller fluctuations was observed. The initial peak in the COF curve corresponded to $\mu_R$ of 0.17. Further decrease in COF was observed when graphene was added in increasing volume percentages in CF (Figure 58(b)). The results showed that regardless of the concentration of the graphene, the sliding tests with GCF resulted in lower COF than when CF without the graphene was used. The average COF of three tests curves exhibited running-in and steady state regimes are presented in Figure 59(a, b). For tests conducted in the GCF with $54\times10^{-5}$ wt.% graphene in CF, the lowest $\mu_R$ of 0.086 and $\mu_s$ of 0.080 were recorded. This graphene concentration was selected to be used as in the cutting fluid in the drilling tests of Inconel 718 with WC-Co tool, as described in the Section 3.3.2.

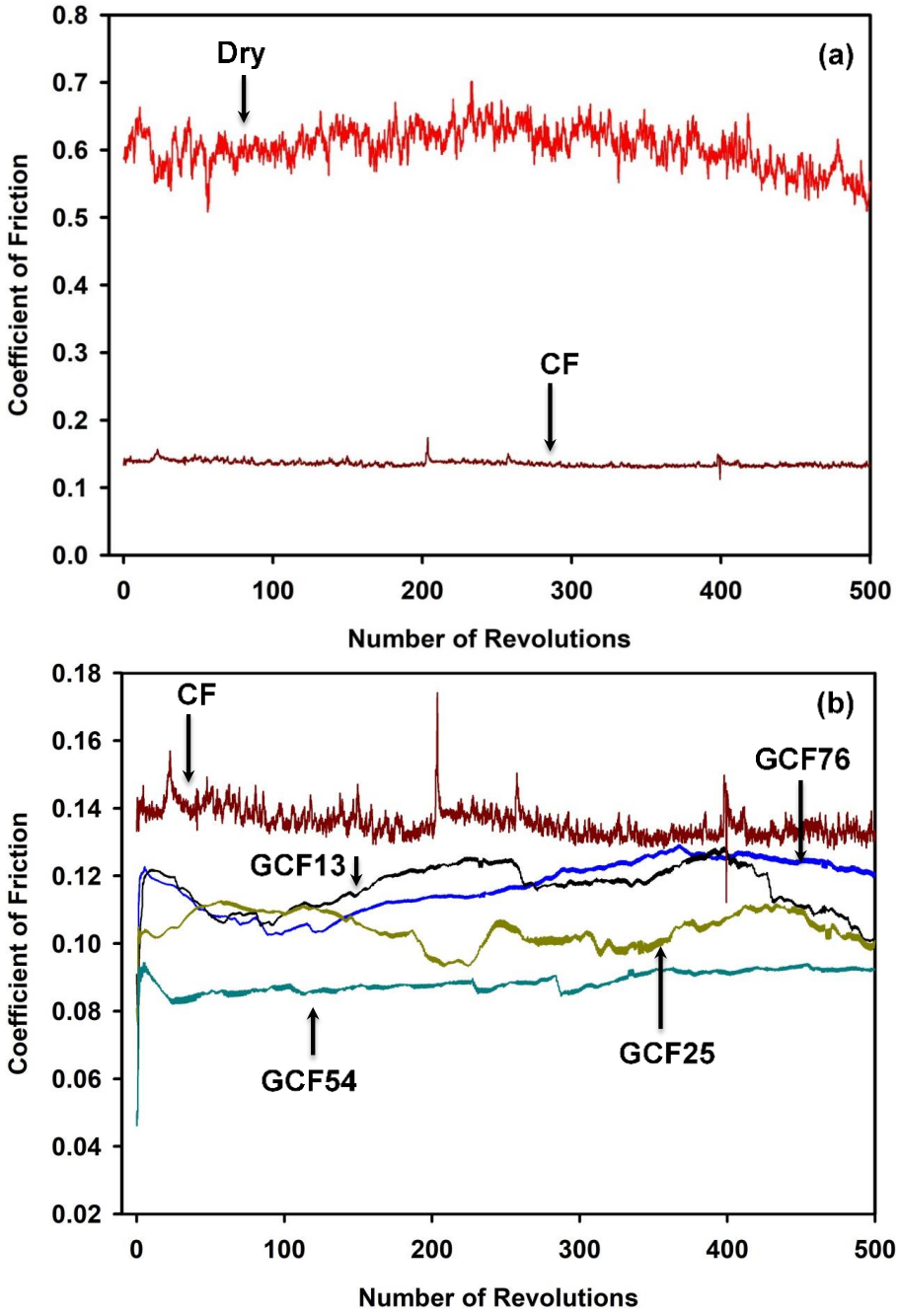


Figure 58 Variation of COF with the number of revolutions when WC-Co was tested against Inconel 718 counterface in (a) dry and CF, (b) lubricated conditions with varying concentrations (GCF) where GCF13=$13\times10^{-5}$ wt.% graphene, GCF25=$25\times10^{-5}$ wt.% graphene, GCF54=$54\times10^{-5}$ wt.% graphene and GCF76=$76\times10^{-5}$ wt.% graphene.

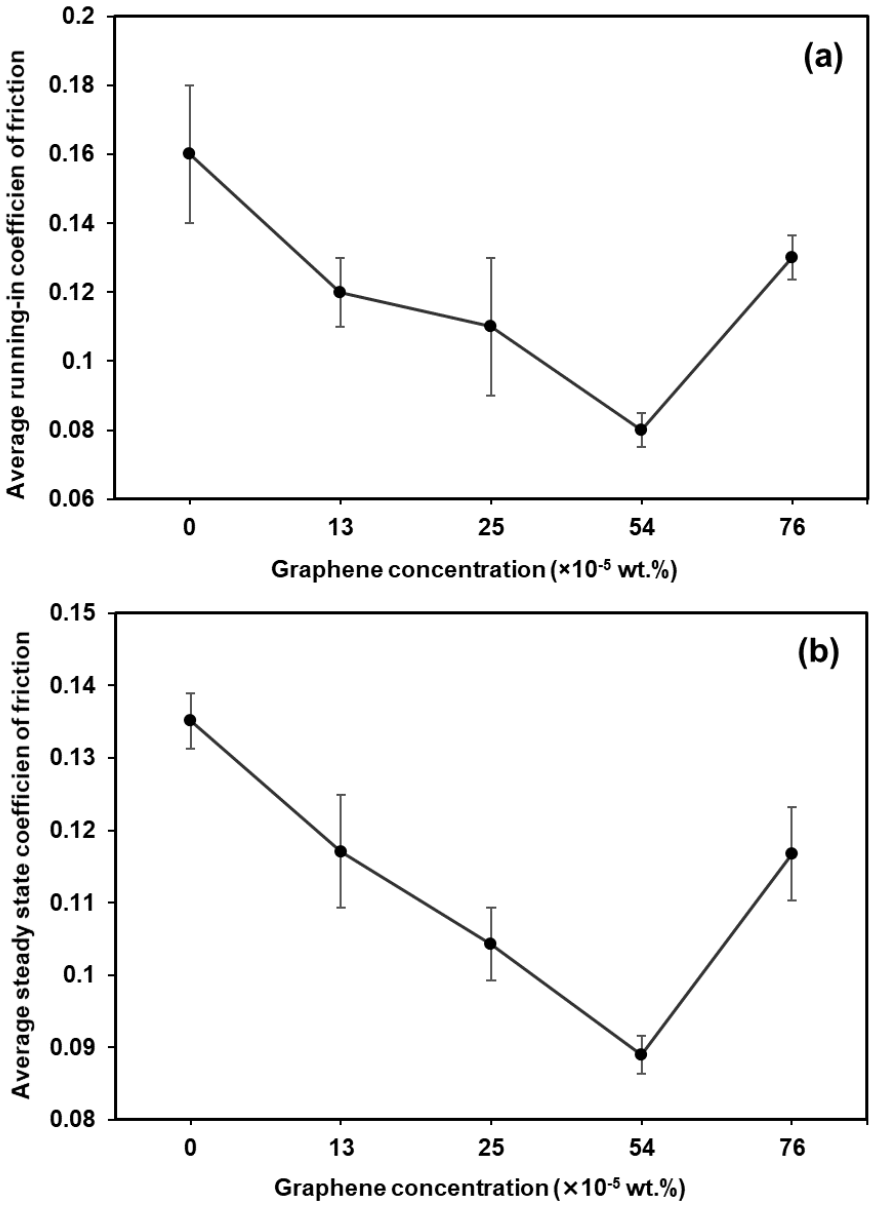


Figure 59 Variation of (a) running-in and (b) steady state COF for CF and GCF lubricated sliding conditions with varying concentrations. Each point represents the average value of the three iterative tests performed in all test conditions. The error bars denote the standard deviation about the mean COF value from the three iterative tests.

Figure 60(a) shows a secondary electron image (SEI) of the wear track generated on the WC-Co surfaces which is typical image showing tribolayers that were formed at the wear track in the form of discrete patches located usually along the boundaries of the wear track and aligned in

the sliding direction during the lubricated test using GCF. The EDS map shows that the tribolayers incorporated carbon (Figure 60(b)). The elemental C distribution map in Figure 60(b) suggests that graphene in the cutting fluid became deposited on the wear track during sliding contact. The examination of the Inconel 718 sliding surfaces provided evidence for severe plastic deformation at the contact surface and formation of long deformed fragments extruding forward ahead of sliding contact surface Figure 60(c). The EDS maps such as the one shown in Figure 60(d) showed that the extruded fragments were rich in C (Figure 60 (d)). Therefore, graphene particles deposition on the worn surfaces occurred simultaneously with sliding induced plastic deformation of Inconel 718. The Inconel 718 pin contact surfaces were also examined after sliding tests conducted using CF and a SEM image is shown in Figure 61(a). In this case no noticeable transfer layer could be observed on the contact surface of Inconel 718 (Figure 61 (a)). Along the alloying elements (Ni) only presence of O was detected on the wear scar (Figure 61(b, c)). The pin-on disk tests, therefore, revealed that GCF when used as a lubricant during the sliding tests reduced the COF of Inconel 718 by forming tribolayers on the top of both pin and disk surfaces.

### 3.3.2. Drilling Torque in Dry, CF (With 0 Wt.% Graphene) And GCF (CF with $54\times10^{-5}$ Wt.% Graphene)

Inconel 718 was first subjected to drilling without using CF, i.e., drilled in dry condition and during these tests the WC-Co drill failed after only after drilling a few holes due adhesion of Inconel 718 and also due to tool wear. Figure 62 (a) shows the variations of measured drilling torque values with the drilling time recorded during dry drilling using WC-Co drills. A high torque >7 Nm, while drilling the third hole was observed and tool failure occurred. In

comparison, during the drilling tests using flooded CF drill failure did not occur for the entire duration of the test consisting of 50 holes. The values of maximum and average torques were low compared to those generated during drilling in dry condition (Figure 62(b)). However, during flooded CF drilling, torque spikes were observed during drilling of several holes (Figure 62 (b)). When drilling was conducted using cutting fluid with $54\times10^{-5}$ wt.% graphene (GCF), the average torque was not only low but also stable. The torque spikes were occasionally observed and the peak values were smaller (Figure 62(c)). The result are summarized in Figure 62(d) which shows a constant average torque from the first hole to the $50^{th}$ hole (2.01 ± 0.02 N-m).

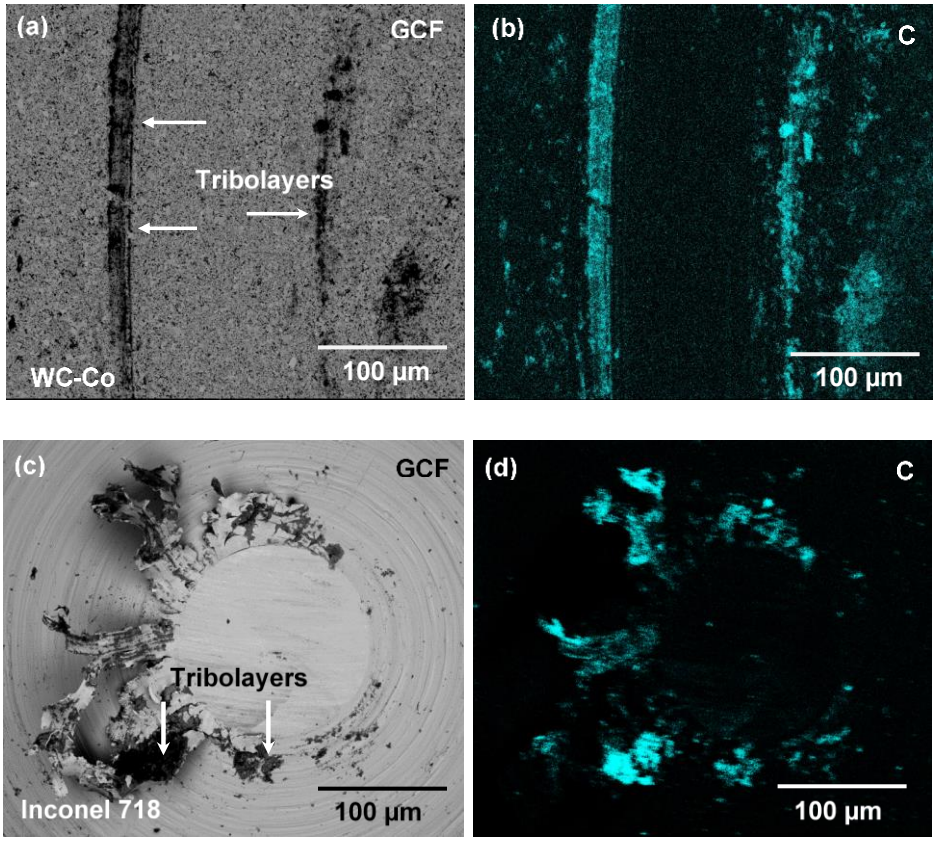


Figure 60 (a) Typical secondary electron images of wear tracks formed on the WC-Co surface when tested against Inconel 718 using GCF as lubricant. The elemental EDS map taken from (a) is shown in (b) for C, (c) Secondary electron image of the Inconel 718 pin surface taken after sliding against WC-Co at GCF condition. The elemental EDS map taken from (c) is shown in (d) for C.

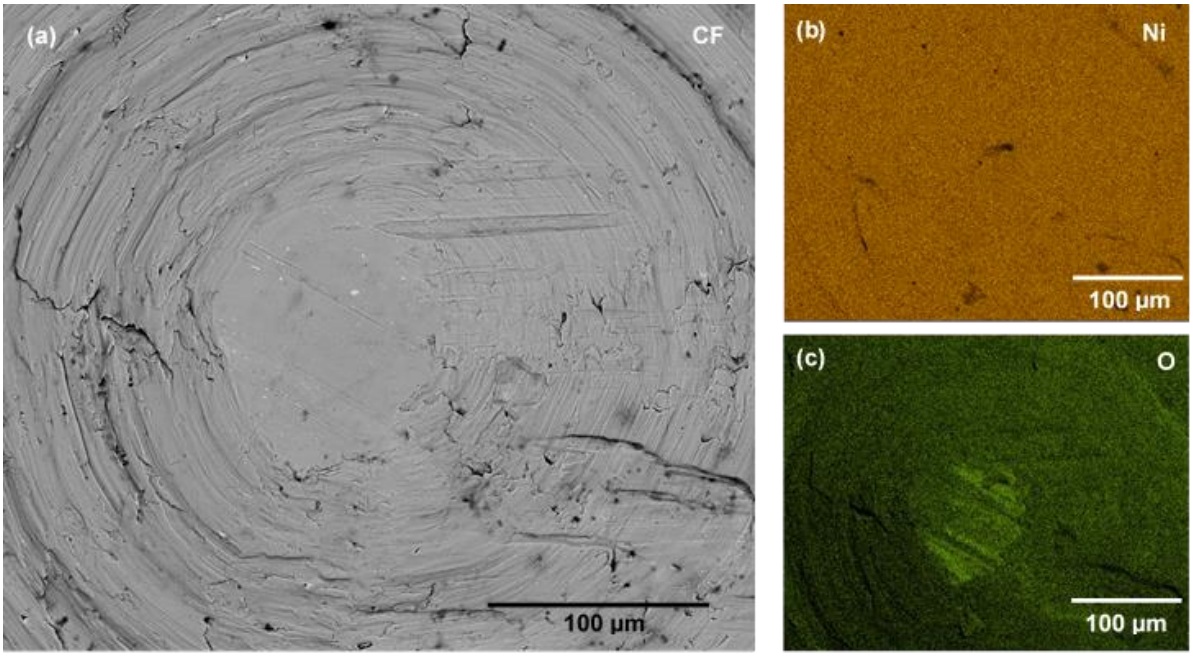


Figure 61 (a) Typical secondary electron images of wear tracks formed on the WC-Co surface when tested against Inconel 718 using CF as lubricant. The elemental EDS maps taken from the area shown in (a) are for (b) Ni and (c) O.

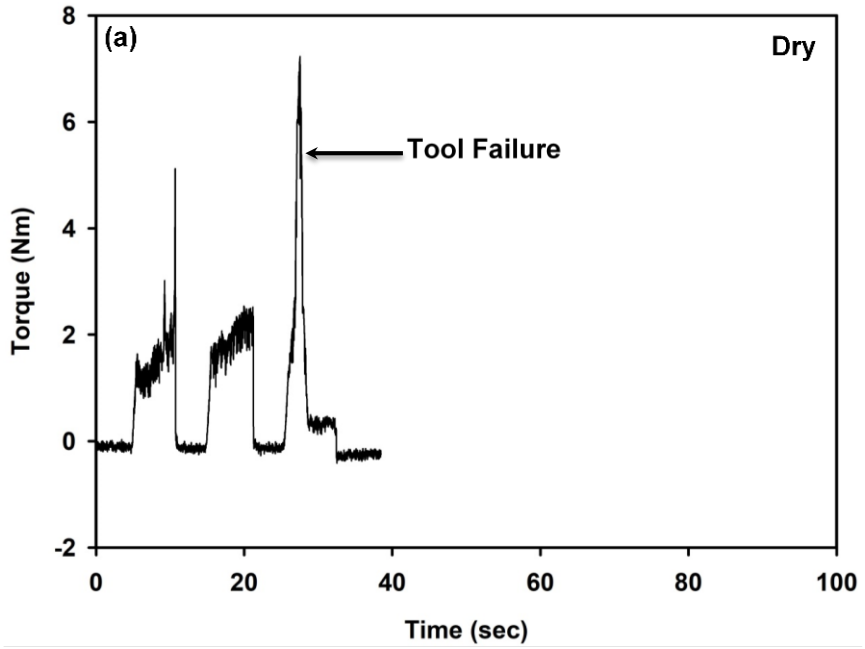
(a)
Dry
Tool Failure
Torque (Nm)
Time (sec)
8
6
4
2
0
-2
0
20
40
60
80
100

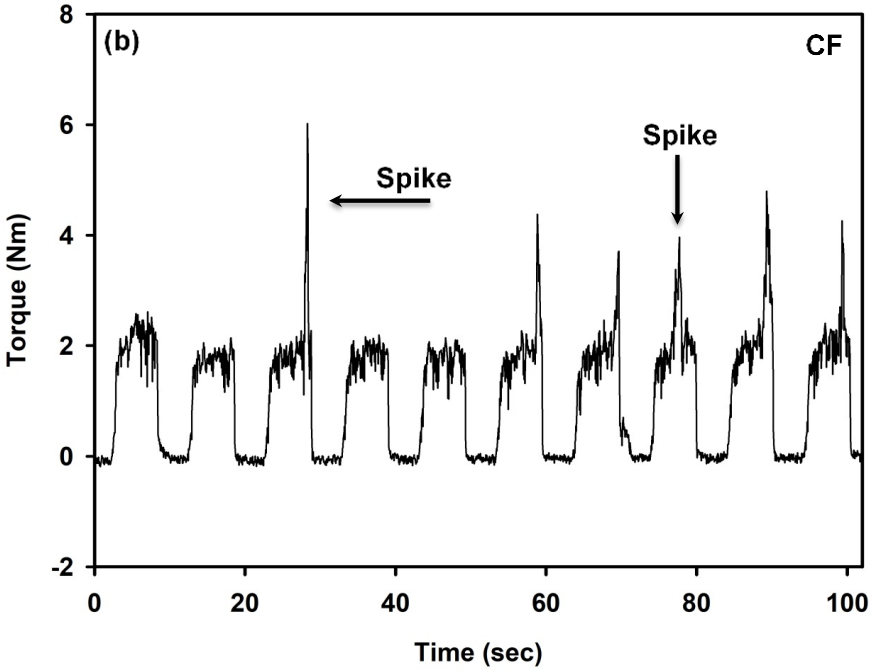
(b)
CF
Spike
Spike
Torque (Nm)
Time (sec)
8
6
4
2
0
-2
0
20
40
60
80
100

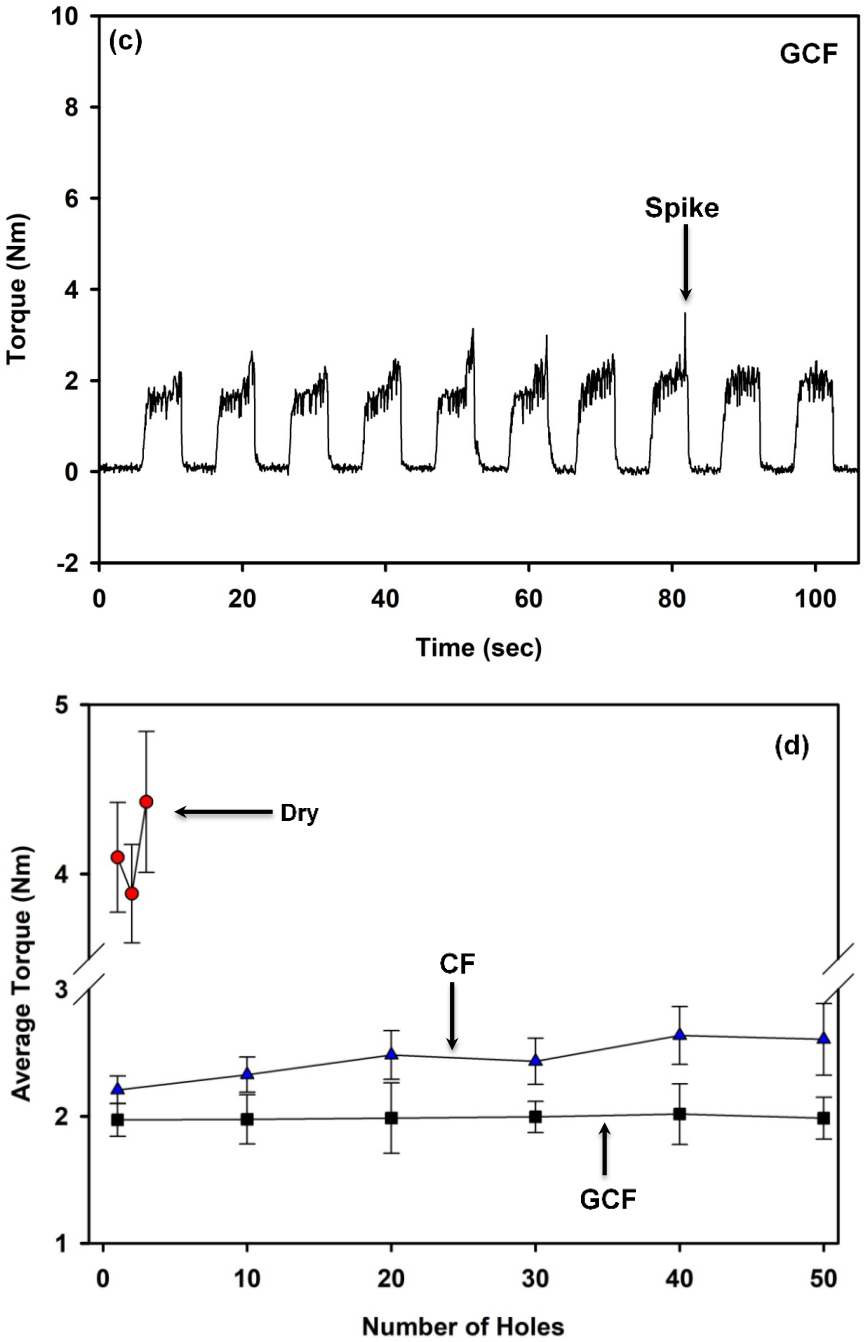


Figure 62 Variations (with time) of the torques generated during (a) dry, (b) CF, (c) GCF. Torque data are obtained for WC-Co in dry drilling until failure for CF and GCF conditions for 50 holes. (d) A comparison of average torques under dry, CF and GCF drilling conditions using WC-Co drills.

### 3.3.3. Temperature Increase During Drilling

The temperature values recorded during drilling of the first holes under each drilling condition and plotted as a function of the length of the hole as the drill moves inside Inconel 718 workpiece. The schematic illustration showing the cross-section of a drilled hole and the position of the thermocouple hole is shown in Figure 63(a). The temperature variations obtained in this way for dry drilling and drilling with CF and GCF are plotted in Figure 63(b). Accordingly, the maximum temperature attained during the dry drilling was 482 $^{o}$C at the base of the drilled hole, whereas when drilling using CF, the maximum temperature attained was 167 ºC and using GCF the temperature did not exceed 97 ºC. The temperature profile obtained during GCF drilling was more stable than the one generated using CF in drilling. The low and uniform temperature observed for GCF was due to the high thermal conductivity of graphene facilitating heat dissipation from tool-workpiece interfaces. It can be suggested that as the temperature generated during GFC drilling was low the amount of workpiece material adhering to the tool would be low as the material transfer phenomenon during drilling is affected by the softening behaviour of the workpiece at high temperatures. The tribolayers that were generated on the tool surface could assist maintaining low interface temperatures by reducing the COF hence lowering the drilling torque. These points will be examined in Section 3.4.

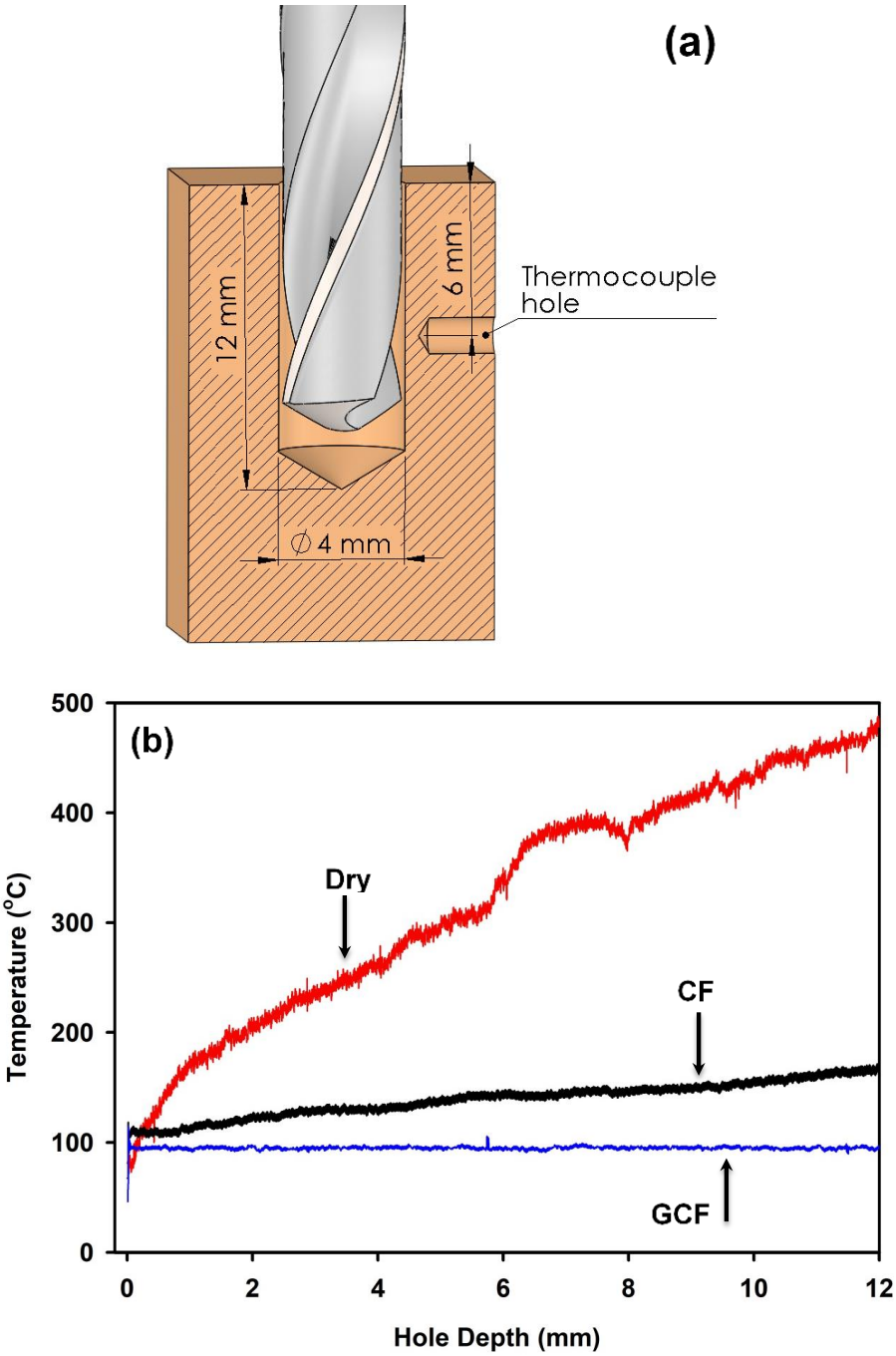


Figure 63 (a) Schematic illustration showing the cross-section of a drilled hole and the position of the thermocouple hole, (b)Variations (with hole depth) of temperature generated during dry, CF and GCF drilling of the first hole in each case.

### 3.3.4. SEM Observation of Cutting Edge of Drills

Material transfer from Inconel 718 to the WC-Co drill and adhesion of transferred material to drill flutes occurred during drilling in dry condition due to the temperature increase. Figure 64(a) shows the schematic illustration of the observed area of the drill cutting edge. Figure 64(b) shows the back scattered electron image of the cutting edge of drill flute used in dry condition. It was found that the entire cutting edge of the drill was converted by adhered material transferred from Inconel 718. The height of the BUE formed in this way was 300±130 µm. The use of CF reduced the adhesion of Inconel 718 and the height of the BUE was reduced to 142±31 µm. However, extensive tool edge chipping was observed after drilling 50 holes (Figure 64 (c)). The average depth of the chipped zone was 258±78 µm. On the other hand, the drill cutting edge did not exhibit detectable amount of adhesion of Inconel 718 when GCF was used. (Figure 64(d)).

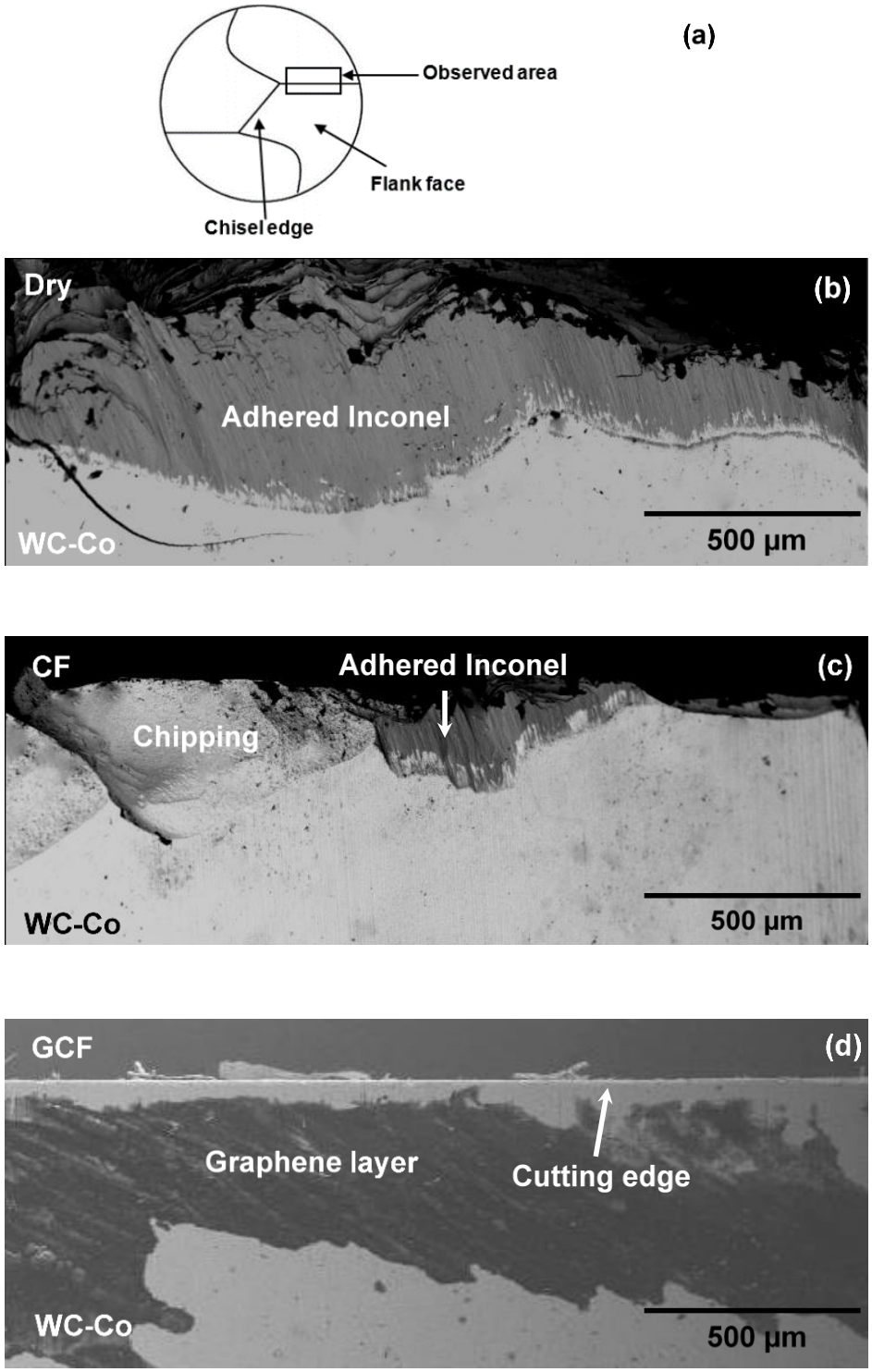


Figure 64 (a) The schematic illustration of the observed area of the drill cutting edge. Back scattered electron images of cutting edge of the WC-Co drills used in (b) dry, (c) CF and (d) GCF drilling conditions.

### 3.3.5. Subsurface Plastic Deformation During Drilling

Typical cross-sectional optical images showing plastically deformed subsurface zones under the surfaces of the holes drilled in Inconel 718 using dry, CF and GCF drilling conditions are given in Figure 65 (b-d). The surface with duplex grains (Figure 57) was perpendicular to the axis of the drill as shown in Figure 65(a).

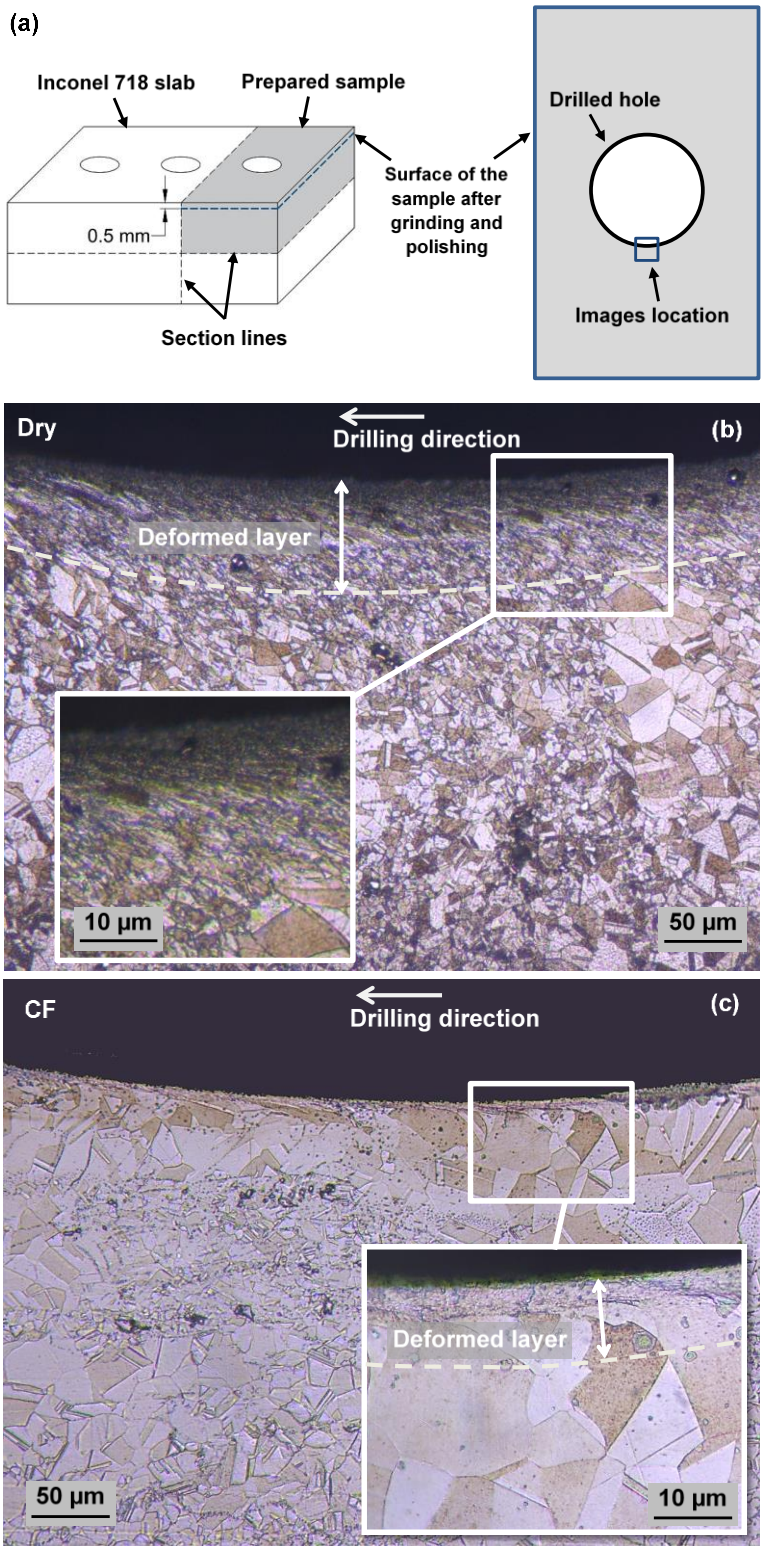
(a)
Inconel 718 slab
Prepared sample
0.5 mm
Section lines
Surface of the sample after grinding and polishing
Drilled hole
Images location
Dry
Drilling direction
(b)
Deformed layer
10 µm
50 µm
CF
Drilling direction
(c)
Deformed layer
50 µm
10 µm

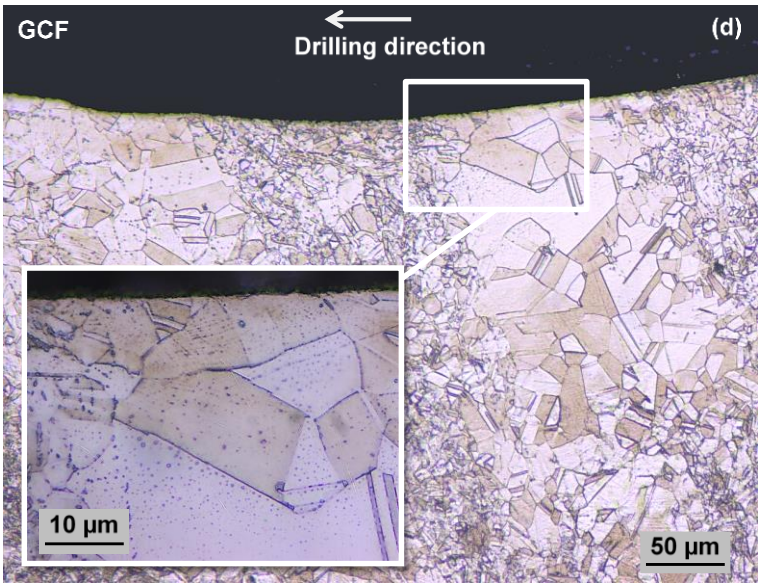


Figure 65 (a) Schematic illustration of the sample and the location of the images taken using optical microscopy. Typical cross-sectional optical images showing plastically deformed subsurface layers under the drilled holes on Inconel 718 formed under (b) dry, (c) CF and (d) GCF drilling conditions.

Deviations from the initial position of grain boundaries were considered to be due to the plastic shear strains [10] generated at the drilled Inconel 718 alloy's surface and subsurface regions. For each drilling experiment, at least 10 different locations below the hole surfaces of the last drilled hole were examined. The depth of plastic deformation zone for each condition were estimated from the observations of the changes in the grain microstructures near the drilled surface. For dry machining (Figure 65 (b)), the average depth of deformed zone was 75±6 µm. High COF in dry drilling (Figure 58 (b)) resulted in high adhesion of workpiece materials on the cutting tool (Figure 64 (b)) which changed the geometry of cutting edge (see Section 3.3.4), acting like a high radius cutting edge. This can be responsible for cutting of the workpiece material by ploughing action rather than shearing [11], leading to extrusion of the material between the tool and workpiece.

This process would result in generation of a high cutting force [12], which can be observed from Figure 62, and high subsurface deformation in dry drilling process. A smaller average depth of subsurface deformation of 12±3 μm was observed in CF drilling conditions (Figure 65(c)). In this condition, adhesion of Inconel 718 to the cutting edge was decreased (Figure 64(b)). Thus, shearing action, rather than ploughing action occurred. When drilling was made using GCF, plastic deformation was not detected as the grain boundary displacements were not easily observable at this magnification (Figure 65(d)). In some parts of the drilled hole, the deformation layer depth of 5±1 μm can be seen in Figure 65(c), however, in general the depth of deformation was approximately 1 μm. This is attributed to the fact that the cutting edge retained its original shape, and consequently, shear cutting action resulted in almost no deformation in the subsurface region of the machined workpiece.

### 3.3.6. Analysis of Surface Finish

The features of the hole surfaces drilled in different drilling conditions were examined using an optical surface profilometer. 3-D surface contours of the drilled holes are presented in Figure 66(a–c), which are the representative surface morphologies. The hole surfaces after dry drilling exhibited the highest surface roughness as expected (Figure 66(a)), while CF and GCF drilling produced smoother surfaces (Figure 66(b, c)). The changes in the arithmetic mean height ($S_a$) variations with the number of holes produced are plotted in Figure 66(d). The $S_a$ of the first hole was 5.27±1.06 μm in CF and 4.75 ±0.87 μm in GCF drilling conditions. The $R_a$ values of surfaces drilled using GCF was lower than the CF and did not raise with the holes number drilled. The surface roughness results indicated that the use of GCF provided an

improved drilled hole surface quality in addition to reducing the average torque when compared to CF drilling.

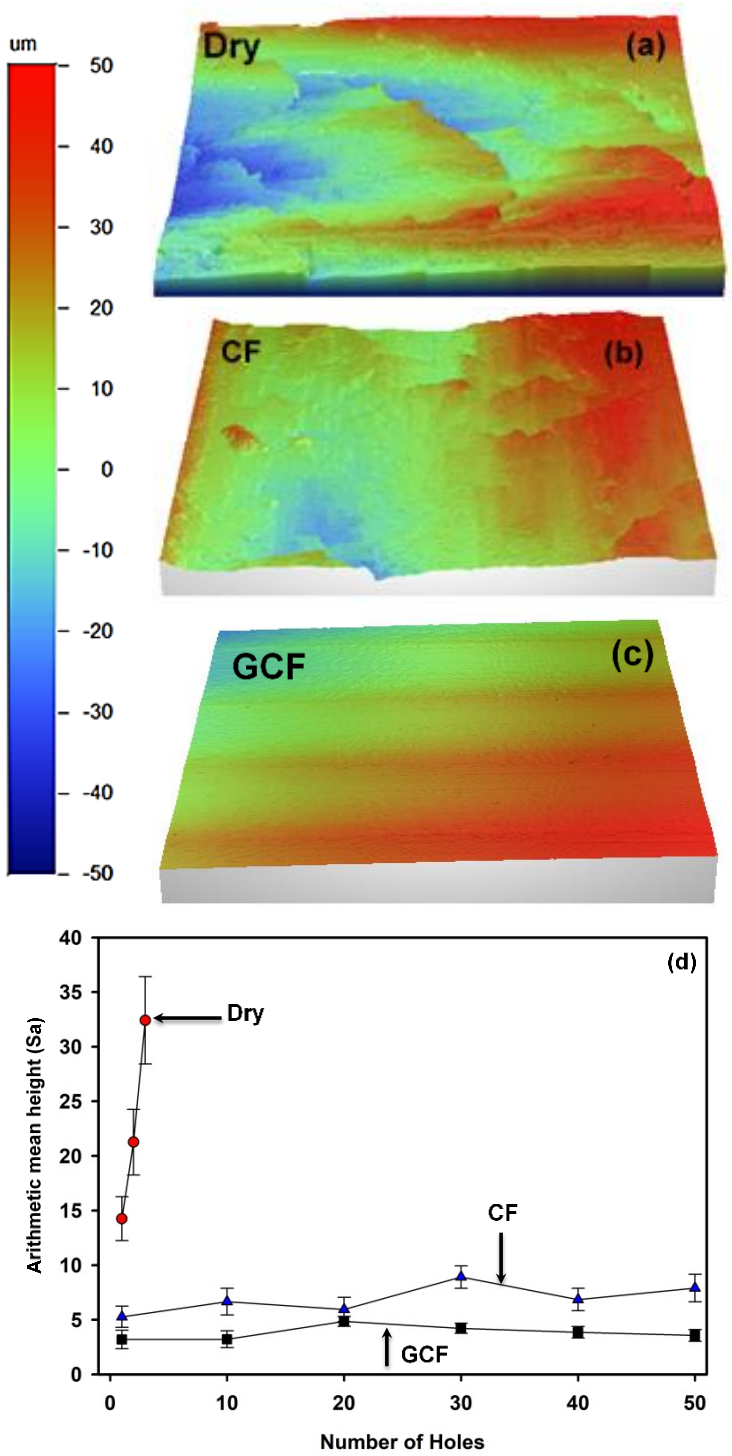


Figure 66 Three-dimensional optical surface profilometry images of typical surfaces of drilled holes using WC-Co drills in (a) dry, (b) CF and (c) GCF after drilling 50 holes. (d) Comparisons of arithmetic mean height ($S_a$) variations of drilled holes using WC-Co drills in dry, CF and GCF conditions.

### 3.4. DISCUSSION

It is instructive to analyze the effect of friction on drilling by examining the COF curves obtained using the tribological test that are described in Section 3.2.2. It is also useful to consider the morphological features of worn surfaces subjected to sliding. As presented in Figure 58(a), in lubricated sliding tests using CF, Inconel 718 in sliding against WC-Co, showed high COF values with large fluctuations about the mean COF values. In contrast, the use of $54\times10^{-5}$ wt.% graphene added to the cutting fluid (GCF) resulted in a lower running- in COF. A low steady-state COF with smaller fluctuations was also observed. A carbon rich tribolayer on the tool surface was also formed during drilling with GCF as evident from Figure 64(c) and this would likely reduce the COF between the tool and workpiece. The tribolayer formed on the WC-Co drill was further characterized using Raman spectroscopy. The spectrum obtained from the tribolayer was compared with that of the pristine graphene as shown in Figure 67. The Raman spectrum of the graphene in Figure 67 showed the characteristic G and 2D peaks of graphene at 1578 $cm^{-1}$ and 2705 $cm^{-1}$ respectively. As 2D/G <1 a multilayered graphene structure was predicted by this spectrum [13]. The low intensity of D-band of the as-received graphene suggested a structure with low defect density [14, 15]. The Raman spectra of tribolayers formed in sliding and drilling experiments (Figure 67) suggested that the graphene was subjected to damage; as revealed by high intensity of D bands.

Figure 67 (a-c) shows the D peaks of the Raman spectra obtained from the tribolayers were not only higher than the graphene before being subjected to sliding and drilling tests but their peak position shifted to ~1351 $cm^{-1}$ from the D peak's initial position, which was 1365 $cm^{-1}$ for the as-received graphene. The existence of (D+G) band at ~2735 $cm^{-1}$ can also be seen in

Figure 68(b, c). The D peak and occurrence of the (D+G) peak provided the evidence of sliding induced defect generation. The defects produced due to sliding include fracture at the edge of graphene and vacancy formation [14]. An increase in the concentration of vacancies and formation of edge defects would facilitate dissociation of H- and -OH from ethanol or water [15-19]. It is generally observed that the friction behavior of graphene involves formation of tribolayers on the counterface [15-19]. These tribolayers consist of graphene layers that were damaged during the sliding process and the graphene layers were weakened as a result of the dissociated H- and OH- that were absorbed by the layers at the defect sites, reducing the binding energies and increasing the spacing [14]. In general, these tribochemical mechanisms help to reduce the adhesive interactions, hence the COF, between the tools and workpieces surfaces. In

summary, the GCF drilling facilitated formation of a tribolayer on the tool surface. Thus, a low and stable torque was observed during drilling using GCF compared to CF.

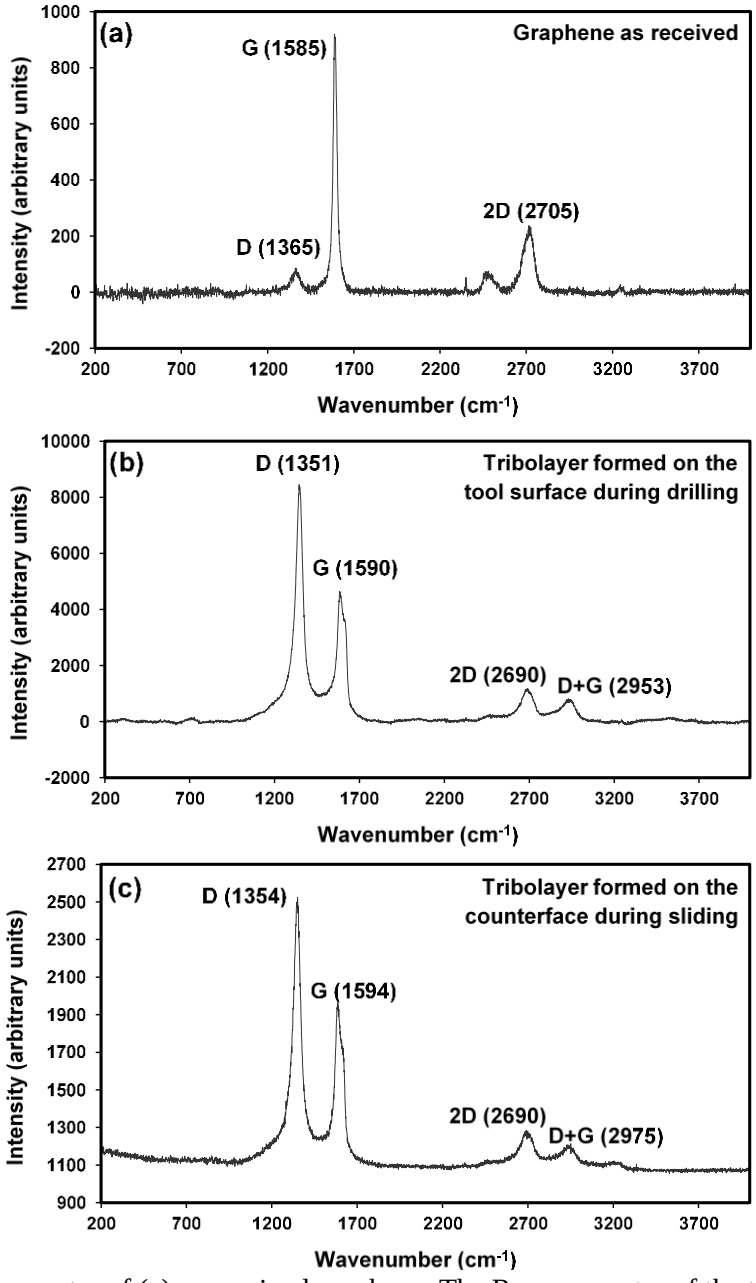


Figure 67 Raman spectra of (a) as received graphene. The Raman spectra of the tribolayer formed during (b) sliding test, and (c) drilling operation.

Another important aspect of graphene is thermal conductivity. The high thermal conductivity of graphene allowed easy dissipation of cutting temperature from the tool-workpiece interface. This is another factor that should be taken into account at the microstructural level because the higher temperatures, such as those generated during dry drilling would soften the material cause more deformation (Figure 65) and consequently promote adhesion resulting in high COF (Figure 58) and a high drilling torque (Figure 62). Thus, rationalization of the effect of graphene in cutting fluid on machining is complex as both atomistic and microstructural effects should be considered as discussed above. However, the advantages of the graphene addition to the cutting fluid are clear resulting in low and stable cutting forces and smoother surfaces. There should be more work done to understand why the particular volume percentage of graphene would result in a minimum COF in tribological tests.

Although the use of graphene in cutting fluid is advantageous for cutting the Inconel 718, however, the cost of production and cutting fluid waste management should be considered for mass production.

## 3.5. CONCLUSIONS

(1) The results of this chapter showed that that the use of graphene incorporating cutting fluid (GCF) during drilling process of Inconel 718 would reduce cutting torque and improve machined surface quality. The reasons for these improvements were investigated starting from tribological tests that determined the coefficient of friction (COF) between Inconel 718 and the tool material and showed the importance of formation of tribolayers in controlling the friction. The graphene incorporating tribolayers reduced the COF of Inconel 718 WC-Co system.

(2) The study of the tribological behaviour of Inconel 718 has proven to be a key factor in understanding the mechanism leading to the improvements in the drilling process. The lowest COF of the Inconel 718 / WC-Co tribosystem was 0.05 that was recorded for the boundary lubricated tests using GCF with $54\times10^{-5}$ wt.% graphene; at higher concentrations, an increasing COF trend was observed. Flooded drilling of Inconel 718 workpiece using WC-Co drills using GCF with this low percentage of graphene resulted in the formation of tribolayers with the same composition as those formed in tribological tests.

(3) Subsurface deformation of drilled surfaces of Inconel 718 were examined by cross-sectional optical microscopy that showed that both the depth of deformation zone and the subsurface strains were reduced compared to flooded drilling due to reduction of cutting temperatures when GCF drilling was used due to the formation of tribolayers. Consequently, adhesion between the interfaces was minimized; This resulted in a reduction in drilling torque by 20% and arithmetic mean height (Sa) of machined Inconel 718 surfaces by 50%.

(4) In summary, formation of tribolayer on the tool rake face, as a result of addition of GNP to the cutting fluid, reduced the COF in the tool-chip interface which resulted in reduction in cutting torque and temperature leading to low tool wear. Consequently, tooling retained its original shape, which in turn, contributed to more shearing action, rather than ploughing action, during the cutting process. Therefore, less microstructural deformation was observed when GCF was utilized and the produced surface roughness was reduced compared to flooded and dry cutting conditions.

## REFERENCES

[1] S. Bhowmick, M.Z.U. Khan, A. Banerji, M.J. Lukitsch, A.T. Alpas, Low friction and wear behaviour of non-hydrogenated DLC (a-C) sliding against fluorinated tetrahedral amorphous carbon (ta-C-F) at elevated temperatures, Applied Surface Science, 450 (2018) 274-283.

[2] M.Z.U. Khan, S. Bhowmick, M.J. Lukitsch, A.T. Alpas, Effect of test atmosphere on the tribological behaviour of the tetrahedral amorphous carbon (ta-C) and fluorinated ta-C (ta-C-F) coatings against steel, Surface and Coatings Technology, 332 (2017) 382-390.

[3] I. Hutchings, P. Shipway, Tribology: friction and wear of engineering materials, Butterworth-Heinemann, India, 2017.

[4] S. Bhowmick, A. Banerji, A.T. Alpas, Tribological behavior of Al–6.5%, –12%, –18.5% Si alloys during machining using CVD diamond and DLC coated tools, Surface and Coatings Technology, 284 (2015) 353-364.

[5] S. Bhowmick, A.T. Alpas, The role of diamond-like carbon coated drills on minimum quantity lubrication drilling of magnesium alloys, Surface and Coatings Technology, 205 (2011) 5302-5311.

[6] S. Bhowmick, A.T. Alpas, The performance of hydrogenated and non-hydrogenated diamond-like carbon tool coatings during the dry drilling of 319 Al, International Journal of Machine Tools and Manufacture, 48 (2008) 802-814.

[7] S. Bhowmick, M.J. Lukitsch, A.T. Alpas, Dry and minimum quantity lubrication drilling of cast magnesium alloy (AM60), International Journal of Machine Tools and Manufacture, 50 (2010) 444-457.

[8] S. Bhowmick, A.T. Alpas, Minimum quantity lubrication drilling of aluminium–silicon alloys in water using diamond-like carbon coated drills, International Journal of Machine Tools and Manufacture, 48 (2008) 1429-1443.

[9] S. Bhowmick, A.T. Alpas, The Performance of Diamond-Like Carbon Coated Drills in Thermally Assisted Drilling of Ti-6Al-4V, Journal of Manufacturing Science and Engineering, 135 (2013) 061019.

[10] E.M. Trent, P.K. Wright, Metal cutting, Butterworth-Heinemann, USA, 2000.

[11] M.C. Shaw, N.P. Suh, Discussion: "New Developments in the Theory of the Metal-Cutting Process: Part I. The Ploughing Process in Metal Cutting" (Albrecht, P., 1960, ASME J. Eng. Ind., 82, pp. 348–357), Journal of Engineering for Industry, 82 (1960) 357-357.

[12] D.A. Stephenson, J.S. Agapiou, Metal cutting theory and practice, CRC press, USA, 2016.

[13] A.C. Ferrari, J.C. Meyer, V. Scardaci, C. Casiraghi, M. Lazzeri, F. Mauri, S. Piscanec, D. Jiang, K.S. Novoselov, S. Roth, A.K. Geim, Raman spectrum of graphene and graphene layers, Physical Review Letters, 97 (2006) 187401.

[14] Z. Yang, S. Bhowmick, F.G. Sen, A. Banerji, A.T. Alpas, Roles of sliding-induced defects and dissociated water molecules on low friction of graphene, Scientific Reports, 8 (2018) 121.

[15] P. Lazar, E. Otyepková, P. Banáš, A. Fargašová, K. Šafářová, L. Lapčík, J. Pechoušek, R. Zbořil, M. Otyepka, The nature of high surface energy sites in graphene and graphite, Carbon, 73 (2014) 448-453.

[16] S. Bhowmick, G. Sun, A.T. Alpas, Low friction behaviour of boron carbide coatings (B4C) sliding against Ti–6Al–4V, Surface and Coatings Technology, 308 (2016) 316-327.

[17] J.-C. Rietsch, P. Brender, J. Dentzer, R. Gadiou, L. Vidal, C. Vix-Guterl, Evidence of water chemisorption during graphite friction under moist conditions, Carbon, 55 (2013) 90-97.

[18] S. Bhowmick, A. Banerji, A.T. Alpas, Friction reduction mechanisms in multilayer graphene sliding against hydrogenated diamond-like carbon, Carbon, 109 (2016) 795-804.

[19] P. Egberts, G.H. Han, X.Z. Liu, A.T.C. Johnson, R.W. Carpick, Frictional behavior of atomically thin sheets: hexagonal-shaped graphene islands grown on copper by chemical vapor deposition, ACS Nano, 8 (2014) 5010-5021.

# CHAPTER 4

# TURNING OF INCONEL 718 UNDER CRYOGENIC CONDITION IN COMPARISON TO FLOODED CUTTING: A MULTI-RESPONSE OPTIMIZATION APPROACH USING RSM

## 4.1. INTRODUCTION

The literature survey in Chapter 2 showed that cryogenic machining did not always improve the machinability of Inconel 718. This chapter uses response surface methodology (RSM) to address this question that which set of parameters should be used during the cryogenic machining to obtain an overall favorable performance which is comparable or even better the conventional flooded cutting.

Response surface methodology (RSM) is a statistical analysis method which is used for designing the experiments and optimizing the process parameters [1, 2]. It is well known that RSM can help to determine the set of machining parameters under new cutting conditions under which the tool wear is low and productivity is high. It has been employed for optimization of manufacturing processes of various alloys including superalloys [3-5]. The use of RSM could determine the set of machining parameters under which these

new cutting methods could provide high machining efficiency and low tool wear. Response Surface Methodology (RSM) is a powerful tool for systematic investigation of effect of process parameters on the response factors [6]. However, there are few works on optimization of parameters under cryogenic machining of superalloys. Most of the previous reports on cryogenic machining of Inconel 718 were based on experiments that were conducted at cutting parameters that were either randomly selected or were conceived to be the most important ones according to the researchers. Although the parameters used in these experiments were generally consistent with those recommended by the manufacturers, the selection of the cutting parameters used in the laboratory experiments can be improved using RSM. Thus, a systematic approach has been adopted in the current research to determine an optimum set of machining parameters [7]. Pusavec, et al. [8] have attempted to address this question by optimizing the cutting parameters using RSM. However, they compared cryogenic cooling with MQL and Cryo/MQL. According to the results, cryo-MQL showed the better results in terms of tool wear and cutting force. Speed of 42.3 m/min, feed of 0.05 mm/rev and depth of cut of 0.88 mm were found to be optimum cutting parameters. However, the lack of a systematic optimization of cryogenic cutting in machining of superalloys is still existing in the literature.

This chapter consists of two parts: in the first part, turning tests were done on Inconel 718 by spraying $LN_2$ to the cutting area at different cutting parameters (cutting speed, feed rate and depth of cut) and the resulted flank wear, cutting force and Ra surface roughness were compared with the data from flooded and dry cutting. The main objective of this part is to evaluate the effectiveness of application of $LN_2$ to the cutting area in increasing the machinability of Inconel 718 so that it will be comparable to conventional flooded cutting. In the second part,

statistical analysis and multi-response optimization using desirability function of RSM were employed in order to investigate the effect of cutting parameters on the response factors, namely flank wear, cutting force, Ra surface roughness and material removal rate (MRR) and determine the optimum cutting parameters in cutting using $LN_2$. For this purpose, cutting speed, feed rate and depth of cut were selected as cutting parameters each in five levels.

## 4.2. MATERIALS AND METHODS

The turning experiments were conducted on HAAS CNC Lathe using uncoated cemented carbide inserts and a tool holder with the ISO designation of DNGG150402 and PDJNR2020 manufactured by Sandvik Cormorant. The cross-sectional analysis of the cutting edge of the tool showed that the rake angle was +9°. To prevent ploughing action, and consequently, lower plastic deformation during the cutting process, tool radius was selected at the lower amount (0.2 mm) and the depth of cut was selected to be more than tool radius (Table 5) [9].

Hot rolled bars of Inconel 718 with the composition (wt.%) of Ni 53.84, Fe 18.02, Cr 17.98, (Nb+Ta) 5.39, Nb 5.38, Mo 2.92, Ti 0.96, Al 0.47, Co 0.35, Mn 0.09, Si 0.08, Cu 0.05, C 0.02, P 0.01, B 0.004, S 0.0003, Ta <0.01, Mg <0.01, and Ca <10 PPM were used as the workpiece material. The samples were solution treated with the cycle consisting of heating to 955°C and holding for 1 hour and then quenched in water. Figure 68 shows that the microstructure of the Inconel 718 consisted of a bimodal grain structure with small (19 ± 3 µm) and large grains (60 ± 10 µm) with hardness values of 290 HV and 243 HV.

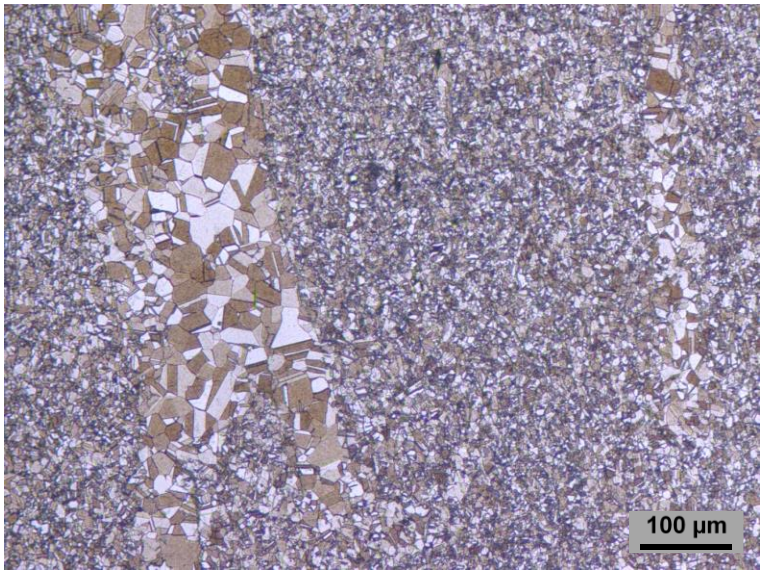


Figure 68 Microstructure of Inconel 718 workpiece.

Cryogenic cutting experiments were conducted using a rotating pump mounted to a flask containing $LN_2$ to spray the liquid nitrogen on the cutting edge of the tool and contact surface of the workpiece. The experimental setup and application of $LN_2$ to the cutting area is shown in Figure 69a, b. The flooded cutting experiments were conducted by applying synthetic cutting fluid.

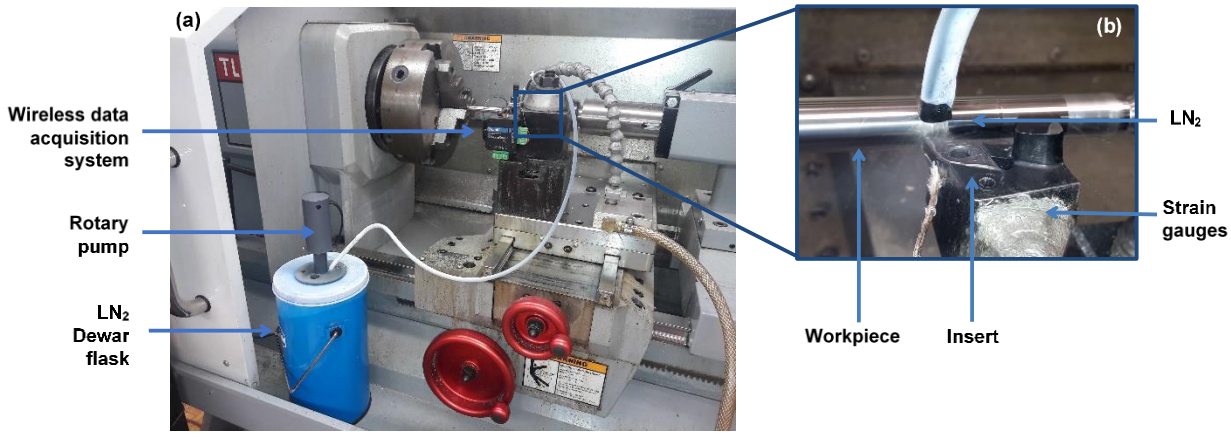


Figure 69 (a) Experimental setup showing the $LN_2$ Dewar flask, rotary pump and wireless data acquisition system, (b) application of $LN_2$ to the cutting area.

Linear strain gauges mounted on the tool holder were used to measure the cutting force in the tangential direction. The resistance and gauge factor of the strain gauges were 3.5 kΩ and 2.08 (Figure 70a). Since the changes in the resistance of strain gauges were very low (usually less than 0.5%) [9], a Wheatstone bridge configuration was used [10] (Figure 70b). A 'groove' or reduced gauge section with thinner cross sectional area was machined on the tool holder where the strain gauges were located for measuring elastic deflections during the machining process with high sensitivity. Figure 70c shows the modified tool holder and the strain gauges attached to the 'groove' on it. The calibration of the measurement set up was done before each cutting experiment by hanging of weights and a linear relationship between the applied load and the output voltage $V_{out}$ was observed as shown in Figure 70d. A data acquisition system including a wireless transmitter (V-Link 2.4 GHz Wireless Voltage Node 181) and an analog base receiver (MicroStrain Micro TxRx wireless base station W/ analog outputs) was used to measure the cutting forces during the turning process [11]. The real time streaming rate of this data acquisition system was up to 4 KHz and the analog latency while one channel was active was 2.5 ms.

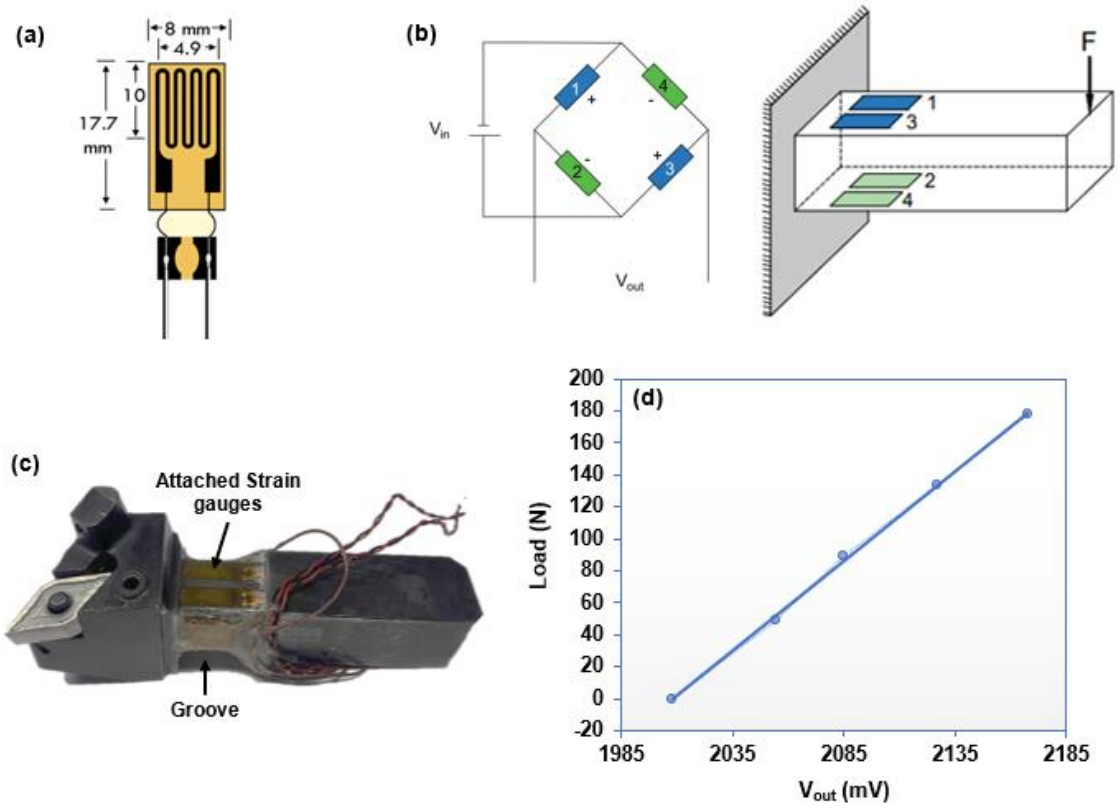


Figure 70 (a) Dimensions of linear strain gauge, (b) Wheatstone bridge configuration on the tool holder, (c) strain gauges attached on the tool holder, (d) calibration diagram, the obtained equation is $Load = 1.1209 \times V_{out} - 2251$.

Flank wear values were recorded according to ISO 3685:1993 standard by measuring the flank wear land in the B region [12] at least in 10 spots and the average values are reported. After each experiment, the insert was unmounted from the tool holder and its surface was examined using a ZEISS Axio Vert optical microscope at ×20 magnification which was fitted with a camera for measuring the obtained pictures using ImageJ software.

Vertical Scanning Interferometry (VSI) mode of WYKO NT 1100 optical profilometry system was utilized for 3D measurement of machined surface roughness values. The measurements were done at least in five area of the machined surface.

Turning experiments were designed following response surface methodology (RSM) using MINITAB software. Figure 71 shows the design of experiments cube plot. Axial, factorial and center points are illustrated in this figure along with the related test numbers. Axial points estimate the quadratic terms of the model. factorial portion of the design contribute to the estimation of the interaction terms in the second-order model. The center points provide an internal estimate of error and contribute toward the estimation of quadratic terms [13].

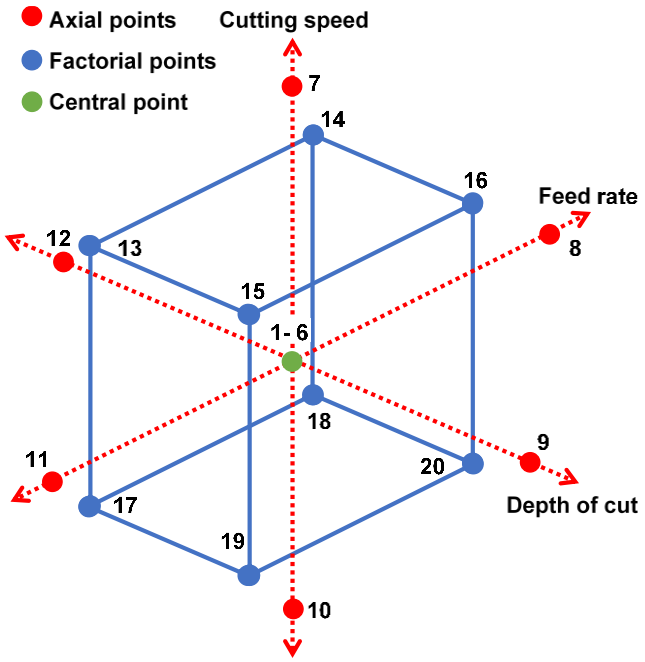


Figure 71 RSM design of experiments cube plot with the test numbers.

The results section is presented in two parts: in Section 4.3.1. a comparison of response parameters namely, flank wear, cutting force and Ra surface roughness on machining under cryogenic cutting condition with flooded and dry cutting are presented. The objective of this part was to investigate whether any improvement in machining of Inconel 718 by application of liquid nitrogen to the cutting area would acquire compared to flooded and dry machining.

The experiments in this part were carried out using parameters shown on the axial points (red points) in Figure 71. In section 4.3.3, statistical analyses and multi-response optimization of parameters using analysis of variance (ANOVA) and desirability function of RSM in machining under cryogenic condition are given. Statistical analyses were conducted using all the axial, factorial and central points of the RSM experimental design consisting of 20 experiments (Figure 71). Three cutting parameters (cutting speed, feed rate and depth of cut) each at five levels were considered as the process parameters (Table 5). Material removal rate (MRR), flank wear, cutting force and surface roughness were considered as the response factors.

## 4.3. RESULTS AND DISCUSSIONS

### 4.3.1. Comparison of Cryogenic Cutting with Flooded and Dry Machining

The objective of this part is to assess whether the application of liquid nitrogen to the cutting area during the turning experiments would improve the machinability of the Inconel 718 compared to the conventional flooded cutting. In addition, since cryogenic cutting is considered as a type of dry cutting method, the results were also compared to dry machining. For this purpose, seven experiments were done according to the axial points of the experimental design shown in Figure 71 under cryogenic, flooded and dry conditions and the results of flank wear, cutting force and Ra surface roughness were compared to evaluate the performance of the cryogenic cutting (Table 4).

Table 4 Experimental results of flank wear, cutting force and Ra surface roughness under different cutting conditions.

| Cutting Parameters | | | Cryogenic | | | Flooded | | | Dry | | |
|---|---|---|---|---|---|---|---|---|---|---|---|
| $V_c$ | f | $a_p$ | $VB_B$ (µm) | $F_c$ (N) | $Ra$ (µm) | $VB_B$ (µm) | $F_c$ (N) | $Ra$ (µm) | $VB_B$ (µm) | $F_c$ (N) | $Ra$ (µm) |
| 120 | 0.05 | 0.5 | 160 | 122 | 0.920 | 154 | 104 | 0.872 | 201 | 99 | 0.764 |
| 70 | 0.09 | 0.5 | 67 | 140 | 1.405 | 71 | 142 | 1.270 | 102 | 133 | 0.548 |
| 70 | 0.05 | 0.7 | 60 | 120 | 1.775 | 69 | 124 | 0.576 | 103 | 121 | 0.789 |
| 20 | 0.05 | 0.5 | 53 | 108 | 0.675 | 51 | 117 | 0.651 | 47 | 97 | 0.660 |
| 70 | 0.01 | 0.5 | 77 | 19 | 1.656 | 128 | 40 | 0.317 | 185 | 44 | 0.693 |
| 70 | 0.05 | 0.3 | 23 | 40 | 0.534 | 76 | 67 | 0.431 | 101 | 52 | 0.577 |

### 4.3.2. Effect of Cutting Parameters on Flank Wear Under Different Cutting Conditions

Figure 72a-c shows the variation of average flank wear values with cutting speed, feed rate and depth of cut for cryogenic, in comparison with flooded and dry cutting conditions. Flank wear values were recorded according to ISO 3685:1993 standard by measuring the flank wear land in the region B [12] at least in 10 spots and the average values are reported. The variation of flank wear values with cutting speed, feed rate and depth of cut were similar under all the cutting conditions. Flank wear increased with the increase in cutting speed as shown in Figure 72a. By increasing feed rate from low (0.01 mm/rev) to medium (0.05 mm/rev) values, flank wear decreased. However, at a higher feed rate of 0.09 mm/rev, flank wear did not change significantly compared to the one at 0.05 mm/rev (Figure 72b). Measured values of flank wear were almost constant for all the cutting depth values (Figure 72c). Flank wear values were almost the same for cryogenic and flooded conditions at all cutting parameters while dry cutting resulted in higher flank wear at all the cutting parameters. Small standard deviations about the mean values of flank wear generated during flooded and cryogenic cutting revealed high uniformity of flank wear in comparison to dry cutting condition [14].

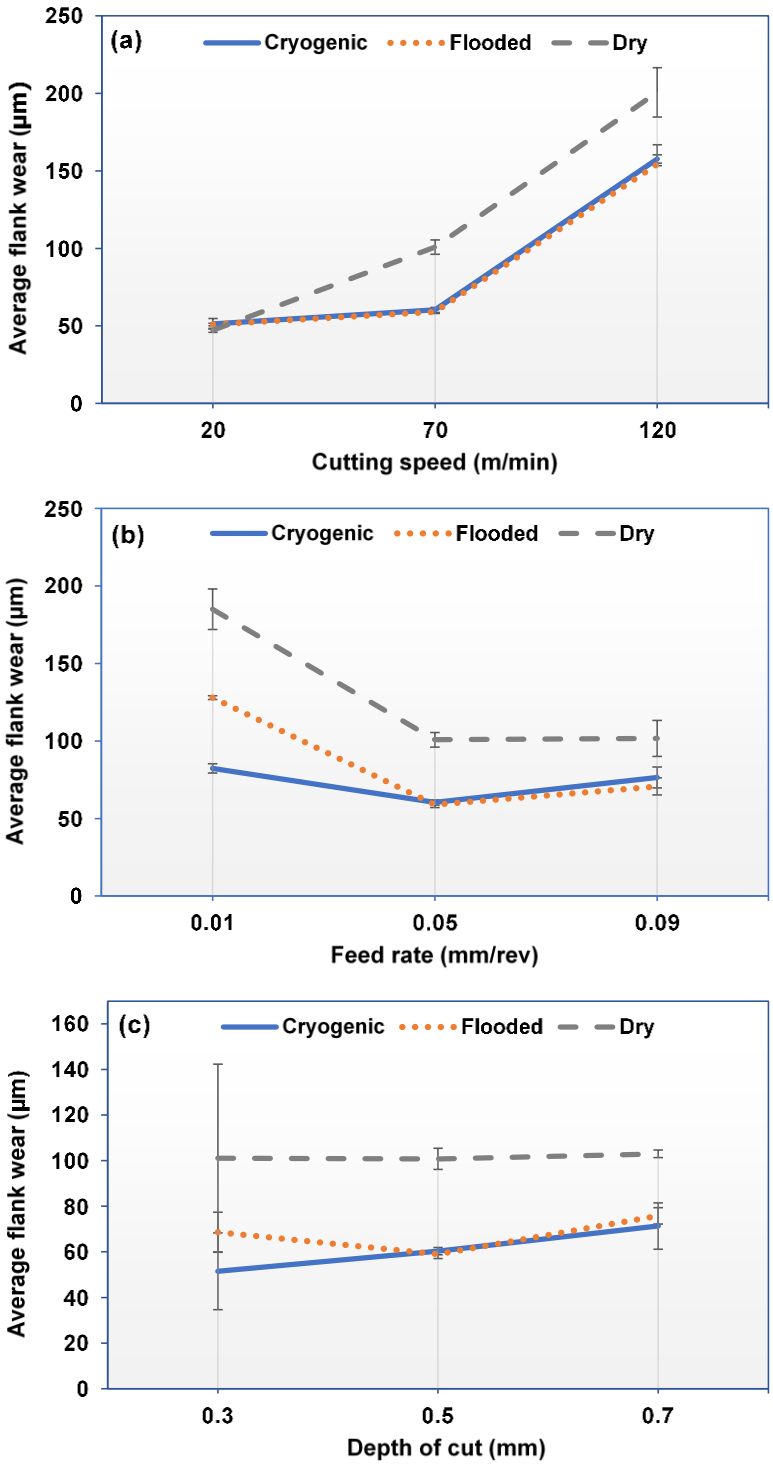


Figure 72 Average flank wear values at different (a) cutting speeds (f = 0.05 mm/rev, $a_p$ = 0.5 mm), (b) feed rates ($V_c$ = 70 m/min, $a_p$ = 0.5 mm) and (c) depth of cuts ($V_c$ = 70 m/min, f = 0.05 mm/rev) under cryogenic, flooded and dry conditions.

Tool wear types under cryogenic, flooded and dry conditions were investigated using scanning electron microscopy (SEM) (Figure 73-Figure 75). It was observed that under cryogenic condition, abrasion of the flank face of the tool and adhesion of Inconel 718 and formation of built-up edges (BUE) were the wear mechanisms for almost all the set of parameters that machining tests were conducted. Typical adhesion of Inconel 718 on the flank face of the cutting tool is shown in Figure 73a-d. Adhered layer of Inconel 718 material was observed at low cutting speed of 20 m/min (Figure 73a). At high feed rate of 0.09 mm/rev (Figure 73b) BUE was formed in the depth of cut region of the tool. At depth of cut values of 0.3 mm (Figure 73c) and 0.7 mm (Figure 73d), BUE and abrasion along with adhesion were observed around the tool nose. This shows that abrasion occurred before adhesion of the Inconel 718 material on the cutting edge of the tool. Chipping was another wear type that was observed under cryogenic cutting at low feed rate of 0.01 mm/rev. Figure 73e shows the chipping on the cutting edge from the end cutting edge view. Wear mechanism changed at the 120 m/min cutting speed to mainly abrasion of the flank face of the cutting tool (Figure 73f).

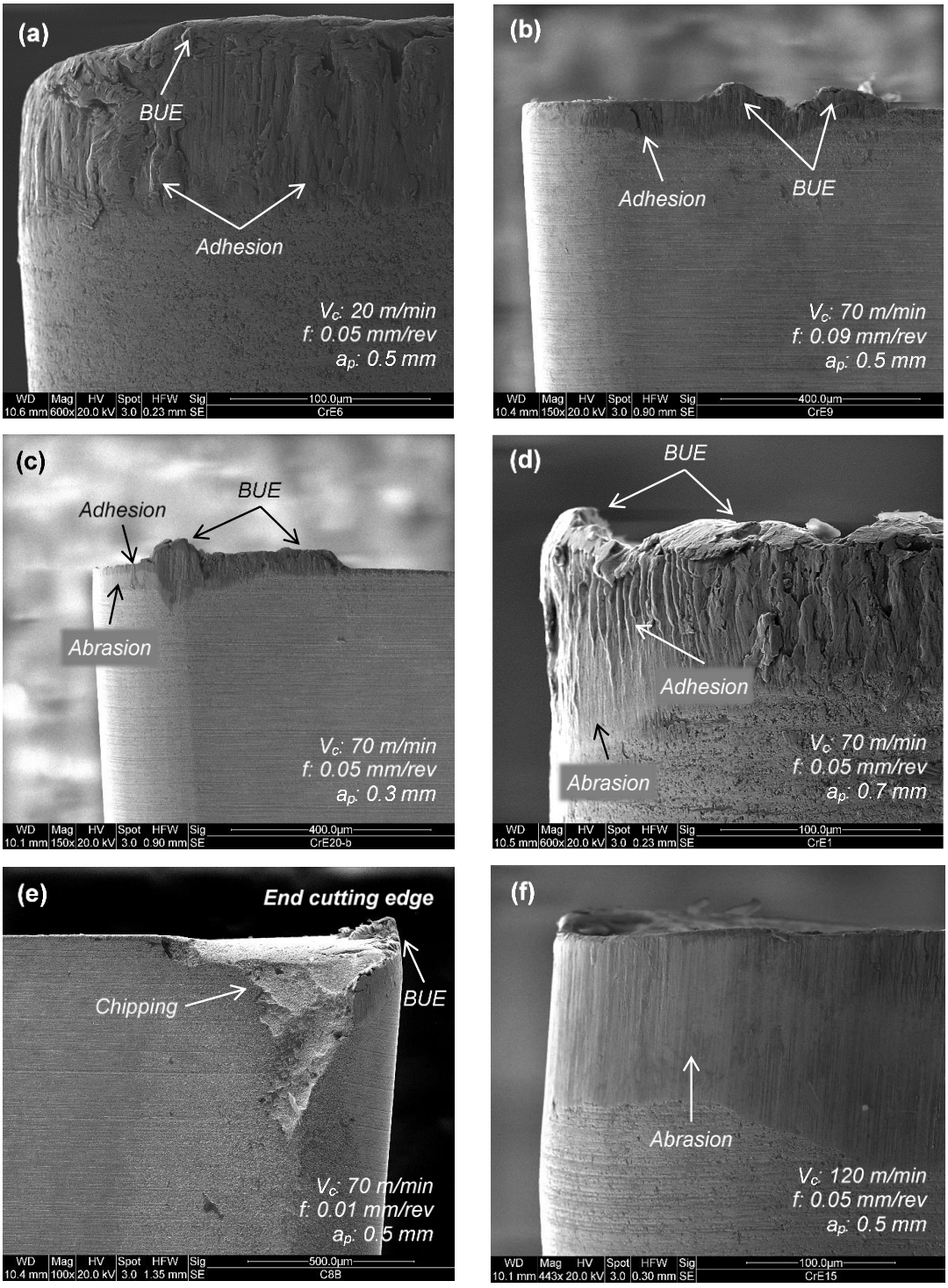


Figure 73 Typical tool wear types observed in turning of Inconel 718 under cryogenic condition at (a) $V_c$: 20 m/min, f: 0.05 mm/rev, $a_p$: 0.5 mm. (b) $V_c$: 70 m/min, f: 0.09 mm/rev, $a_p$: 0.5 mm. (c) $V_c$: 70 m/min, f: 0.05 mm/rev, $a_p$: 0.3 mm. (d) $V_c$: 70 m/min, f: 0.05 mm/rev, ap: 0.7 mm. (e) $V_c$: 70 m/min, f: 0.01 mm/rev, $a_p$: 0.5 mm. (f) $V_c$: 120 m/min, f: 0.05 mm/rev, $a_p$: 0.5 mm.

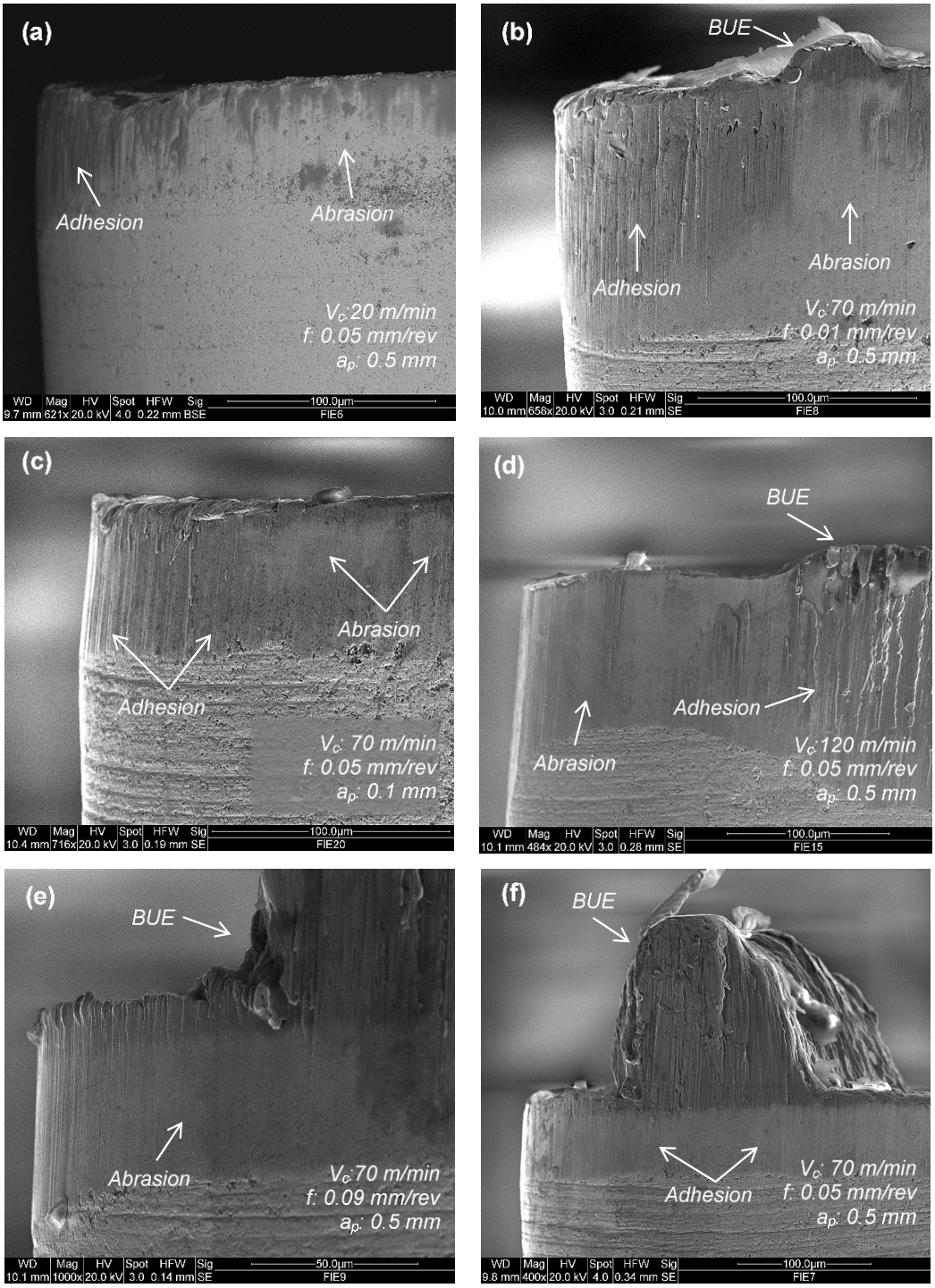


Figure 74 Typical tool wear types observed in turning of Inconel 718 under Flooded condition at (a) Vc:20 m/min, f: 0.05 mm/rev, $a_p$: 0.5 mm. (b) $V_c$:70 m/min, f: 0.01 mm/rev, $a_p$: 0.5 mm. (c) $V_c$: 70 m/min, f: 0.05 mm/rev, $a_p$: 0.1 mm. (d) $V_c$:120 m/min, f: 0.05 mm/rev, $a_p$: 0.5 mm. (e) $V_c$:70 m/min, f: 0.09 mm/rev, $a_p$: 0.5 mm. (f) $V_c$: 70 m/min, f: 0.05 mm/rev, $a_p$: 0.5 mm.

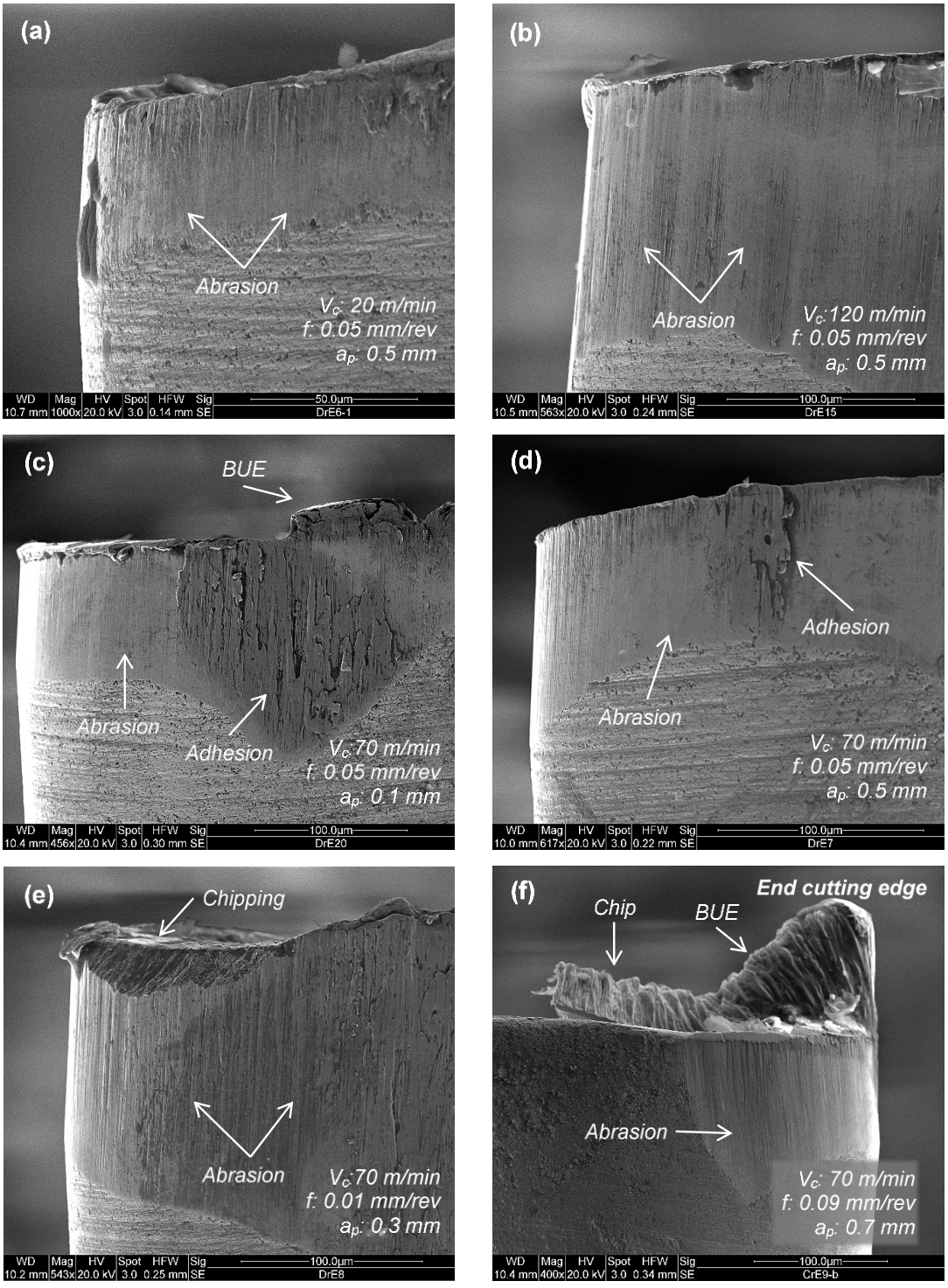


Figure 75 Typical tool wear types observed in turning of Inconel 718 under Dry condition at (a) $V_c$: 20 m/min, f: 0.05 mm/rev, $a_p$: 0.5 mm, (b) $V_c$:120 m/min, f: 0.05 mm/rev, $a_p$: 0.5 mm, (c) $V_c$:70 m/min, f: 0.05 mm/rev, $a_p$: 0.1 mm, (d) $V_c$: 70 m/min, f: 0.05 mm/rev, $a_p$: 0.5 mm, (e) $V_c$:70 m/min, f: 0.01 mm/rev, $a_p$: 0.3 mm, (f) $V_c$: 70 m/min, f: 0.09 mm/rev, $a_p$: 0.7 mm.

Abrasion and adhesion both were observed on the cutting edge after machining under flooded cutting (Figure 74a-f). At low cutting speed of 20 m/min, feed rate of 0.01 mm/rev and depth of cut of 0.1 mm, abrasion was the dominant wear mechanism (Figure 74a-c), although slight adhered layers of Inconel 718 material along with BUE was also observable. Increase in cutting speed to 120 m/min (Figure 74d), feed rate to 0.09 mm/rev (Figure 74e) and depth of cut to 0.5 mm (Figure 74f) led to increase the adhered layer and BUE on the cutting tool. However, abrasion was still an important wear mechanism on flank wear of the tool at these parameters.

In dry cutting, abrasion was the most significant wear mechanism on flank wear of the cutting tool (Figure 75a-f). Formation of adhered layer and BUE was lower compared to flooded cutting. At 20 m/min (Figure 75a) and 120 m/min (Figure 75b) cutting speeds, abrasion was the dominant wear mechanism. At 0.1 mm (Figure 75c) and 0.5 mm (Figure 75d) depth of cuts, adhesion and BUE were observed on the flank face of the tool. Chipping of the tool nose was occurred at low feed rate of 0.01 mm/rev and low depth of cut of 0.3 mm (Figure 75e). At high feed rate of 0.09 mm/rev and high depth of cut of 0.7 mm, adhesion of Inconel 718 material was significant and BUE was formed on the cutting tool (Figure 75f). Zhuang, et al. [15] reported similar results in which high adhesion and built-up edge (BUE) were observed in cryogenic cutting and high abrasion in dry cutting of Inconel 718 when comparing the results with plasma-enhanced machining (PEM). Moreover, Pusavec, et al. [8] observed catastrophic failure on the cutting edge during the cryogenic cutting of Inconel 718 when comparing it with dry, MQL and CryoMQL conditions.

*4.3.2.1. Effect of cutting parameters on cutting force under different cutting conditions*

Figure 76a-c shows the variation of cutting force values in terms of cutting parameters under cryogenic, flooded and dry conditions. Cutting force was the lowest at the medium cutting speed (70 m/min) under all cutting conditions. While cryogenic cutting resulted in lower cutting force in low and medium cutting speed compared to flooded cutting, at the high cutting speed, cutting force was higher under cryogenic cooling. This can be attributed to change in wear mechanism under cryogenic cutting (Figure 73f). Cutting force was measured to be low under dry cutting which was because of sharp tool edge and the small length of cutting whereby the effect of high tool wear was not taken effect yet. Similar results were obtained in previous works; cutting force and surface roughness were higher in wet machining than dry cutting in turning Inconel 718 done by Devillez, et al. [16]. Tebaldo, et al. [14] reported a negligible variation in cutting forces among the different cooling techniques (dry, MQL, MQC and wet). They also showed higher cutting force in flooded than cryogenic and MQL.

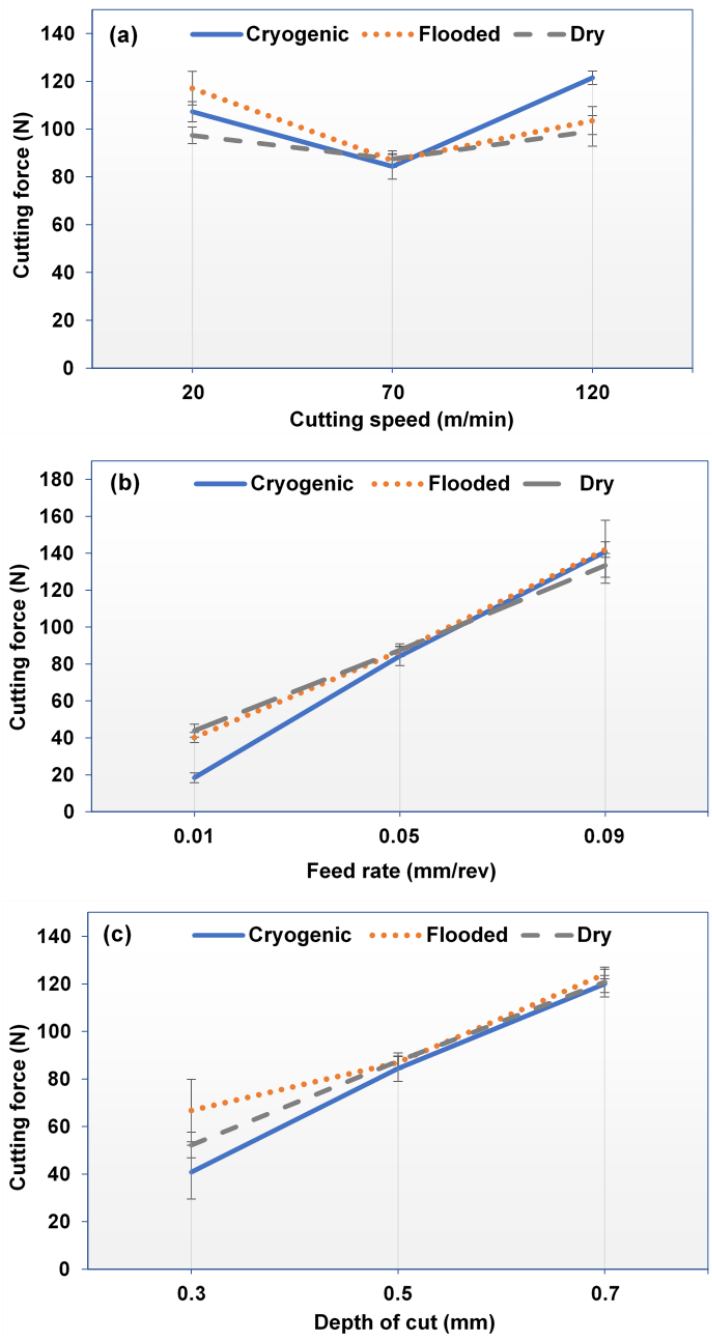


Figure 76 Cutting force values at different (a) cutting speeds (f = 0.05 mm/rev, $a_p$ = 0.5 mm), (b) feed rates ($V_c$ = 70 m/min, $a_p$ = 0.5 mm) and (c) depth of cuts ($V_c$ = 70 m/min, f = 0.05 mm/rev) under cryogenic, flooded and dry conditions.

With respect to the effect of feed rate and depth of cut on the cutting force, it was observed that by increasing feed rate and depth of cut, cutting force had an increasing trend (Figure 76b, c). At low depth of cut and feed rate, cryogenic cutting resulted in lower cutting force than flooded and dry cutting whereas at medium and high parameters the cutting force values were almost the same under all the cutting conditions.

*4.3.2.2. Effect of cutting parameters on Ra surface roughness under different cutting conditions*

Figure 77a-c shows variations of Ra surface roughness with cutting parameters (cutting speed, feed rate and depth of cut) under different cutting conditions. There was a minimum value of Ra at medium cutting speed of 70 m/min for all the cutting conditions (Figure 77a). This is attributed to the low cutting force at this parameter (Figure 76a). Generally, flooded cutting resulted in lower surface roughness than cryogenic cutting at all the cutting conditions. Similar results were reported by Tebaldo, et al. [14]. They compared MQC with dry and flooded cutting and reported that the lowest magnitude of surface roughness when flood turning was obtained compared to cryogenic cutting. Figure 77b-c showed that high values of Ra were observed at low feed rate (0.01 mm/rev) and high depth of cut (0.7 mm) when cutting under cryogenic condition while flooded cutting resulted in much lower Ra values at these parameters. Dry cutting resulted to lower roughness values compared to cryogenic cutting at all the cutting parameters. Similar results were reported by Pusavec, et al. [8] in turning of Inconel 718. They reported high Ra roughness values under cryogenic cutting in comparison to dry cutting at all the cutting speeds.

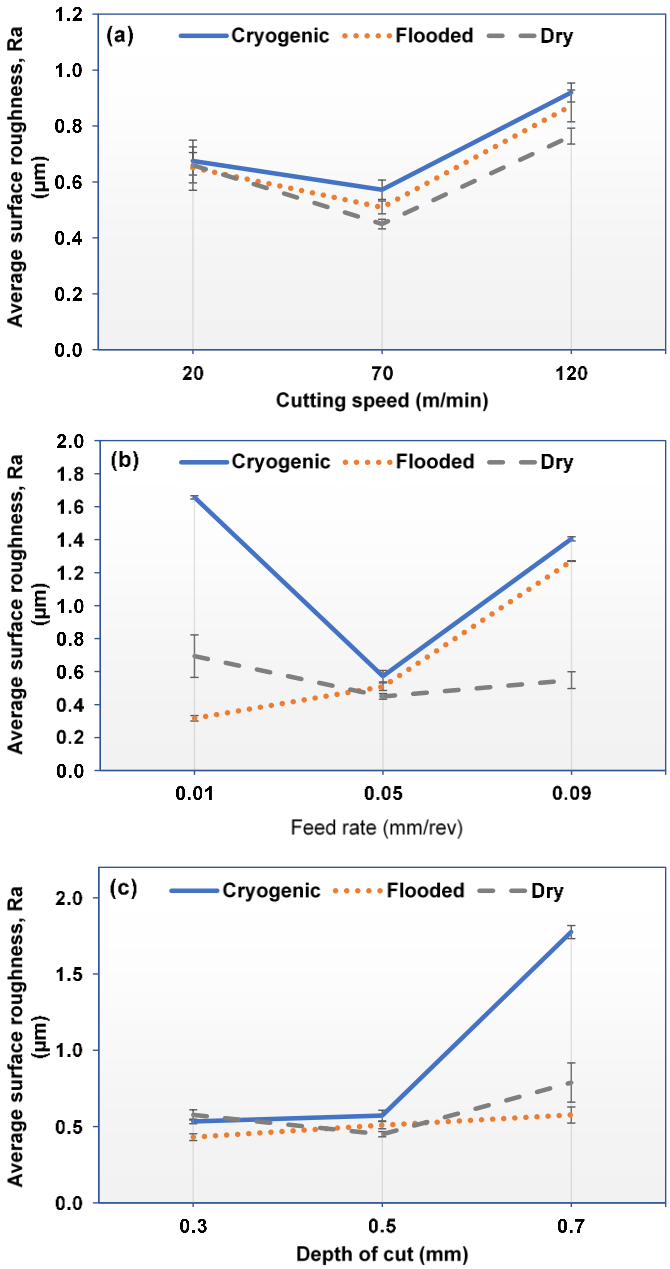


Figure 77 Average Ra surface roughness values at different (a) cutting speeds (f = 0.05 mm/rev, $a_p$ = 0.5 mm), (b) feed rates ($V_c$ = 70 m/min, $a_p$ = 0.5 mm) and (c) depth of cuts ($V_c$ = 70 m/min, f = 0.05 mm/rev) under cryogenic, flooded and dry conditions.

Produced workpiece surface quality under cryogenic and flooded cutting conditions were closely investigated by SEM (Figure 78a, b). Figure 78a shows surface quality produced under

cryogenic condition at different feed rates. At low feed rate (0.01 mm/rev) cavity and high built-up layer (BUL) resulted in high roughness value (1.7 µm) and poor surface quality. Side flow and BUL were observed at high feed rate (0.09 mm/rev) in lesser extent than 0.01 mm/rev, but the roughness value was still high (1.4 µm). Side flow is the result of high pressure on the workpiece material left behind on the on the secondary cutting edge of the tool [10]. It has been shown that side flow can be zero for brittle materials [17]. At the medium feed rate (0.05 mm/rev), however, the surface defects such as groove and BUL were less prominent and the roughness value dropped to 0.6 µm, resulting in good surface quality, which was comparable to the one produced under flooded cutting as shown in Figure 78b. Under flooded cutting, unlike the cryogenic cutting, the obtained quality of the machined surfaces was consistent whereby there were no dramatic changes in formation of surface defects at different cutting parameters. However, the surface roughness increased with feed rate (Figure 78b). Similar consistency in the produced surface quality was observed at different depth of cut values (Figure 77c). Therefore, surface quality and formation of surface defects under cryogenic condition was highly dependent on the cutting parameters at which the machining process was carried out.

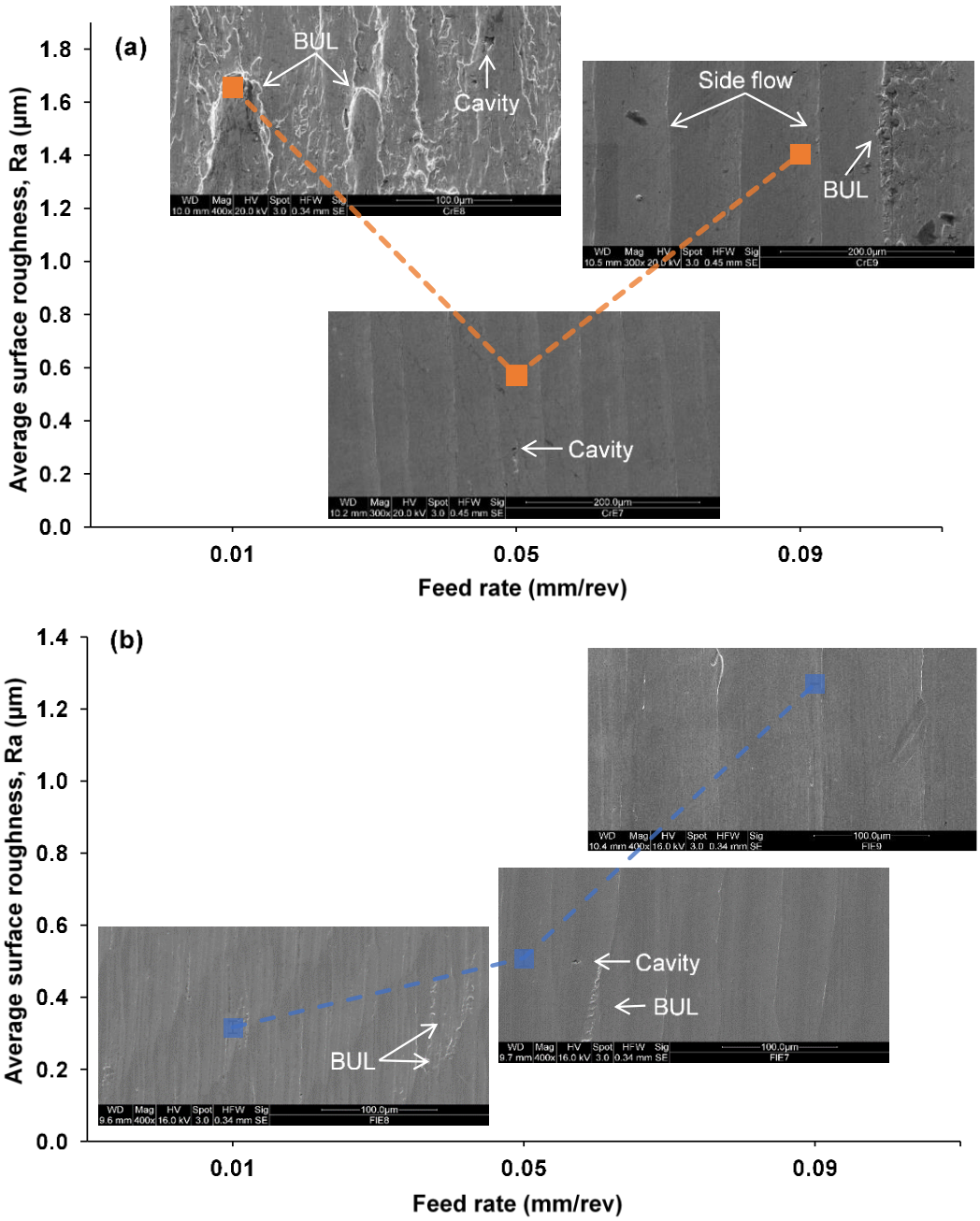


Figure 78 Variation of surface quality with feed rate ($V_c$ = 70 m/min, $a_p$ = 0.5 mm) under (a) cryogenic, (b) flooded cutting conditions.

### 4.3.3. Statistical Analysis and Optimization of Cutting Parameters in Cutting Inconel 718 Under Cryogenic Condition Using RSM

Experimental results in section 4.3.1 indicated that there can be a set of parameters in which machinability of Inconel 718 in terms of tool wear, cutting force and surface quality can be improved without using flooded machining. In order to find the optimum cutting parameters under cryogenic cutting condition response surface methodology (RSM) was utilized as stated previously. Cutting speed, feed rate and depth of cut were selected as the process parameters and flank wear, cutting force, Ra surface roughness and material removal rate (MRR) were considered as the response parameters for multi-response optimization process using desirability function. Material removal rate (MRR) is defined as $V_c \times f \times a_p$. Table 5 presents three cutting parameters, namely cutting speed, feed rate and depth of cut each at five levels which were considered for RSM statistical analysis. Experimental results of machining of Inconel 718 under cryogenic condition according to RSM experimental design arrangement are summarized in

Table 6. The effect of cutting parameters on the response parameters were investigated by 3D surface graphs and statistical analyses such as ANOVA so as to determine the most significant parameters on each response factor.

Table 5 Cutting parameters and their levels.

| Cutting Parameters | Level 1 | Level 2 | Level 3 | Level 4 | Level 5 |
|---|---|---|---|---|---|
| Cutting speed, $V_c$ (m/min) | 20 | 45 | 70 | 95 | 120 |
| Feed rate, $f$ (mm/rev) | 0.05 | 0.10 | 0.15 | 0.20 | 0.25 |
| Depth of cut, $a_p$ (mm) | 0.3 | 0.4 | 0.5 | 0.6 | 0.7 |

Table 6 Experimental results after machining of Inconel 718 under cryogenic condition.

| Test No. | Point Type * | Cutting parameters | | | Response Parameters | | | |
|---|---|---|---|---|---|---|---|---|
| | | Speed, $V_c$ (m/min) | Feed, $f$ (mm/rev) | Depth of cut, $a_p$ (mm) | Flank wear, $VB_B$ (µm) | Cutting force, $F_c$ (N) | Surface roughness, Ra (µm) | $MRR$ (cm3/min) |
| 1 | C | 70 | 0.05 | 0.5 | 62 | 86 | 0.534 | 1.75 |
| 2 | C | 70 | 0.05 | 0.5 | 63 | 89 | 0.504 | 1.75 |
| 3 | C | 70 | 0.05 | 0.5 | 59 | 82 | 0.587 | 1.75 |
| 4 | C | 70 | 0.05 | 0.5 | 55 | 80 | 0.490 | 1.75 |
| 5 | C | 70 | 0.05 | 0.5 | 65 | 83 | 0.620 | 1.75 |
| 6 | C | 70 | 0.05 | 0.5 | 58 | 85 | 0.572 | 1.75 |
| 7 | A | 120 | 0.05 | 0.5 | 160 | 122 | 0.920 | 3.00 |
| 8 | A | 70 | 0.09 | 0.5 | 67 | 140 | 1.405 | 3.15 |
| 9 | A | 70 | 0.05 | 0.7 | 60 | 120 | 1.775 | 2.45 |
| 10 | A | 20 | 0.05 | 0.5 | 53 | 108 | 0.675 | 0.5 |
| 11 | A | 70 | 0.01 | 0.5 | 77 | 19 | 1.656 | 0.35 |
| 12 | A | 70 | 0.05 | 0.3 | 23 | 40 | 0.534 | 1.05 |
| 13 | F | 95 | 0.03 | 0.6 | 125 | 104 | 0.536 | 1.71 |
| 14 | F | 95 | 0.07 | 0.6 | 97 | 153 | 1.146 | 3.99 |
| 15 | F | 95 | 0.03 | 0.4 | 100 | 67 | 0.363 | 1.14 |
| 16 | F | 95 | 0.07 | 0.4 | 103 | 104 | 0.658 | 2.66 |
| 17 | F | 45 | 0.03 | 0.6 | 54 | 106 | 0.851 | 0.81 |
| 18 | F | 45 | 0.07 | 0.6 | 58 | 184 | 1.376 | 1.89 |
| 19 | F | 45 | 0.03 | 0.4 | 54 | 66 | 0.961 | 0.54 |
| 20 | F | 45 | 0.07 | 0.4 | 27 | 110 | 0.948 | 1.26 |

* C: Central point, A: Axial point, F: Factorial point

*4.3.3.1. Effect of cutting parameters on flank wear*

The experimental data were used for developing a regression model in terms of flank wear which is presented in Eq. 15.

$$VB_B = -18.4 - 1.68\,V_c - 1173\,f + 456\,a_p + 0.02\,{V_c}^2 + 9602\,f^2 - 378\,{a_p}^2 \quad (15)$$

Where $VB_B$ is the average flank wear in the region B (see Section 4.2), $V_c$ is cutting speed, $f$ is feed rate and $a_p$ is depth of cut. Coefficient of determination, $R^2$ of the model was calculated as

95.68% which confirmed the effectiveness of the model. Figure 79a, b shows the normal probability plot of the residuals for flank wear in which the data closely fall on the straight line indicating that the errors are distributed normally [13]. This also can be seen in Figure 79b in which histogram of residuals for flank wear shows distribution around the zero value.

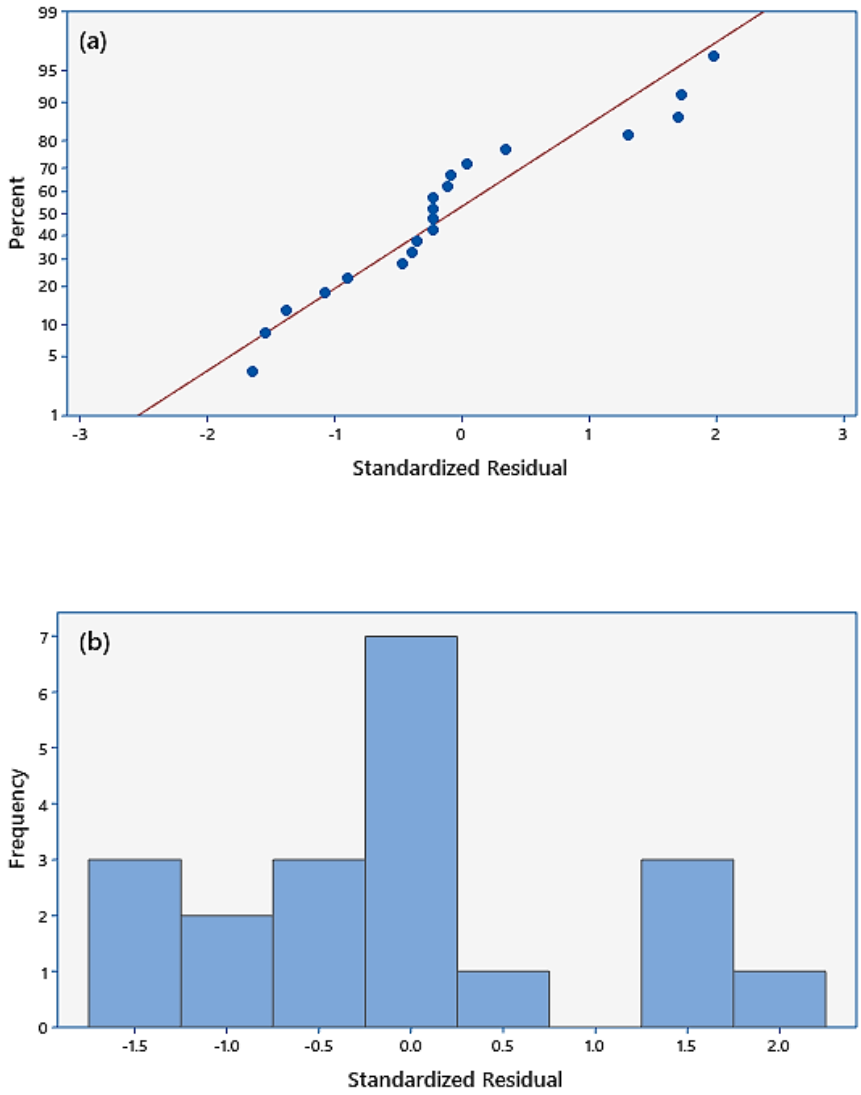


Figure 79 (a) Normal probability plot, (b) histogram of standardized residual for flank wear.

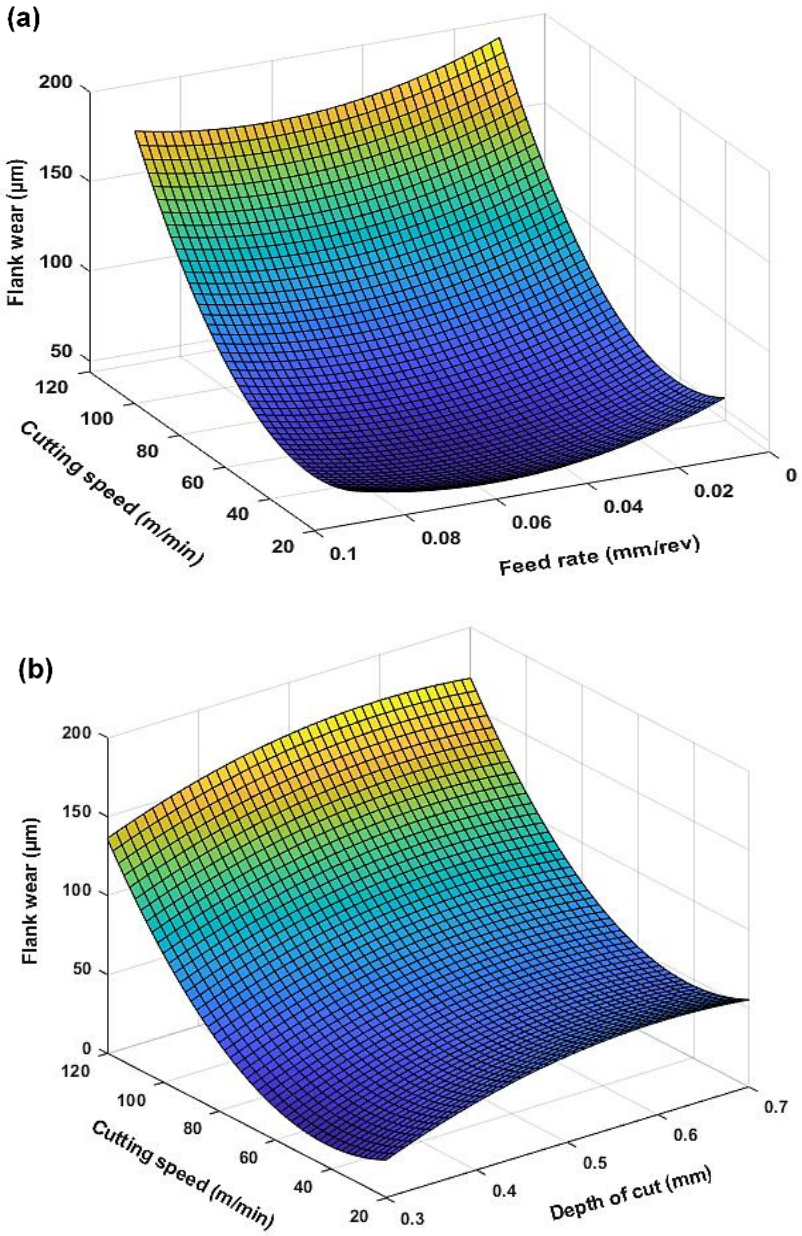


Figure 80 3D surface graph for interaction effect of (a) cutting speed and depth of cut and (b) feed rate and cutting speed on flank wear.

Analysis of variance (ANOVA) for flank wear is presented in Table 7. In this table, *DF* is degree of freedom which is one for each parameter, SS is sum of squares which is a statistical technique to determine the variation of data point compared to the line of best fit, MS is mean

square which is defined as SS/DF. $SS_E$ and $MS_E$ are are called the sum of squares and mean square due to error which are determined within each group. $SS_E$ is defined by:

$$SS_E = \sum_{i=1}^{a} \sum_{j=1}^{n} (y_{ij} - \bar{y}_{i.})^2 \quad (16)$$

Where $y_{ij}$ is *ij*th observation, $\bar{y}_{i.}$ is the average of the observations under *i*th treatment. F-value is calculated as $MS/MS_E$ which is used to determine whether the test is statistically significant, meaning the results are meaningful and not gained by random [18]. For this purpose, probability value (P-value) is calculated. P-value is defined as the smallest level of significance ($\alpha$=0.05) that would lead to rejection of the null hypothesis which is that the average value of the dependent variable is the same for all groups [13]. In other words, when the P-value of a variable is less than 0.05, it can be stated with the 95% of confidence that the variable is statistically significant and when the P-value of a variable is between 0.5 and 0.1, the variable is considered marginally significant [19].

Table 7 shows that all the parameters had statistically significant effect on flank wear as the P-values are less than 0.05. Cutting speed with the P-value of 0.001 for Vc and 0.000 for $V_c{}^2$ was a highly significant variable. In addition, F-values of cutting speed showed that it was the most influential parameter on flank wear.

Table 7 Results of ANOVA for flank wear.

| Source | DF | SS | MS (SS/DF) | F-Value ($MS/MS_E$) | P-Value ($\alpha$=0.05) |
|---|---|---|---|---|---|
| Model | 6 | 18832.6 | 3138.76 | 48.03 | 0.000 |
| $V_c$ | 1 | 1342.6 | 1342.57 | 20.54 | 0.001 |
| $f$ | 1 | 520.5 | 520.54 | 7.96 | 0.014 |
| $a_p$ | 1 | 514.5 | 514.52 | 7.87 | 0.015 |
| ${V_c}^2$ | 1 | 3907.2 | 3907.17 | 59.78 | 0.000 |
| $f^2$ | 1 | 370.9 | 370.92 | 5.68 | 0.033 |
| ${a_p}^2$ | 1 | 360.0 | 360.03 | 5.51 | 0.035 |
| Error | 13 | 849.6 | 65.35 | | |
| Total | 19 | 7,864.7 | | | |

The effect of cutting parameters on the flank wear can be observed in Figure 80. It is observed that flank wear increased from 45 µm at 40 m/min to 190 µm at 120 m/min cutting speed (Figure 80a). Flank wear increased with depth of cut; however, the rate of increase decreased as the depth of cut values increased (Figure 80b).

*4.3.3.2. Effect of cutting parameters on cutting force*

Regression model developed for the cutting force ($F_c$) is presented in Eq. 13. $R^2$ value of the model was calculated as 88.17% which shows the adequacy of the model.

$$F_c = -3.5 - 2.100\,V_c + 1310\,f + 174\,a_p + 0.01482\,{V_c}^2 + 966\,f^2 + 51\,{a_p}^2 \qquad (17)$$

Normal probability plot of the residuals for cutting force are shown in Figure 81a. The fact that the data fall on the straight line shows that the errors are distributed normally. Histogram of standardized residual depicted in Figure 81b shows that the residuals were distributed around zero. ANOVA for cutting force is given in Table 8. P-value analysis for the cutting parameters showed that cutting speed (P-value= 0.01) was the only statistically significant parameter for cutting force. Feed rate (P-value= 0.12) had a marginally significant effect on cutting force.

Table 8 Results of ANOVA for cutting force.

| Source | DF | SS | MS (SS/DF) | F-Value (MS/MSE) | P-Value (α=0.05) |
|---|---|---|---|---|---|
| Model | 6 | 23025.0 | 3837.50 | 16.13 | 0.000 |
| $V_c$ | 1 | 2103.5 | 2103.46 | 8.84 | 0.011 |
| $f$ | 1 | 649.2 | 649.20 | 2.73 | 0.122 |
| $a_p$ | 1 | 74.8 | 74.83 | 0.31 | 0.584 |
| ${V_c}^2$ | 1 | 2156.6 | 2156.57 | 9.06 | 0.010 |
| $f^2$ | 1 | 3.8 | 3.75 | 0.02 | 0.902 |
| ${a_p}^2$ | 1 | 6.6 | 6.57 | 0.03 | 0.871 |
| Error | 13 | 3092.8 | 237.91 | | |
| Total | 19 | 26117.8 | | | |

3D surface graph for interaction effect of the cutting parameters are shown in Figure 82a, b. Increase in cutting speed first reduced the cutting force and then increased it. Increase in feed rate and depth of cut resulted in rise of the cutting force (Figure 82b).

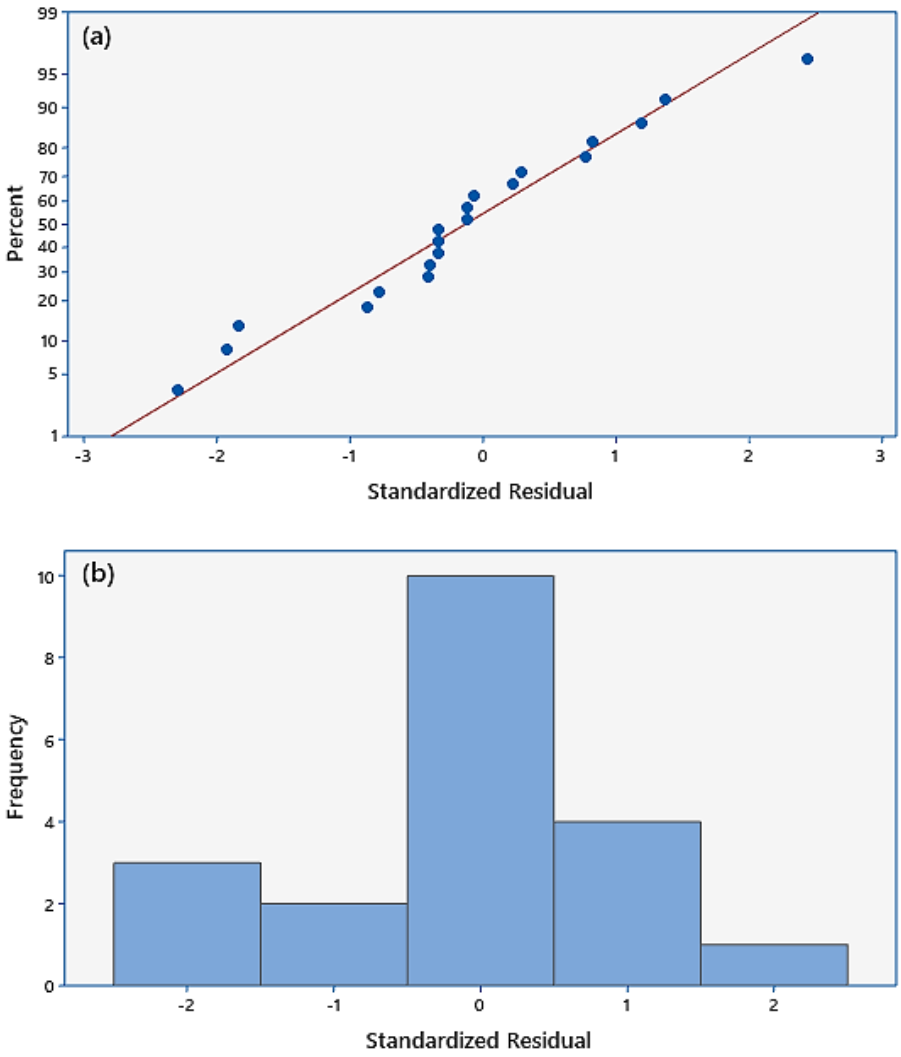


Figure 81 (a) Normal probability plot, (b) histogram of standardized residual for cutting force.

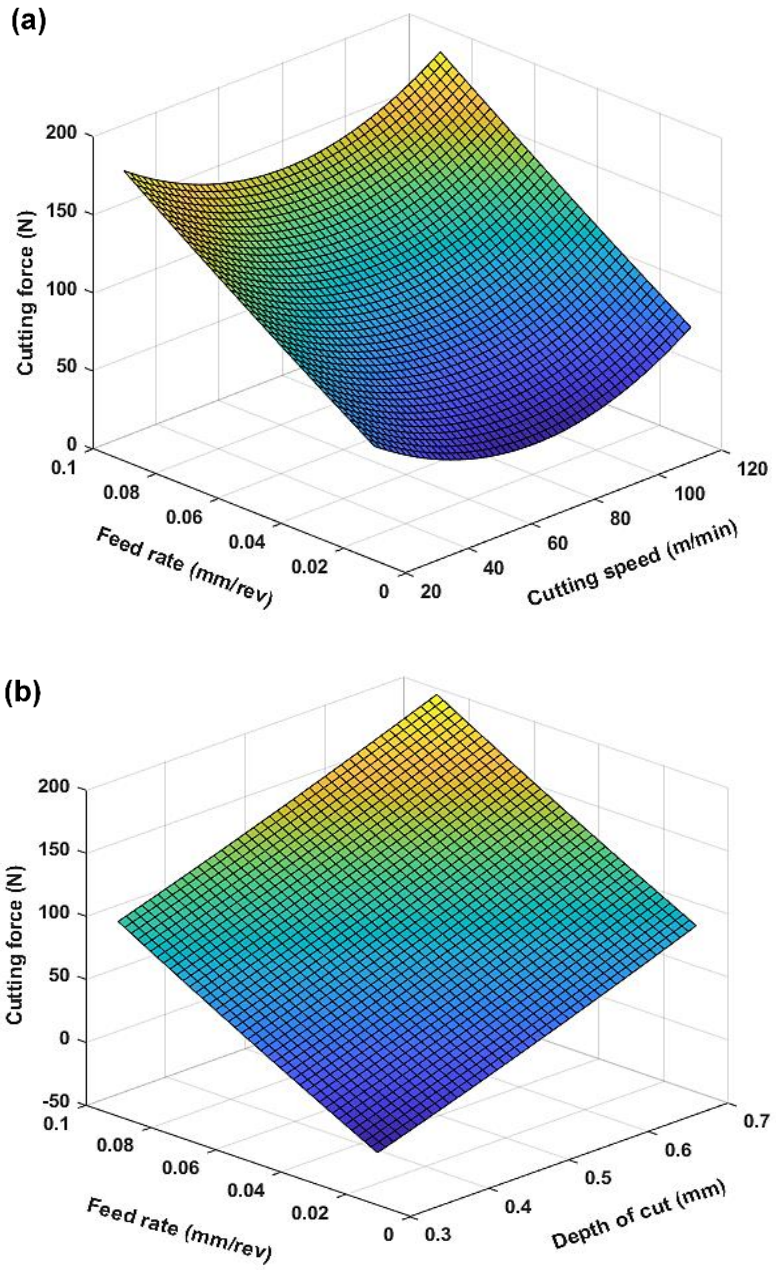


Figure 82 3D surface graph for interaction effect of (a) cutting speed and feed rate and (b) cutting speed and depth of cut on cutting force.

*4.3.3.3. Effect of cutting parameters on Ra surface roughness*

Regression model for predicting Ra surface roughness was developed (Eq. 14). Coefficient of determination, $R^2$ of the model was calculated as 77.7%.

$$Ra = 6.98 - 0.0265\,V_c - 88.4\,f - 15.39\,a_p + 0.000076\,{V_c}^2 + 577\,f^2 + 13.69\,{a_p}^2 + 0.099\,V_c \times f + 0.0172\,V_c \times a_p + 53.3\,f \times a_p \quad (18)$$

Normal probability plot (Figure 83a) and histogram of standardized residual (Figure 83b) showed that the residuals were distributed around the zero which confirmed that the developed model was adequate. F-values and P-values of feed rate and depth of cut presented in Table 9 showed that these parameters were statistically significant for Ra surface roughness.

Table 9 Results of ANOVA for Ra surface roughness.

| Source | DF | Adj SS | Adj MS | F-Value | P-Value (α=0.05) |
|---|---|---|---|---|---|
| Model | 9 | 2.53133 | 0.28126 | 3.88 | 0.023 |
| $V_c$ | 1 | 0.08433 | 0.08433 | 1.16 | 0.306 |
| $f$ | 1 | 0.60597 | 0.60597 | 8.37 | 0.016 |
| $a_p$ | 1 | 0.40831 | 0.40831 | 5.64 | 0.039 |
| ${V_c}^2$ | 1 | 0.05700 | 0.05700 | 0.79 | 0.396 |
| $f^2$ | 1 | 1.34007 | 1.34007 | 18.51 | 0.002 |
| ${a_p}^2$ | 1 | 0.47097 | 0.47097 | 6.51 | 0.029 |
| $V_c \times f$ | 1 | 0.01944 | 0.01944 | 0.27 | 0.616 |
| $V_c \times a_p$ | 1 | 0.01471 | 0.01471 | 0.20 | 0.662 |
| $f \times a_p$ | 1 | 0.09103 | 0.09103 | 1.26 | 0.288 |
| Error | 10 | 0.72401 | 0.07240 | | |
| Total | 19 | | | | |

Figure 84a shows the variation of Ra surface roughness with cutting speed and feed rate. At low feed rates Ra values were high, however, by increasing the feed rate, Ra decreased to a minimum value and then increased again with higher feed rates. The effect of depth of cut on Ra surface roughness was increase with increasing depth of cut (Figure 84b). With respect to the cutting speed, by increasing the cutting speed, Ra values decreased (Figure 84a, b).

Minimum amount of Ra roughness was achieved at cutting speed of 90 m/min, feed rate of 0.04 mm/rev and 0.4 mm depth of cut.

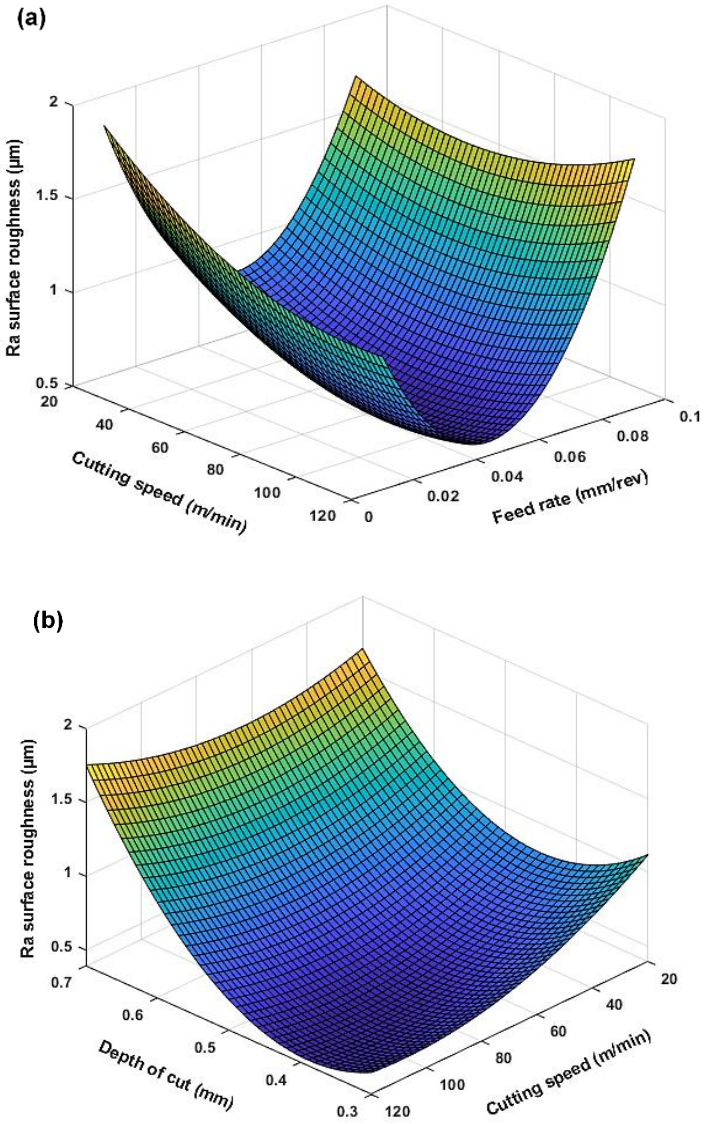


Figure 83 (a) Normal probability plot, (b) histogram of standardized residual for Ra surface roughness.

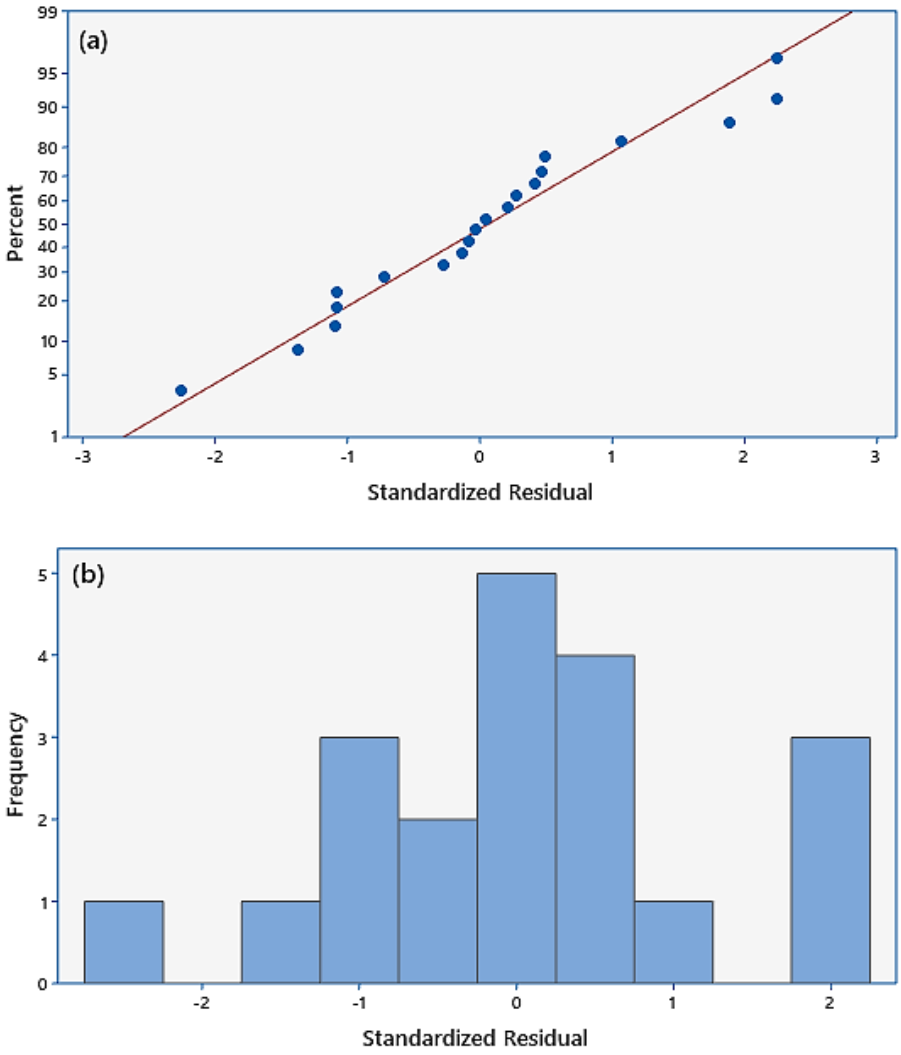


Figure 84 3D surface graph for interaction effect of (a) cutting speed and feed rate and (b) cutting speed and depth of cut on Ra surface roughness.

*4.3.3.4. Multi-response optimization*

Desirability function of RSM was used to perform the multi-response optimization in order to find the optimal cutting parameters that would result in the maximum possible material removal rate, while maintaining the lowest possible flank wear, cutting force and Ra surface roughness values. Each response parameter was converted to a desirability function varying from 0 to 1 in which zero means the response is outside the acceptable region and the value of one indicates

that the response has reached the goal. Individual desirability was combined to provide a measure of composite desirability of the multi response system [3]. Constraints for optimizing flank wear, surface roughness, cutting force and material removal rate are summarized in Table 10. It was determined that cutting speed of 81 m/min, feed rate of 0.06 m/rev and depth of cut of 0.38 mm were the optimum cutting parameters for achieving flank wear of 61 µm, cutting force of 82 N and Ra surface roughness of 0.530 µm with the MRR value of 1.88 $cm^3$/min (Table 11).

The proposed ranges for the cutting parameters which was provided by the manufacturer were cutting speed of 40 m/min (0.08-3), feed rate of 0.04 mm/rev (0.02-0.1) and depth of cut of 0.2 (0.08-3). The optimum feed rate and depth of cut found in this research are in the range of the manufacturer's catalogue, but the cutting speed is twice as high as the one that manufacturer was proposed which means higher production rate can be possible.

Table 10 Constraints for optimization of flank wear, surface roughness, cutting force and material removal rate.

| Response | Goal | Lower | Target | Upper | Weight | Importance |
|---|---|---|---|---|---|---|
| Flank wear, $VB_B$ (µm) | Minimum | - | 23 | 160 | 1 | 1 |
| Cutting force, $F_c$ (N) | Minimum | - | 19 | 184 | 1 | 1 |
| Surface roughness, Ra (µm) | Minimum | - | 0.36 | 1.77 | 1 | 1 |
| $MRR$ ($cm^3$/min) | Maximum | 0.35 | 3.99 | - | 1 | 1 |

Table 11 Multi-response optimization results for response parameters.

| Cutting speed, $V_c$ | Feed rate, $f$ | Depth of cut, $a_p$ | Composite Desirability | Predicted values | | | |
|---|---|---|---|---|---|---|---|
| | | | | Flank wear, $VB_B$ (µm) | Cutting force, $F_c$ (N) | Surface roughness, Ra (µm) | $MRR$ ($cm^3$/min) |
| 81 | 0.06 | 0.38 | 0.63 | 61 | 82 | 0.530 | 1.88 |

## 4.4. SUMMARY AND CONCLUSIONS

In this work, effect of cryogenic turning on Inconel 718 was investigated by experimentally determining the flank wear, cutting force and Ra surface roughness under cryogenic cutting at different cutting parameters, namely cutting speed, feed rate and depth of cut and comparing them with those obtained from flooded and dry conditions. In addition, statistical analyses and multi-response optimization of parameters were carried out in machining under cryogenic condition. The optimum values of cutting parameters were determined using desirability function of response surface methodology (RSM). Following are the main results drawn from this chapter:

(1) Application of liquid nitrogen to the cutting area lowered the flank wear compared to dry cutting, resulting in the values as low as the ones from flooded cutting. Abrasion of flank face of the tool and adhesion of Inconel 718 material were the wear mechanisms in cryogenic and flooded cutting.

(2) Cutting forces were lower under cryogenic cutting performed at low (110 N at 20 m/min) and medium (90 N at 70 m/min) cutting speeds than those in flooded (120 N at 20 m/min, 95 N at 70 m/min) whereas high cutting speed of 120 m/min resulted in higher cutting force compared to flooded cutting (120 N and 100 N).

(3) Ra surface roughness was higher in cryogenic cutting than in flooded cutting for all the cutting parameters used. Formation of surface defects such as built-up layers and cavities formed when cutting under cryogenic condition was dependent on the cutting parameters (cutting speed, feed rate and depth of cut), as opposed to flooded cutting during which there

was a consistency in obtained surface quality in terms of formation of defects on the surface.

(4) Experimental results summarized in 1-3 revealed that there could be an optimum set of values in which cryogenic cutting can provide a performance equivalent to the flooded cutting. Thus, experiments were designed according to the response surface methodology (RSM) under cryogenic condition.

(5) Statistical analysis of Inconel 718 subjected to cryogenic cutting revealed that all the cutting parameters were statistically significant variables and the cutting speed was the most influential parameter on flank wear. The Cutting speed was statistically significant and feed rate was marginally significant parameters on cutting force. Feed rate and depth of cut were the most influential and statistically significant parameters for Ra surface roughness.

(6) Multi-response optimization using desirability function of RSM showed that a cutting speed of 81 m/min, a feed rate of 0.06 mm/rev and a depth of cut of 0.63 mm would constitute an optimum set of cutting parameters for achieving the lowest possible flank wear (61 μm), cutting force (82 N) and Ra surface roughness (0.530 μm) and the highest possible MRR (1.88 $cm^3$/min) in cryogenic cutting under the current test condition.

(7) Given the results from the comparison between cryogenic with flooded cutting in Section 4.3.1, it is predictable that flank wear, cutting force and surface defects be as low as flooded cutting at the optimum parameters, while Ra surface roughness may still result in higher values.

## REFERENCES

[1] A.I. Khuri, S. Mukhopadhyay, Response surface methodology, Wiley Interdisciplinary Reviews: Computational Statistics, 2 (2010) 128-149.

[2] R.D. Koyee, U. Heisel, R. Eisseler, S. Schmauder, Modeling and optimization of turning duplex stainless steels, Journal of Manufacturing Processes, 16 (2014) 451-467.

[3] B. Davoodi, B. Eskandari, Tool wear mechanisms and multi-response optimization of tool life and volume of material removed in turning of N-155 iron–nickel-base superalloy using RSM, Measurement, 68 (2015) 286-294.

[4] M. Günay, M.E. Korkmaz, N. Yaşar, Performance analysis of coated carbide tool in turning of Nimonic 80A superalloy under different cutting environments, Journal of Manufacturing Processes, 56 (2020) 678-687.

[5] P. Zhang, Z. Liu, J. Du, G. Su, J. Zhang, C. Xu, On machinability and surface integrity in subsequent machining of additively-manufactured thick coatings: A review, Journal of Manufacturing Processes, 53 (2020) 123-143.

[6] S.H. Musavi, B. Davoodi, B. Eskandari, Evaluation of surface roughness and optimization of cutting parameters in turning of AA2024 alloy under different cooling-lubrication conditions using RSM method, Journal of Central South University, 27 (2020) 1714-1728.

[7] A. Shokrani, V. Dhokia, S.T. Newman, Investigation of the effects of cryogenic machining on surface integrity in CNC end milling of Ti–6Al–4V titanium alloy, Journal of Manufacturing Processes, 21 (2016) 172-179.

[8] F. Pusavec, A. Deshpande, S. Yang, R. M'Saoubi, J. Kopac, O.W. Dillon, I.S. Jawahir, Sustainable machining of high temperature Nickel alloy – Inconel 718: part 1 – predictive performance models, Journal of Cleaner Production, 81 (2014) 255-269.

[9] A.R.C. Sharman, J.I. Hughes, K. Ridgway, The effect of tool nose radius on surface integrity and residual stresses when turning Inconel 718™, Journal of Materials Processing Technology, 216 (2015) 123-132.

[10] M.C. Shaw, J. Cookson, Metal cutting principles, Oxford university press New York, 2005.

[11] G. Krishnamurthy, S. Bhowmick, W. Altenhof, A.T. Alpas, Increasing efficiency of Ti-alloy machining by cryogenic cooling and using ethanol in MRF, CIRP Journal of Manufacturing Science and Technology, 18 (2017) 159-172.

[12] International Standard ISO 3685, Tool-life testing with single-point turning tools, 1993-11-15.

[13] D.C. Montgomery, Design and analysis of experiments, John wiley & sons, 2017.

[14] V. Tebaldo, G.G. di Confiengo, M.G. Faga, Sustainability in machining: “Eco-friendly” turning of Inconel 718. Surface characterisation and economic analysis, Journal of Cleaner Production, 140 (2017) 1567-1577.

[15] K. Zhuang, X. Zhang, D. Zhu, H. Ding, Employing preheating- and cooling-assisted technologies in machining of Inconel 718 with ceramic cutting tools: towards reducing tool wear and improving surface integrity, The International Journal of Advanced Manufacturing Technology, 80 (2015) 1815-1822.

[16] A. Devillez, G. Le Coz, S. Dominiak, D. Dudzinski, Dry machining of Inconel 718, workpiece surface integrity, Journal of Materials Processing Technology, 211 (2011) 1590-1598.

[17] T. Sata, M. Shaw, Behavior of cellular materials undergoing plastic flow, CIRP Annals, 12 (1964) 190.

[18] T.J. Archdeacon, Correlation and regression analysis: a historian's guide, Univ of Wisconsin Press, 1994.

[19] L. Pritschet, D. Powell, Z. Horne, Marginally significant effects as evidence for hypotheses: changing attitudes over four decades, Psychological Science, 27 (2016) 1036-1042.

# CHAPTER 5

# SUMMARY AND GENERAL CONCLUSIONS

## 5.1. SUMMARY AND CONCLUSIONS

Superalloys are among the important materials in modern applications, as they are extensively used in various industrial areas ranging from aerospace industry to heat treatment and medical equipment. However, they are considered as difficult-to-cut materials and manufacturing high-quality products out of these alloys are expensive. Thus, use of cutting fluid during the cutting process is necessary for obtaining desired results in terms of surface quality and production cost. Consumption of mineral oil cutting fluids, which consist of a significant portion of cutting fluid usage in machining industry, needs to be reduced because of its environmental and health hazards. This study investigated utilization of vegetable oil cutting fluid enhanced by addition of graphene nanoplatelets (GNP) as well as liquid nitrogen ($LN_2$) applied to the cutting area as alternative methods to mineral-based oil.

The results of this thesis showed that addition of GNP and application of liquid nitrogen to the cutting area are effective methods to replace mineral-based cutting fluids. However, in order to

achieve the desired results, these methods should be enhanced and optimized before replacing the mineral-based oils.

Chapter 3 showed that bio-degradable vegetable-based oils can be significantly improved by addition of GNPs at a very small fraction. According to the results from tribological analysis through pin-on-disk tests, this resulted in formation of tribolayer on the tool faces. Formation of tribolayer reduced the COF in the tool-chip interface which resulted in reduction of cutting torque compared to flooded and dry cutting conditions. Considering the fact that most of the cutting energy consumed in the cutting area converts to heat, lower cutting torque resulted in lower cutting temperature. Low cutting torque and temperature contributed to low adhesion of material to the cutting edge of the tool. This helped with retention of the original shape of the cutting edge of the tool, leading to more shearing action, rather than ploughing action, during the cutting process. Consequently, the surface roughness and subsurface microstructural deformation significantly decreased when GNP-blending cutting fluid was used compared to conventional flooded and dry conditions.

It was shown in Chapter 4 that complete omission of cutting fluid during the machining process is feasible by employing cryogenic cutting. Liquid nitrogen evaporates after contacting the tool and workpiece surface leaving no contamination which eliminates the cleaning, recycling, and deposal costs after the machining process. The results from this section showed that Application of liquid nitrogen to the cutting area lowered the flank wear compared to dry cutting, resulting in the values as low as the ones from flooded cutting. At the cutting speed of 70 m/min, cutting force and surface roughness were almost as low as flooded cutting. Thus, experimental results revealed that there could be an optimum set of values in which cryogenic cutting can provide a

performance equivalent to the flooded cutting. Thus, experiments were designed according to the response surface methodology (RSM) under cryogenic condition. Multi-response optimization using desirability function of RSM showed that a cutting speed of 81 m/min, a feed rate of 0.06 mm/rev and a depth of cut of 0.63 mm would constitute an optimum set of cutting parameters

However, there are some shortcomings in implementation of these methods that should be addressed. Some precautions should be taken when using GNP during the cutting process, as nanoparticles are considered as hazardous materials. Also, cleaning the machined part and the machine after the process can be an extra cost. However, the use of graphene nanoplatelets in the cutting fluid (GCF) seems to be necessary as the conventional flooded cutting is not capable of eliminating the subsurface microstructural deformation and produce high surface quality while maintaining high production rate compared to GCF during machining of some critical parts such as shafts and disks that are used in hot section of turbofan engines, namely combustion chamber, the turbine and the exhaust.

With respect to cryogenic cutting, on the other hand, the operator needs special personal protective equipment and needs to take precautions when working with $LN_2$. Also, limitations regarding the tank taking up a large space as well as the need for filling it up frequently create some obstacles in using this method in industrial scale. However, after determining the optimum parameters for each pair of workpieces and cutting tool material the results can be comparable to conventional flooded cutting while implementing clean production.

## 5.2. FUTURE STUDIES

Application of cutting fluid blended with GNP can be applied in other machining processes as well to evaluate its effectiveness. In addition, an optimization method, such as RSM, Taguchi, Gray relational analysis, etc., can be employed to investigate more precisely the optimum values of GNP percentage along with optimum cutting parameters in order to achieve the lowest possible flank wear, cutting force and surface roughness.

In this study, investigation on the effect of use of liquid nitrogen on cutting performance of Inconel 718 was conducted in a short distance of 20 mm for each experiment. For the further and more precise results, cutting process can be carried out in longer cutting distances (or until the tool life criteria is reached) at the predetermined optimum parameters. Effect of cryogenic cutting on machined subsurface deformation and chip morphologies are other important aspects that can be considered in the future works.

# APPENDIX

## SPRINGER NATURE LICENSE
## TERMS AND CONDITIONS

Nov 30, 2020

This Agreement between Mr. Behzad Eskandari ("You") and Springer Nature ("Springer Nature") consists of your license details and the terms and conditions provided by Springer Nature and Copyright Clearance Center.

| | |
|---|---|
| License Number | 4958930431990 |
| License date | Nov 30, 2020 |
| Licensed Content Publisher | Springer Nature |
| Licensed Content Publication | The International Journal of Advanced Manufacturing Technology |
| Licensed Content Title | Flooded drilling of Inconel 718 using graphene incorporating cutting fluid |
| Licensed Content Author | Behzad Eskandari et al |
| Licensed Content Date | Nov 14, 2020 |
| Type of Use | Thesis/Dissertation |
| Requestor type | non-commercial (non-profit) |
| Format | print and electronic |
| Portion | full article/chapter |
| Will you be translating? | no |
| Circulation/distribution | 1 - 29 |
| Author of this Springer Nature content | yes |
| Title | Machining of Inconel 718 nickel-based superalloy using liquid nitrogen and Nano-lubricants |
| Institution name | University of Windsor |
| Expected presentation date | Dec 2020 |
| Requestor Location | Mr. Behzad Eskandari<br>401 Sunset Avenue Windsor, ON N9B 3P4 Canada<br>Attn: University of Windsor, Mechanical, Automotive and Materials Engineering Department |
| Total | 0.00 CAD |
| Terms and Conditions | |

**Springer Nature Customer Service Centre GmbH**
**Terms and Conditions**

This agreement sets out the terms and conditions of the licence (the **Licence**) between you and **Springer Nature Customer Service Centre GmbH** (the **Licensor**). By clicking 'accept' and completing the transaction for the material (**Licensed Material**), you also confirm your acceptance of these terms and conditions.

**1. Grant of License**

**1. 1.** The Licensor grants you a personal, non-exclusive, non-transferable, world-wide licence to reproduce the Licensed Material for the purpose specified in your order only. Licences are granted for the specific use requested in the order and for no other use, subject to the conditions below.

**1. 2.** The Licensor warrants that it has, to the best of its knowledge, the rights to license reuse of the Licensed Material.

However, you should ensure that the material you are requesting is original to the Licensor and does not carry the copyright
of another entity (as credited in the published version).

**1. 3.** If the credit line on any part of the material you have requested indicates that it was reprinted or adapted with permission from another source, then you should also seek permission from that source to reuse the material.

**2. Scope of Licence**

**2. 1.** You may only use the Licensed Content in the manner and to the extent permitted by these Ts&Cs and any applicable laws.

**2. 2.** A separate licence may be required for any additional use of the Licensed Material, e.g. where a licence has been purchased for print only use, separate permission must be obtained for electronic re-use. Similarly, a licence is only valid in the language selected and does not apply for editions in other languages unless additional translation rights have been granted separately in the licence. Any content owned by third parties are expressly excluded from the licence.

**2. 3.** Similarly, rights for additional components such as custom editions and derivatives require additional permission and may be subject to an additional fee. Please apply to Journalpermissions@springernature.com/bookpermissions@springernature.com for these rights.

**2. 4.** Where permission has been granted **free of charge** for material in print, permission may also be granted for any electronic version of that work, provided that the material is incidental to your work as a whole and that the electronic version is essentially equivalent to, or substitutes for, the print version.

**2. 5.** An alternative scope of licence may apply to signatories of the STM Permissions Guidelines, as amended from time to time.

**3. Duration of Licence**

**3. 1.** A licence for is valid from the date of purchase ('Licence Date') at the end of the relevant period in the below table:

| Scope of Licence | Duration of Licence |
|---|---|
| Post on a website | 12 months |
| Presentations | 12 months |
| Books and journals | Lifetime of the edition in the language purchased |

**4. Acknowledgement**

**4. 1.** The Licensor's permission must be acknowledged next to the Licenced Material in print. In electronic form, this acknowledgement must be visible at the same time as the figures/tables/illustrations or abstract and must be hyperlinked to the journal/book's homepage. Our required acknowledgement format is in the Appendix below.

**5. Restrictions on use**

**5. 1.** Use of the Licensed Material may be permitted for incidental promotional use and minor editing privileges e.g. minor adaptations of single figures, changes of format, colour and/or style where the adaptation is credited as set out in Appendix 1 below. Any other changes including but not limited to, cropping, adapting, omitting material that affect the meaning, intention or moral rights of the author are strictly prohibited.

**5. 2.** You must not use any Licensed Material as part of any design or trademark.

**5. 3.** Licensed Material may be used in Open Access Publications (OAP) before publication by Springer Nature, but any Licensed Material must be removed from OAP sites prior to final publication.

**6. Ownership of Rights**

**6. 1.** Licensed Material remains the property of either Licensor or the relevant third party and any rights not explicitly granted herein are expressly reserved.

**7. Warranty**

IN NO EVENT SHALL LICENSOR BE LIABLE TO YOU OR ANY OTHER PARTY OR ANY OTHER PERSON OR FOR ANY
SPECIAL, CONSEQUENTIAL, INCIDENTAL OR INDIRECT DAMAGES, HOWEVER CAUSED, ARISING OUT OF OR IN
CONNECTION WITH THE DOWNLOADING, VIEWING OR USE OF THE MATERIALS REGARDLESS OF THE FORM OF ACTION,
WHETHER FOR BREACH OF CONTRACT, BREACH OF WARRANTY, TORT, NEGLIGENCE, INFRINGEMENT OR OTHERWISE
(INCLUDING, WITHOUT LIMITATION, DAMAGES BASED ON LOSS OF PROFITS, DATA, FILES, USE, BUSINESS
OPPORTUNITY OR CLAIMS OF THIRD PARTIES), AND
WHETHER OR NOT THE PARTY HAS BEEN ADVISED OF THE POSSIBILITY OF SUCH DAMAGES. THIS LIMITATION SHALL APPLY NOTWITHSTANDING ANY FAILURE OF ESSENTIAL PURPOSE OF ANY LIMITED REMEDY PROVIDED HEREIN.

**8. Limitations**

**8. 1.** ***BOOKS ONLY:***Where **'reuse in a dissertation/thesis'** has been selected the following terms apply: Print rights of the final author's accepted manuscript (for clarity, NOT the

published version) for up to 100 copies, electronic rights for use only on a personal website or institutional repository as defined by the Sherpa guideline (www.sherpa.ac.uk/romeo/).

**9. Termination and Cancellation**

**9. 1.** Licences will expire after the period shown in Clause 3 (above).

**9. 2.** Licensee reserves the right to terminate the Licence in the event that payment is not received in full or if there has been a breach of this agreement by you.

**Appendix 1 — Acknowledgements:**

**For Journal Content:**

Reprinted by permission from [**the Licensor**]: [**Journal Publisher** (e.g. Nature/Springer/Palgrave)] [**JOURNAL NAME**] [**REFERENCE CITATION** (Article name, Author(s) Name), [**COPYRIGHT**] (year of publication)

For **Advance Online Publication papers:**

Reprinted by permission from [**the Licensor**]: [**Journal Publisher** (e.g. Nature/Springer/Palgrave)] [**JOURNAL NAME**] [**REFERENCE CITATION** (Article name, Author(s) Name), [**COPYRIGHT**] (year of publication), advance online publication, day month year (doi: 10.1038/sj.[JOURNAL ACRONYM].)

**For Adaptations/Translations:**

Adapted/Translated by permission from [**the Licensor**]: [**Journal Publisher** (e.g. Nature/Springer/Palgrave)] [**JOURNAL**

**NAME**] [**REFERENCE CITATION** (Article name, Author(s) Name), [**COPYRIGHT**] (year of publication)

**Note: For any republication from the British Journal of Cancer, the following credit line style applies:**

Reprinted/adapted/translated by permission from [**the Licensor**]: on behalf of Cancer Research UK: : [**Journal Publisher**

(e.g. Nature/Springer/Palgrave)] [**JOURNAL NAME**] [**REFERENCE CITATION** (Article name, Author(s) Name), [**COPYRIGHT]** (year of publication)

For **Advance Online Publication** papers:

Reprinted by permission from The [**the Licensor**]: on behalf of Cancer Research UK: [**Journal Publisher** (e.g.

Nature/Springer/Palgrave)] [**JOURNAL NAME**] [**REFERENCE CITATION** (Article name, Author(s) Name), [**COPYRIGHT**] (year of publication), advance online publication, day month year (doi: 10.1038/sj.[JOURNAL ACRONYM])

**For Book content:**

Reprinted/adapted by permission from [**the Licensor**]: [**Book Publisher** (e.g. Palgrave Macmillan, Springer etc) [**Book Title**] by [**Book author**(s)] [**COPYRIGHT**] (year of publication)

**Other Conditions**:

Version 1.2

**Questions? customercare@copyright.com or +1-855-239-3415 (toll free in the US) or +1-978-646-2777.**

# VITA AUCTORIS

| | |
|---|---|
| NAME: | Behzad Eskandari |
| PLACE OF BIRTH: | Zanjan, Iran |
| EDUCATION: | University of Windsor, MASc, Windsor, ON, 2020. |
| | University of Tabriz, MSc, Tabriz, Iran, 2013. |
| | Montazeri Technical College of Mashhad, BSc, Mashhad, Iran, 2010 |
| | University of Zanjan, AD, Zanjan, Iran, 2007. |